

Development and Optimization of Methods for Accelerated Magnetic Resonance Imaging

THÈSE N° 8237 (2018)

PRÉSENTÉE LE 23 MARS 2018

À LA FACULTÉ DES SCIENCES ET TECHNIQUES DE L'INGÉNIEUR
LABORATOIRE DE TRAITEMENT DES SIGNAUX 5
PROGRAMME DOCTORAL EN GÉNIE ÉLECTRIQUE

ÉCOLE POLYTECHNIQUE FÉDÉRALE DE LAUSANNE

POUR L'OBTENTION DU GRADE DE DOCTEUR ÈS SCIENCES

PAR

Tom HILBERT

acceptée sur proposition du jury:

Prof. D. Van De Ville, président du jury
Prof. J.-Ph. Thiran, Dr G. Krüger, directeurs de thèse
Prof. K. T. Block, rapporteur
Prof. D. G. Norris, rapporteur
Dr O. Reynaud, rapporteur



ÉCOLE POLYTECHNIQUE
FÉDÉRALE DE LAUSANNE

Suisse
2018

It is the tension between creativity and skepticism that has produced
the stunning and unexpected findings of science.
— Carl Sagan

Meiner Familie...

Acknowledgements

I joined the ACIT group for the first time in 2009. Since then, I have had countless projects, internships and theses to finish. Today, eight years later, I'm finishing my third and (hopefully) last thesis, my dissertation. I would like to thank my colleagues and friends who always helped me and made this period a great part of my life. However, there are a few people I would like to thank personally.

Back in 2009, I was certainly far below the average age in the ACIT group. Despite of being just at the beginning of my academic career (4th semester in my bachelor studies), you, Gunnar, believed in my skills and kept finding funding and hiring me for various projects from which I learned so much. I want to thank you for your support and trust that shaped my career and led me all the way to the end of my PhD, and hopefully, more to come.

In my very first project I was supervised by probably the coolest PhD student in the lab. It makes me laugh when I think back to my worries of what I should wear on my first day, only to see Tobi coming around the corner in shorts and a funny t-shirt. Eight years later, Tobi is the head of the ACIT group and is not only supervising me, but also 12 other knowledge seeking researchers. I want to thank you, Tobi, for always being both a good supervisor and a friend. I learned countless things (e.g. how to properly name a word document or operate a several million dollar MRI scanner) from you over these many years and I'm looking forward to continuing this great endeavour.

I would like to thank you, Jean-Philippe, for providing me the opportunity to work in the great environment of the LTS5. The diverse projects and expertise of you and your lab are extraordinary, and I want to thank you for welcoming me to the LTS5 family so kindly.

Despite being very nervous at the beginning, I will remember my thesis exam as a rather pleasant experience. I want to thank my jury, Prof. David J. Norris, Prof. Kai T. Block, and Dr. Oliver Reynaud, and the committee president Prof. Dimitri Van De Ville for the interesting discussions and for their precious time.

One reason why I actually manage to get out of bed every morning and take the crowded metro to the office is the ACIT team. I could always rely on the support of the team and this gave me the motivation to keep on going. Béné, thank you for all the years of teamwork, and one day I hope I'll be at least a little bit as organized as you. Thank you, Ricardo, for not only critically proofreading this thesis, but also for your discussions about work, your crazy projects and politics during pasta with Pesto Rosso and beer at home. Thank you, Davide, for sharing your deep knowledge in programming that always comes along with either a kind insult or wisdom from the book of Mormons. Thank you, Mario, Maryna, Pavel, John, and Bobo, for

Acknowledgements

the great time in our little PhD office, where we prayed to the gods of Bollywood and always had something to laugh about. Thank you, Kieran, Jonas and Alexis, for helping me when I got stuck with problems that seemed unsolvable, and for always asking the difficult questions during presentations. I also had the pleasure to supervise two very smart Master students, Emilie and Gian-Franco. Thank you for being patient with my first attempts at supervision. My gratitude goes also to the many interns and students that created so many memorable moments. Luca, yes I'll try deep learning. Alexandra, my stomach still hurts from all the Haribo. Theo, I miss the epic Fridays. Pascal, I still cannot speak nor understand Swiss-German.

I had the honor to work together with great minds in the field of MRI, without whom this thesis would have much fewer innovative ideas. Thank you, Tilman, for being so generous to provide your code and knowledge upon which I built my PhD work. I want to send a big thanks to the bSSFP gurus in Basel. It was always fun to work with you, Oliver and Damien, and it is impressive that the flow of ideas never stopped. My gratitude goes also to the simultaneous-multi-slice experts, David, Jenni, Laurent, and Jose in Nijmegen and their patients in answering my countless questions about PINS pulses. I also was given the opportunity to visit the CAI2R at the New York University for a month. Thank you, Martijn and Tobias B., for making this possible and also Thomas B., Thomas V., Florian for welcoming me so kindly.

In the research of new clinical tools in radiology, one obviously has to consider the feedback of the expert radiologists. I want to send my gratitude to Prof. Meuli, Prof. Maeder, Dr. Hagman and Dr. Omoumi for always providing constructive critique on our new ideas, no matter how unreasonable they may seem, and providing the input that was necessary to steer my research into the right direction.

I was also part of a team of researchers and developers in Erlangen. Thank you, Heiko, for letting me being a part of this team despite the long distance. Thank you, Michael, Christoph, Elisabeth, Alto, Esther and Rainer, for all the support and ideas.

Probably the most social, but also least productive, period of my PhD was spent in the open space of the LTS5. I want to thank you, Didrik, Vijay, Maryna, Gabriel, and all the other people who shared an amazing time, crazy nights in the bar Giraffe and a fair amount of Cuvée des Trolls with me.

Needless to say that everything that I present in this thesis did not work right away. It required dozens of nights in the basement of the CHUV at the scanner. One motivation to keep commuting between EPFL and CHUV was the group of Mathias. Although you guys think that Neuro MRI is boring, you, Jessica, Ruud, Simo, Gabri, Andrew, Giulia, Emeline and Roberto made me feel welcome and we have become good friends over the years. Thank you.

Tesekkürler, Esi, for your frequent phone calls that allowed us to stay connected, although we both continued on different paths after the master studies. I am pretty sure that some paper drafts would still not be finished without your virtual "Arschtritt".

Thank you, Chris and Caroline, for baring with my three hour dumpling stuffing and two hour sushi rolling workshops that ended with a feast. I cannot even imagine a boring evening or skiing day when you guys are around. Also thank you, Chris, for kicking my "inner-swine-dog". I appreciate it, even though it may not seem like it.

Murat and Marili, it seems like I have known you for ages now and I want to send my warm

thanks for all the quality time we spent together travelling, hiking, cooking, skiing, dancing, sailing and all the great activities that balance out the work stress.

Another factor that I need in order to unwind is music. The weekly noise-making with “The Available” in the bunker of EPFL has helped to forget the bugs and disappointing results. Thank you, Chica, João (Hendrix), João (the wise), Joaquin and Dan, for not getting mad when I hit the drums even louder after a rough day.

Usually, I did not seem stressed when I was working on this thesis. However, there is one person that knows the truth. Nora, thank you for dealing with the-nervewracking-me that surfaces the moment I come home. I Kant thank you enough for your kindness, heartwarming care and inspiration.

Liebe Omas, ich bin euch so sehr dankbar für eure Unterstützung und dass Ihr es mir nicht übel nimmt dass ich mich entschied so weit weg von Zuhause zu leben. Ich bin froh dass Ihr mich in Lausanne besucht habt und dass Ihr jetzt auch versteht warum ich diesen Ort so sehr mag.

Marci, Du warst schon immer ein Vorbild und vielleicht hätte ich nie studiert wenn ich nicht damals mit dir in Dresden probe-studiert hätte. So viele Jahre später, werden wir beide zu „Dr. Hilbert“ und das sogar im selben Monat. Vielen Dank!

Vati und Mutti. Mit eurer Liebe und Unterstützung habt Ihr mich erst im kleinen Crossen gedeihen lassen und raus in die weite Welt geschickt. Danke dass Ihr immer, in guten sowie auch schlechten Zeiten, für mich da wart und mich immer frei entscheiden lassen habt was ich mit meinen Leben mache. Danke für alles.

Lausanne, 2 November 2017

T. H.

Abstract

Magnetic resonance imaging (MRI) has yielded great success as a medical imaging modality in the past decades, and its excellent soft tissue contrast is used in clinical routine to support diagnosis today. However, MRI is still facing challenges. For example, the acquisition time is long in comparison to computed tomography, especially when directly measuring tissue properties with quantitative MRI. This thesis presents new approaches to accelerate quantitative MRI acquisitions without decreasing the accuracy, using analytical and numerical signal models.

A quantitative acquisition to map the transverse relaxation T2 was first accelerated by combining parallel imaging with model-based reconstruction. It was demonstrated that the combination leads to an improved artifact behaviour in comparison to a model-based reconstruction alone, facilitating higher acceleration factors. The technique was optimized to obtain T2 maps from the brain, knee, prostate and liver, with good initial results. The idea of combining methods was continued by introducing simultaneous multi slice acquisition to the T2 mapping approach. Furthermore, a numerical simulation rather than an analytical solution was used in the model-based reconstruction, resulting in a fast undersampled acquisition that also accounts for transmit field inhomogeneity. This approach yielded more accurate and faster acquired T2 values.

Magnetic resonance fingerprinting (MRF) is a recently introduced model-based reconstruction that promises to provide multiple quantitative maps using a fast pseudo-random acquisition. However, similar to other model-based approaches, MRF depends on how well the model describes the measured signal. It was demonstrated in this work that the estimated quantitative maps may be systematically biased if the model does not account for magnetization transfer effects. To this end, a simplified numerical model was proposed, that includes magnetization transfer, and yields more accurate quantitative values.

The same approach was translated to bSSFP acquisitions, where banding artifacts are a major limitation: the analytical model of a phase-cycle bSSFP acquisition was used to separate signal effects of the human tissue from signal effects due to magnetic field inhomogeneity. The separation allowed the removal of typical signal voids in bSSFP images. A compressed sensing reconstruction was employed to avoid additional acquisition time.

In summary, this thesis has introduced new approaches to employ signal models in different applications, with the aim of either accelerating an acquisition, or improving the accuracy of an existing fast method. These approaches may help to make the next step away from qualitative towards a fully quantitative MR imaging modality, facilitating precision medicine

Acknowledgements

and personalized treatment.

Keywords

magnetic resonance imaging; quantitative imaging; acquisition acceleration; model-based reconstruction

Zusammenfassung

Magnet Resonanz Tomographie (MRT) hat in den letzten Jahrzehnten einen großen Erfolg erzielt und mit einem exzellentem Weichgewebekонтраст wird es heute im klinischen Alltag genutzt um Diagnosen zu unterstützen. Jedoch stellt sich der MRT immer noch Herausforderungen. Zum Beispiel ist die Aufnahmezeit lang im Vergleich zu der Computer Tomographie, besonders wenn Gewebeeigenschaften direkt mit quantitativer Bildgebung gemessen werden. In diesen Zusammenhang studiert diese Dissertation neue Ansätze, unter der Verwendung von Signalmodellen, um quantitative MRT Bildgebung zu beschleunigen ohne die Genauigkeit zu verringern.

Eine quantitative Messung der transversalen Relaxation T_2 wurde zunächst beschleunigt indem parallel Bildgebung mit modellbasierter Rekonstruktion kombiniert wurde. Es wurde gezeigt dass die Kombination zu einem besseren Bildfehlerverhalten führt im Vergleich zu einer alleinigen modellbasierten Rekonstruktion. Die neue Methodik wurde optimiert für die Messung von T_2 Karten im Kopf, im Knie, der Prostata und der Leber und zeigte gute initiale Ergebnisse.

Die Idee Methoden zu kombinieren wurde fortgesetzt indem Simultane-Multiple-Schichten Aufnahme in der T_2 Kartographie eingeführt wurde. Weiterhin wurde eine numerische Simulation anstatt einer analytischen Lösung in der modellbasierten Rekonstruktion verwendet, was zu einer schnellen unterabgetasteten Messung führte welche auch Inhomogenität im Radiofrequenzfeld beachtet. Somit konnten akkurater und schneller gemessene T_2 Werte erreicht werden.

Magnetresonanz-Fingerprinting (MRF) ist eine modellbasierte Rekonstruktion die vor kurzem vorgestellt wurde und verspricht mehrere quantitative Karten mit einer schnellen pseudozufälligen Aufnahme bereit zu stellen. Jedoch ist MRF, wie andere modellbasierte Ansätze, abhängig von wie genau das Model das gemessene Signal beschreibt. In dieser Arbeit wurde gezeigt, dass die geschätzten quantitativen Karten einen systematischen Fehler haben können wenn Magnetisierungstransfer nicht beachtet wird. Daher wurde ein vereinfachtes numerisches Model vorgeschlagen das Magnetisierungstransfer einbezieht und somit akkurater quantitative Werte erzielte.

Derselbe Ansatz wurde auf bSSFP Messungen übertragen bei denen Bildfehler ein große Limitierung sind: das analytische Model einer Phasenzyklen bSSFP Messung wurde genutzt um Signaleffekte vom Menschlichen Gewebe von Signaleffekten durch Magnetfeldinhomogenität zu trennen. Die Trennung ermöglicht die Entfernung des typischen Signalabfalls in bSSFP Bildern. Eine compressed sensing Rekonstruktion wurde verwendet um zusätzliche

Acknowledgements

Aufnahmezeit zu verhindern.

Zusammenfassend, diese Dissertation hat neue Ansätze zur Verwendung von Signalmodellen in verschiedenen Anwendungen vorgestellt, mit dem Ziel eine Aufnahme zu beschleunigen oder die Genauigkeit einer bereits existierenden Methodik zu verbessern. Diese Ansätze mögen dabei helfen den nächsten Schritt, weg von qualitativ in Richtung einer quantitativen Magnetresonanztomographie zu machen, um präzise Medizin und personalisierte Behandlung zu ermöglichen.

Schlüsselwörter

Magnet Resonanz Tomographie; Quantitative Bildgebung; beschleunigte Messung; Modellbasierte Rekonstruktion

Contents

Acknowledgements	v
Abstract (English/Deutsch)	ix
List of figures	xv
List of tables	xviii
Introduction	1
1 Introduction	1
1.1 Aim and structure of the thesis	3
2 Background	5
2.1 Nuclear Magnetic Resonance	5
2.2 Spatial Encoding	9
2.2.1 Slice Selective Excitation - 2D Imaging	11
2.2.2 In-Plane Localization	12
2.2.3 Non Selective Excitation – 3D Imaging	14
2.3 MR Pulse Sequence Designs	15
2.3.1 Spin-Echo sequence	15
2.3.2 Gradient Recalled Echo Sequence	17
2.3.3 Magnetization Preparation	18
2.4 Instrumentation	19
2.5 Quantitative Magnetic Resonance Imaging	21
2.5.1 T_2 Mapping	22
2.5.2 T_1 Mapping	23
2.5.3 Multi Parametric Mapping	24
2.5.4 Synthetic Contrasts	25
2.6 Accelerated MRI	25
2.6.1 K-Space and Sequence Sampling Techniques	26
2.6.2 Parallel Imaging	26
2.6.3 Compressed Sensing	28
2.6.4 Model-Based Reconstruction	29
2.6.5 Simultaneous Multi Slice	30

3	Accelerated T_2 Mapping Combining Parallel MRI and Model-Based Reconstruction	33
3.1	Introduction	33
3.2	Materials and Methods	35
3.2.1	Acquisition	35
3.2.2	Reconstruction	36
3.2.3	Artificial Undersampling for Ground-Truth Comparison	36
3.2.4	Acquisition of Undersampled Data and Reproducibility	38
3.3	Results	38
3.3.1	Artificial Undersampling for Ground-Truth Comparison	38
3.3.2	Acquisition of Undersampled Data and Reproducibility	40
3.4	Discussion	41
4	Fast Model-Based T_2 Mapping using SAR-Reduced Simultaneous-Multi-Slice Excitation	45
4.1	Introduction	46
4.2	Materials and Methods	46
4.2.1	Acquisition	46
4.2.2	Reconstruction	48
4.2.3	In Vivo Studies	52
4.2.4	Phantom Studies	52
4.3	Results	53
4.3.1	In Vivo Studies	53
4.3.2	Phantom Studies	54
4.3.3	SAR Aspects	54
4.3.4	Computational Requirements	55
4.4	Discussion	55
5	Mitigating the Effect of Magnetization Transfer in Magnetic Resonance Fingerprinting	61
5.1	Introduction	61
5.2	Theory	62
5.2.1	Common Model of Magnetization Transfer	63
5.2.2	Simplified Model	63
5.3	Methods	66
5.3.1	In-Vivo Experiments	66
5.3.2	In Silico Experiments	68
5.3.3	In Vitro Experiments	68
5.4	Results	68
5.4.1	In Vivo Experiments	68
5.4.2	In Silico Experiments	70
5.4.3	In Vitro Experiments	71
5.5	Discussion	72

6 True constructive interference in the steady state	77
6.1 Introduction	77
6.2 Methods	80
6.2.1 Acquisition	80
6.2.2 Reconstruction	81
6.2.3 Simulations and Imaging	82
6.3 Results	84
6.4 Discussion	87
7 Conclusion	93
7.1 Achieved Results	93
7.2 Clinical Impact of this Work	94
7.3 Outlook	96
Bibliography	105
Publications	107
Curriculum Vitae	111

List of Figures

1.1	The first MRI apparatus	2
1.2	Modern MRI	3
2.1	Protons outside and inside a magnetic field	6
2.2	Excitation of spins	7
2.3	Relaxation of spins	8
2.4	Relaxation Curves	9
2.5	Example sequence diagram	10
2.6	Slice selection	11
2.7	K-space frequencies	12
2.8	Frequency encoding	13
2.9	Phase encoding	14
2.10	Spin Echo (SE) sequence design	16
2.11	Gradient Recalled Echo (GRE) sequence design	17
2.12	Balanced Steady State Free Precession (bSSFP) sequence design	18
2.13	Inversion recovery magnetization preparation	19
2.14	Instrumentation of a MRI scanner	21
2.15	Number of publications in quantitative MRI	21
2.16	T_1 mapping with the MP2RAGE	23
2.17	Multi-parametric mapping with TESS	24
2.18	Reconstructing partially parallel acquired data with GRAPPA	27
2.19	Sparse representation in the wavelet-domain	28
2.20	Model-based reconstruction	29
2.21	Simultaneous-Multi-Slice reconstruction.	30
3.1	Sampling pattern of MARTINI and GRAPPATINI	35
3.2	Results of artificial undersampling	39
3.3	Results of undersampled acquisitions.	40
3.4	T_2 maps and simulated contrasts in different organs	42
4.1	Simulations-Multi-Slice CPMG sequence	47
4.2	Employed sampling pattern for acceleration.	47
4.3	Reconstructing Simulations-Multi-Slice and undersampled CPMG data	49
4.4	Stimulated echo effects in CPMG acquisitions.	50

List of Figures

4.5	In Vivo results for undersampled SMS T_2 mapping.	53
4.6	Reproducibility of T_2 values.	56
4.7	Results of phantom experiment	57
4.8	Simulated Contrasts with SMS-CPMG acquisitions.	58
5.1	Magnetization transfer models	66
5.2	Magnetization transfer fingerprinting sequence	67
5.3	Magnetization transfer effects with and without two-pool model	69
5.4	MT-MRF in vivo results from all subjects	70
5.5	Quantitative values in regions of interest.	71
5.6	Example fingerprints	72
5.7	Simulation of model violations	73
5.8	Phantom results of MT-MRF	74
6.1	Performance of various combination methods.	79
6.2	Acquisition scheme for trueCISS	80
6.3	Simulations of regularization of trueCISS	83
6.4	Fitting Robustness of trueCISS	85
6.5	Sparse representation with trueCISS	86
6.6	TrueCISS versus CISS in phantom	88
6.7	TrueCISS parametric maps.	89
6.8	TrueCISS versus CISS in vivo	90

List of Tables

2.1	Relaxation times	8
2.2	Image parameters and contrast	16
3.1	Acquisition parameters	37
4.1	T_2 values within regions of interest.	54

1 Introduction

Technical advances in radio communication during World War II allowed the discovery of 'Nuclear induction' shortly after the end of the war in 1945. Bloch and Rabi [1] as well as Purcell and Pound [2] independently found that voltage can be registered within a coil close to a sample within a magnetic field, after it was irradiated with a radio-frequency (RF) pulse – thereby discovering the nuclear magnetic resonance (NMR) signal. Shortly after, in 1949, Hahn accidentally discovered the spin echo; an additional NMR signal that can be measured when applying a second RF pulse after a short time delay [3]. The spin echo allowed the measurement of relaxation effects [4], which, in 1971, Damadian used to differentiate between healthy and cancerous tissues in mice [5]. These results provided a simple metric, which was, the first proof of concept for the diagnostic use of magnetic resonance.

In 1974, Damadian developed a machine that allowed the spatial encoding of the NMR signal, which is believed to have produced the first image of the human body, launching the era of magnetic resonance imaging (MRI). Figure 1.1 shows a schematic drawing of the apparatus from the US Patent [6] and an example of an image acquired with this machine [7]. The apparatus had only a small field of view (FOV) where the magnetic field was homogeneous, and from which the NMR signal could be retrieved. Therefore, the table where the subject laid had to be moved within this FOV in order to spatially encode the image, resulting in a long acquisition time and a low resolution. The following years saw dramatic improvements in the entire field, leading up to MRI as we know it today. In 1973, Lauterbur proposed the use of magnetic field gradients to spatially encode the NMR signal along one dimension, using similar image reconstruction methods as in computed tomography (CT) [8]. This method drastically reduced acquisition time, while improvements in resolution came about in 1974 with an invention of Sir Mansfield [9]; he used selective excitation to sensitize the acquisition to a single image slice. To encode the third and last spatial dimension in the NMR signal, Kumar et al. proposed the two-dimensional Fourier imaging approach in 1975 [10], a method which is still used today. Since the 1970's, image contrast, quality and resolution have all been improved by development of better hardware and acquisition techniques. Commercialization and the serial production of magnets in the last decades have facilitated the worldwide distribution of

Chapter 1. Introduction

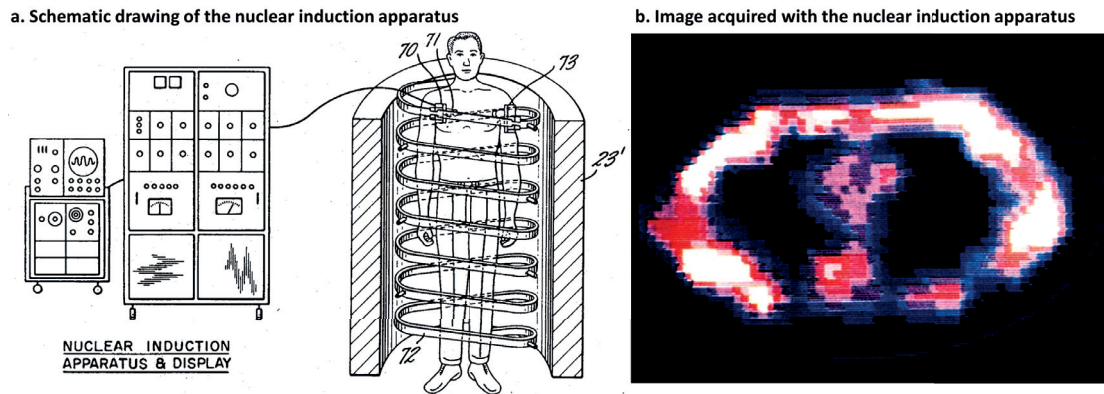


Figure 1.1: (a) A schematic drawing from the US patent describing Damadian's apparatus that resembles the first MRI. (b) An example image acquired with this apparatus, showing a transversal slice of human lungs.

MRI to hospitals, where it is now used in clinical routine, being a crucial part of the diagnostic process. These achievements were also recognized by the Nobel Committee in 1952, 1991, 2002 and 2003, awarding researchers in this field for their contributions.

One of the main advantages of MRI over other imaging methods in clinical use is its excellent soft tissue contrast. For example, in CT images, the intensity difference between white matter and grey matter is far less pronounced than in MRI. This renders MRI especially valuable for neuronal and muscular-skeletal applications. Furthermore, MRI is not relying on ionizing radiation, unlike CT imaging. Figure 1.2 shows a modern MRI scanner from 2017, and a brain image acquired with this machine, comparable to the apparatus design and acquisition from 1977 (Figur 1.1).

Despite the dramatic improvement of MRI techniques, the acquisition of a series of images with different contrasts requires on average 15 minutes, depending on the investigated body region. That is significantly slower than a usual CT exam, and leads to increased patient discomfort, complex scheduling, and a decreased cost-benefit ratio, in conjunction with high maintenance costs. Furthermore, the acquired images are often not standardized, since different institutions use customized image acquisition protocols and different scanner hardware.

Efforts have been made in the past to standardize imaging protocols by matching contrasts across institutions, vendors and field strengths, facilitating better reproducibility. One such example is the Alzheimer's disease Neuroimaging Initiative (ADNI) which has collected over 1700 datasets to date, and published open access imaging protocols tailored for scanning Alzheimer's patients [11]. Nevertheless, conventional MRI images are a qualitative measure, meaning that the contrast is mostly affected by tissue proper-ties, but still depends on many other hardware-related and physiological effects, preventing direct comparison across patients. The difficulties to run studies with non-standardized images ask for new techniques to avoid influences from experimental conditions. By contrast, quantitative MRI (qMRI) aims to directly

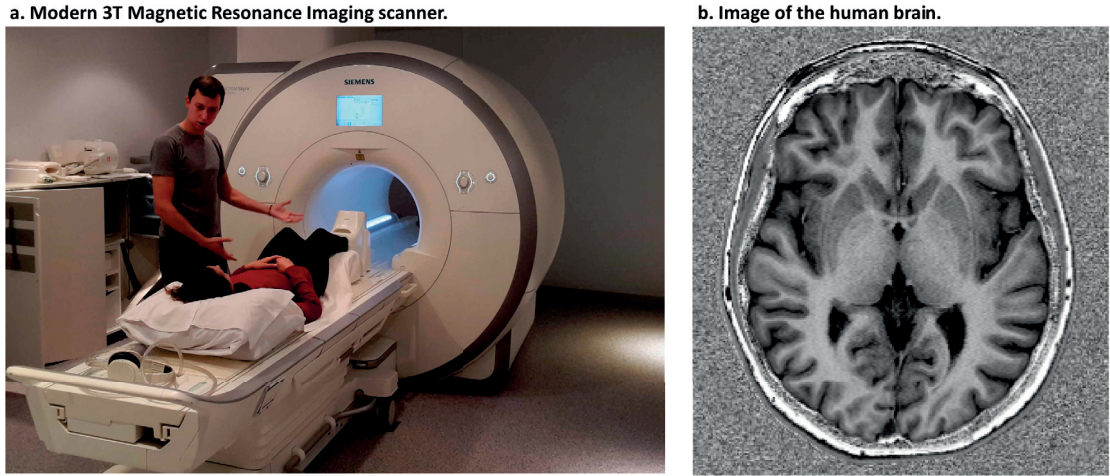


Figure 1.2: (a) Picture of a modern magnetic resonance imaging scanner (MAGNETOM Skyra, Siemens, Germany), and (b) an image of the brain that is possible with such a scanner.

measure tissue properties, ideally independent from the experimental conditions. In qMRI, tissue properties are expressed as quantitative values with physical units, analogous to the measurement of systolic and diastolic blood pressure, expressed in mmHg. This technique spatially maps the measured tissue properties resulting in an image called a quantitative map. This facilitates comparisons either within one patient at multiple time points in order to extract a trend of tissue alternation (intra-subject), or between a tissue property of a patient and a normative range derived from a healthy cohort in order to detect abnormal values (inter-subject). Although quantitative measures have proven to be a good biomarker for disease in the very early days of NMR [5], it has not been established in clinical routine yet, partly because qMRI often requires even longer acquisition times than conventional weighted MRI. An entire field of MRI research has been devoted to overcoming these limitations, with the final goal to move MRI from a qualitative to a standardized quantitative examination, facilitating precision medicine and personalized treatment in the future. One key step towards reaching this goal is to reduce the acquisition time, while retaining or improving the accuracy and precision of the estimated quantitative value.

1.1 Aim and structure of the thesis

This work focuses on optimizing and developing image acquisition and reconstruction methods to obtain quantitative image information faster than conventional imaging techniques. The aim is to reduce the scan time enough to facilitate a routine use of these imaging techniques in a clinical setting, without compromising image quality.

In **Chapter 2**, the state of the art in MRI is described, starting from basic physics to quantitative imaging and acquisition acceleration techniques.

Chapter 3 introduces a method that aims at combining two acceleration techniques, parallel imaging and model-based reconstruction, to acquire a whole-brain, quantitative map of the transverse relaxation in less than 2 minutes. In doing so, the advantages of both methods are combined, resulting in a better artifact behaviour and higher acceleration factors.

Based on Chapter 3, **Chapter 4** continues the idea of combining different acceleration techniques for fast quantitative mapping of the transverse relaxation. A method is introduced where simultaneous-multi-slice pulses enable the acquisition of different sections of the brain at the same time, accelerating the acquisition. A new reconstruction is presented that separates the signals from the different slices, and uses a model-based reconstruction to obtain the quantitative values.

Since model-based reconstruction relies on the accuracy of the physical model to reconstruct data, **Chapter 5** focuses on how an over-simplified model may bias the quantification of relaxation. Using the example of magnetic resonance fingerprinting (MRF), it is demonstrated that physical models are often an approximation of the underlying micro-structure in human tissue, and that magnetization transfer can cause a bias in the relaxation estimation. Further, a new model is introduced that accounts for magnetization transfer and mitigates this bias.

In **Chapter 6**, multiple quantitative maps are estimated on a single balanced Steady State Free Precession (bSSFP) acquisition. Some of these maps represent tissue properties, others represent scanner imperfections. If accurately estimated, scanner imperfections can be separated and removed from the image contrast, resulting in a more standardized acquisition. This improvement is realized via compressed sensing reconstruction, without requiring additional scan time.

Finally, in **Chapter 7**, the thesis is concluded and a future outlook for the introduced methods is discussed.

2 Background

In this Chapter, the basics of MRI are introduced, starting with the physical principals of nuclear magnetic resonance, how an image is generated using these principles and the required instrumentation. Afterwards, a short introduction into quantitative MRI will be given and methods for quantifying relaxation described. Finally, the Chapter ends with a summary of acceleration methods which are already used in fast MRI today. More detailed descriptions and analytical solutions can be found in Haacke et al. [13].

2.1 Nuclear Magnetic Resonance

Protons, in particular hydrogen nuclei, have a naturally occurring spin that gives them a magnetic moment. Thus, protons can be seen as small magnets whose magnetization is described by a vector M . Since protons are usually randomly distributed and oriented, the sum of their magnetization vectors, the net magnetization, is null (see also Figure 2.1a). However, when a strong external magnetic field (B_0) is applied, the magnetization vectors of the protons either align in the direction (parallel) or against the direction (anti-parallel) of this external magnetic field. Depending on the field strength, there are more parallel spins (low energy state) than anti-parallel spins (high energy state), therefore a net magnetization exist along the direction of the magnetic field (see also Figure 2.1b).

Furthermore, the spinning protons precess about the axis of the B_0 field, whereas precession corresponds to the gyration of the spinning axis of the proton about the axis in direction of the magnetic field, similar to a dreidel wobbling around the axis of the earth's gravitational field. The precessional frequency ω_0 , also referred to as the Larmor frequency or resonance frequency, is proportional to the field strength of the main magnetic field B_0 by the gyromagnetic ratio γ :

$$\omega_0 = \gamma B_0 \tag{2.1}$$

The aforementioned magnetization vector M of a proton can be described in a coordinate

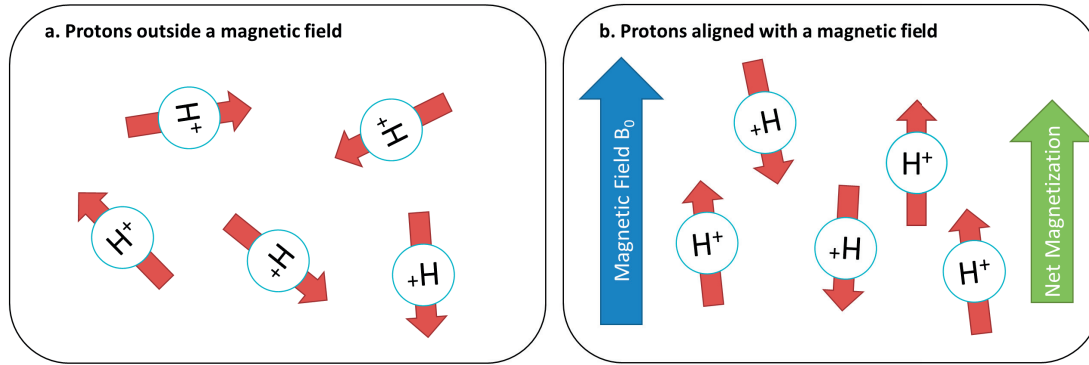


Figure 2.1: (a) Protons which are outside a strong magnetic field are randomly distributed and oriented, therefore the sum of their magnetization (net magnetization) is zero. (b) Protons within a strong magnetic field align with the field parallel or anti-parallel, generating a small net magnetization.

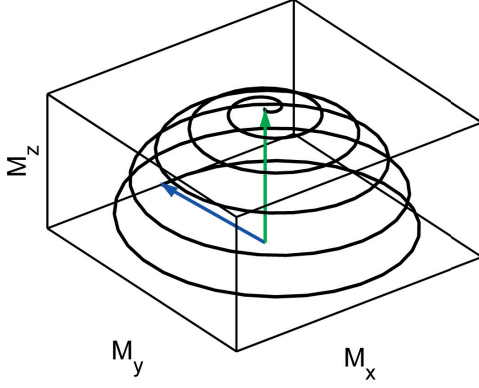
system with x, y and z axis, with M_z being the longitudinal component along the B_0 field and a transverse component M_{xy} in the x-y-plane. Since the spins precess, the gyration is causing a small rotating magnetization component in the x-y-plane. However, the protons are not precessing in phase and thus the net magnetization in the x-y-plane is zero. This state, with magnetization vectors precessing about the magnetic field with zero net magnetization in the transverse plane and with a net magnetization along the z-axis is called equilibrium magnetization (M_0).

Magnetic resonance is the exchange of energy between the spins and an electromagnetic radio frequency (RF) pulse and can be used to change the state of the magnetization vector. However, only spins with the same precessional frequency as the RF pulse frequency will respond and absorb energy. This absorption of energy is called excitation and, on a quantum level, will bring some spins to a higher energy state and into phase coherence. On a greater level, the vector of the net magnetization spirals into the transverse plane as illustrated in Figure 2.2a. From the perspective of a rotating frame of reference, meaning that the coordinate system rotates about the main direction of the magnetic field (z-axis) in the Larmor frequency, the excitation corresponds to rotating the net magnetization into the direction of the RF pulses magnetic field B_1 as illustrated in Figure 2.2b. The flip-angle α of this rotation depends on the amplitude B_1 and duration t_{RF} of the RF pulse:

$$\alpha = \gamma B_1 t_{RF} \quad (2.2)$$

For example, a 90° excitation pulse flips the magnetization vector fully into the transverse plane. Therefore, no longitudinal magnetization M_z is left (i.e. equal amount of parallel and anti-parallel spins) and all spins are in phase (i.e. full phase coherence) and generate a transverse magnetization M_{xy} after the pulse.

a. Excitation of the net-magnetization



b. Excitation of the net magnetization in a rotating frame of reference

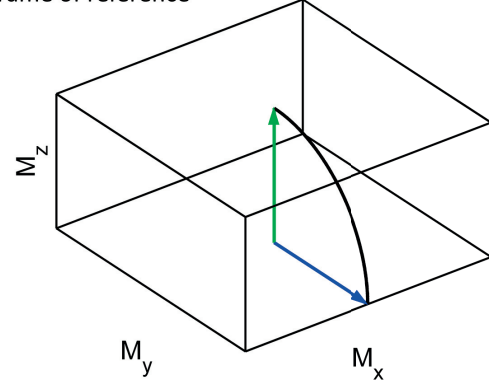


Figure 2.2: (a) Irradiating the equilibrium magnetization with a radio-frequency pulse causes the magnetization vector to spiral into the transverse plane, a process called excitation. (b) In a rotating frame of reference, the excitation corresponds to a rotation of the magnetization vector into the transverse plane, example shown for a 90° pulse. Green vectors indicate the equilibrium magnetization and blue vectors indicate the magnetization vector after the excitation.

After the RF pulse was applied, the magnetization vector returns to the equilibrium magnetization, a process called relaxation. This process can be divided in spin-lattice and spin-spin relaxation.

The spin-lattice or longitudinal relaxation corresponds to spins returning to their original, low-level energy state and is illustrated in Figure 2.3a. This loss in energy corresponds to transferring heat to the external environment (“lattice”), causing an exponential regrowth of longitudinal magnetization M_z over time t , depending on the relaxation constant T_1 :

$$M_z = M_0(1 - e^{(-t/T_1)}) \quad (2.3)$$

The spin-spin or transverse relaxation corresponds to the dephasing (i.e. spins losing their phase coherence) in the transverse plane and is illustrated in Figure 2.3b. The magnetic field of the spins interact with each other resulting in variations of their precessional rate, causing an exponential decay of transverse net magnetization M_{xy} over time depending on the relaxation constant T_2 :

$$M_{xy} = M_0 e^{-t/T_2} \quad (2.4)$$

Furthermore, the spins in the sample are often exposed to local variations in the main magnetic field, for example due to the chemical environment (e.g. iron deposition), hardware imperfections or air-tissue boundaries (e.g. at the nasal cavity). The precession frequencies of the spins vary even more due to these slight local variations resulting in an even faster

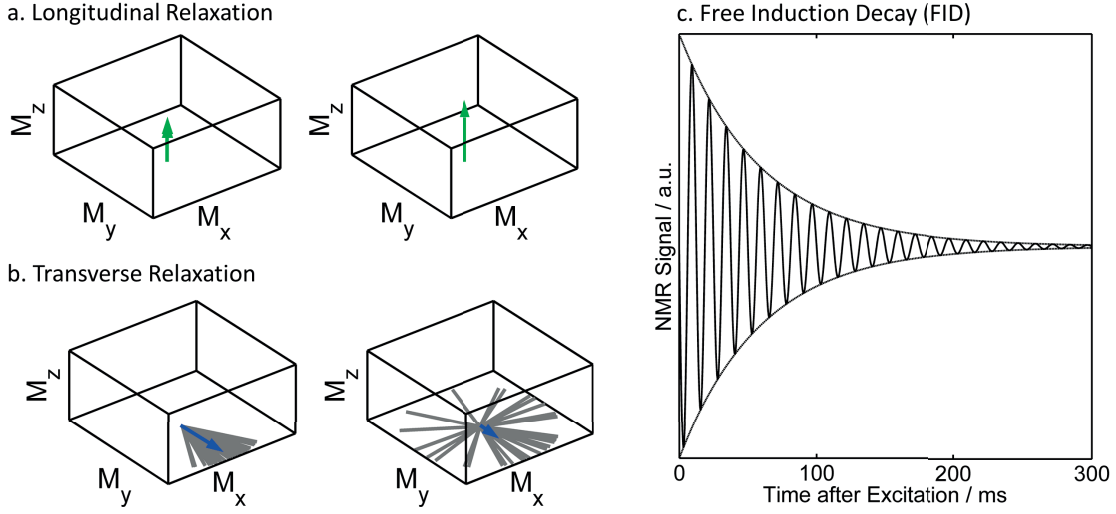


Figure 2.3: Illustration of (a) longitudinal relaxation due to spin-lattice interactions and (b) transverse relaxation due to spin-spin interaction and local field differences leading to a dephasing of spin (grey), reducing the net transverse magnetization (blue). (c) The free induction decay (FID) measured in a coil close to the sample (the Larmor frequency is reduced for visualization purposes).

dephasing. Therefore, the apparent transverse relaxation (T_2^*) is even faster resulting in a rapid exponential decrease in transverse magnetization M_{xy} .

The NMR signal is the voltage that can be measured in a coil located close to the sample. This induced voltage originates from the fluctuation of the magnetic field caused by the transverse magnetization M_{xy} . It is nearly impossible to directly measure the longitudinal magnetization since the NMR signal is very small (e.g. $1\mu T$) in comparison to the main magnetic field (e.g. $1.5T$). Therefore, only the transverse magnetization can be measured after a RF pulse was applied. After the application, the magnitude of the measured signal decreases exponentially with T_2^* as illustrated in Figure 2.3c. This NMR signal is usually referred to as Free Induction Decay (FID).

Hahn discovered the spin-echo [3]; it is an additional NMR signal that can be registered in the coils after irradiating the sample again with an RF pulse. The effect is due to rephasing

Tissue	1.5T		3T	
	T_1/ms	T_2/ms	T_1/ms	T_2/ms
Grey Matter	950	100	1331	110
White Matter	600	80	832	79.6
Cerebrospinal fluid	4500	2200	-	-

Table 2.1: T_1 and T_2 relaxation parameters for hydrogen of different human brain tissue at 1.5 T and 3 T static field strength. These values are only approximated [12, 13].

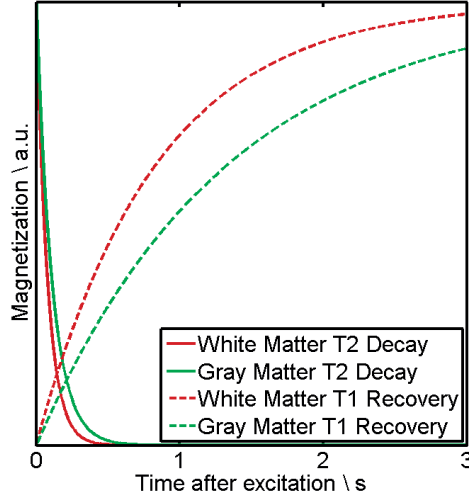


Figure 2.4: Example curves of transverse relaxation (continuous lines) and longitudinal relaxation (dashed lines) for white matter ($T_2 = 80$ ms, $T_1 = 832$ ms) and grey matter ($T_2 = 110$ ms, $T_1 = 1331$ ms).

spins after they initially dephased due to spin-spin interactions and local field variations (T_2^*). For example, when first applying an 90° RF pulse, an FID is registered in the coils that decays with T_2^* . When applying a second 180° pulse, the phase angle of the spins is inverted. Since they still precess in the same direction and frequency (within the rotating frame of reference), they start to rephase (increase spin coherence). This increase in coherence can be registered in nearby coils and is called spin-echo. After the spins refocused, they start to loose phase coherence again and the echo signal decreases again. Only the coherence that was lost due to local field differences can be refocused within the spin echo and the signal due to spin-spin interactions cannot be recovered. Therefore, the amplitude of the spin echo depends on T_2 and the echo-time TE (similar to equation 2.4):

$$M_{TE} = M_0 e^{-TE/T_2} \quad (2.5)$$

Human tissues have very different relaxation times. Example relaxation times at 1.5 and 3 T are shown in Table 2.1. These differences are the reason for the good soft tissue contrast in MRI, since the NMR signal highly depends on the relaxation time. Example T_1 and T_2 relaxation curves are shown in Figure 2.4.

2.2 Spatial Encoding

The previous section described how an NMR signal is formed and how different relaxation properties influence the signal behaviour. However, the measured signal originates always from the entire sample, thus no spatial information is encoded within the signal. In the

Chapter 2. Background

following section, it is described how an image is formed from the NMR signal using magnetic field gradients and RF pulses in pulse sequences.

Magnetic field gradients are additional magnetic fields that are added to the static main field B_0 . In contrary to the static main field, gradients can be toggled on and off (gradient pulse) and are not homogeneous. In fact, they are linear across the scanner. For example, a linear gradient in the z-direction G_z (along the main magnetic field) is positive at one end of the bore and strengthens the main magnetic field. It is negative at the other end of the bore and thus decreases the strength of the magnetic field. Between these two points the magnetic field changes linearly, whereas the gradient amplitude defines the slope of this linear field (higher amplitude results in steeper slope). This brings the advantage that spins precess with a frequency depending on their spatial location in z-direction, since the Larmor frequency depends on the magnetic field strength:

$$\omega(z) = \gamma(B_0 + zG_z) \quad (2.6)$$

Similar to the example of a gradient in z-direction, gradients can be applied in the remaining spatial dimensions: x-gradient (left-right), y-gradient (top-bottom).

The sequential application of RF pulses and gradient pulses are the foundation of spatially encoding the NMR signal. The order and timing of how these pulses are performed is described in pulse sequence diagrams. Figure 2.5 shows the example sequence diagram of a basic gradient-recalled-echo (GRE) sequence, illustrating the components which are required to spatially encode the NMR signal (RF pulses and gradients in all directions) with the vertical axis indicating amplitude and the horizontal axis indicating time.

In summary, the spatial encoding consists of three parts: slice selective excitation, phase encoding and frequency encoding. The following sections detail these three steps on the example of a GRE sequence shown in Figure 2.5.

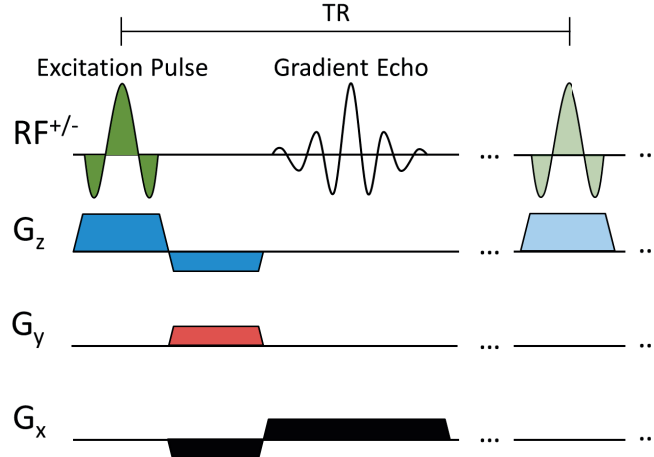


Figure 2.5: A gradient recalled echo sequence diagram with transmit and receive radio frequency (RF+/-) and magnetic field gradients (G_x , G_y , G_z).

2.2.1 Slice Selective Excitation - 2D Imaging

Probably the most straight-forward method for spatially encoding the NMR signal is to restrict the acquisition to a selected slice (plane within the MRI scanner) by applying a gradient pulse (blue in Figure 2.5) simultaneously with the excitation pulse (green in Figure 2.5). As previously mentioned, adding a magnetic field gradient results in a spatial dependency of the precessional frequency. Since only spins with the same precessional frequency as the RF pulse absorb energy (i.e. are resonant, see also Equation 2.1), only a fraction of the spins can be excited by applying an RF pulse with a range of frequencies (bandwidth) to selectively excite only certain spins. Figure 2.6 demonstrates the relationship of the RF pulse properties and excited slice. The centre frequency of the pulse ω_{RF} can be adjusted to move the slice location depending on the slice gradient G_z (see also equation 2.6). The thickness of the slice can be adjusted by either changing the pulse bandwidth $\Delta\omega$ or the amplitude of the gradient G_z :

$$\Delta z = \frac{\Delta\omega}{\gamma G_z} \quad (2.7)$$

When applying the slice-selection gradient, spins will be exposed to different local field strengths across the slice profile (z-direction). This leads to a loss in spin coherence that should be “rewinded” after the application of the pulse. This is performed by applying an additional gradient pulse with the opposite slope and approximately half the gradient moment (area under curve (AUC) of the gradient pulse). In Figure 2.5, this is shown as an additional G_z gradient (blue) with negative amplitude.

One major limitation of MRI sequences with slice selective excitation is the decrease in signal to noise ratio (SNR). The total signal intensity is decreased because the signal only comes from spins that were in the selected frequency range. Another limitation is the shape of the slice-profile. The ideal slice profile would be of a rectangular shape, meaning that the B_1 is constant through the slice in z-direction by applying a boxcar function of frequencies. According to the Bloch simulations, the waveform of the RF pulse has to be a sinc-function with infinite

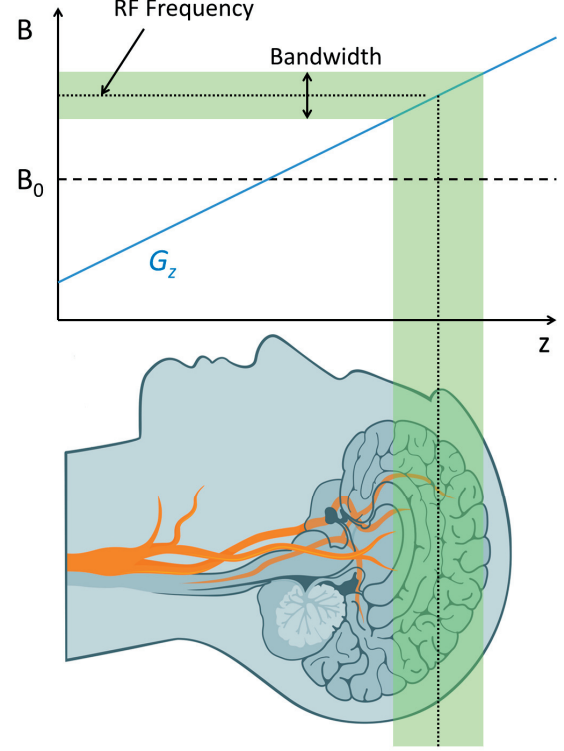


Figure 2.6: Relationship between RF pulse and gradient pulse to perform slice selective excitation. Clip art of Siemens Healthineers was used in this figure.

pulse duration to do so. Obviously, this is not feasible in reality and thus the slices-profiles are often non-ideal, e.g. with a Gaussian shaped B_1 profile, resulting in various different flip angles across the slice.

2.2.2 In-Plane Localization

The most common approach to spatially encode the spins within a slice (in-plane) is the Fourier imaging approach [10]. It is based on the Fourier theorem, stating that any signal, such as a 2D image, can be represented with a set of spatial frequencies. The common representation for these spatial frequencies is the Fourier space or in MR terminology, the k-space. K-space is complex valued and every location in k-space represents a certain spatial frequency in the image with the corresponding magnitude and phase. For example, samples in the k-space centre have low frequencies and represent the image contrast. Samples in the k-space periphery correspond to high frequencies and represent the edges of an image as it is illustrated in Figure 2.7. The inverse Fourier transform of k-space results in the image.

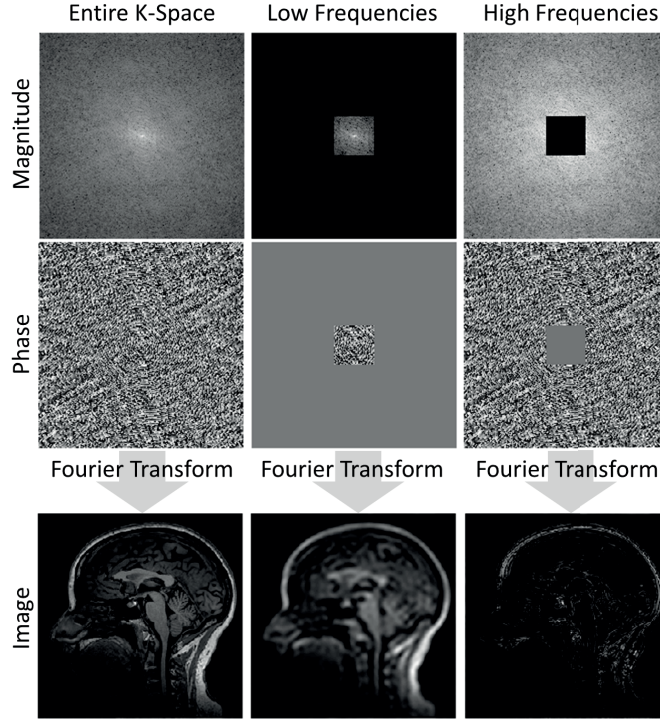


Figure 2.7: (left) K-space (magnitude and phase) of a MR image. (middle) The same k-space however with only the low frequencies and (right) only the high frequencies.

In the example of sampling k-space in a Cartesian sampling scheme, the sampling can be divided into two parts: frequency encoding and phase encoding. Frequency encoding is performed by applying a gradient during the sampling of the MR signal (black in Figure 2.5). Therefore, the MR signal will not be a single sinusoid but a mixture of many frequencies, whereas the frequency depends on the location of the spins. Therefore the measured MR signal $s(t)$ is frequency encoded and defined as:

$$s(t) = \int_x \rho(x) e^{-i\gamma G_x x t} dx, \quad (2.8)$$

with ρ denoting the spin density. For example, as demonstrated in Figure 2.8, assuming there are three objects at different spatial positions (circle, square, and triangle), the spins of these objects will precess at different frequencies due to the magnetic field gradient G_x . Therefore, the received MR signal is an integral of each individual signal from the objects and is thus composed of different frequencies. The 1D Fourier transform of this MR signal results in a projection of the different objects. In k-space, this corresponds to measuring an entire line of samples along the x-axis (also referred to as read-out) through the k-space centre.

Phase encoding is used in order to encode the last spatial domain (in this case the y-direction). It relies on repeating the frequency encoding experiment; with applying a different gradient G_y (red in Figure 2.5) for a certain time Δt_y prior to the sampling of the signal. By applying this gradient, spins will dephase depending on their location along the y-direction as demonstrated in Figure 2.9. After applying the gradient, spins will return to precess at the same frequency, however, the accumulated phase difference remains. The MR signal that is acquired afterwards is thus phase encoded and defined as:

$$s(t) = \int_x \int_y \rho(x, y) e^{(G_x x t + G_y \Delta t_y y)} dx dy \quad (2.9)$$

In k-space, this corresponds to shifting the acquired k-space line in the y-direction. The stronger the applied gradient, the further away is the acquired line from the k-space centre. This also means that for a high resolution image with an example matrix size of 256x256, the process of phase encoding and frequency encoding has to be repeated 256 times since so many lines are required. This leads to the typically long acquisition times of MRI. Also because it cannot be repeated immediately since spins usually require a longer time to fully relax (mostly depending on T_1). Usually, a long delay between excitation pulses, termed repetition time TR, with up to 4 s is required (depending on the sequence) before another k-space line is acquired. In the previous example of a matrix with 256 lines, it would require a total of 17:04 min to acquire the k-space of a single slice. This highly depends on the sequence type (see section 2.3). Furthermore, new acceleration techniques were developed and are described in section 2.6.

To summarize, with the Fourier imaging approach, gradients are used to manipulate the

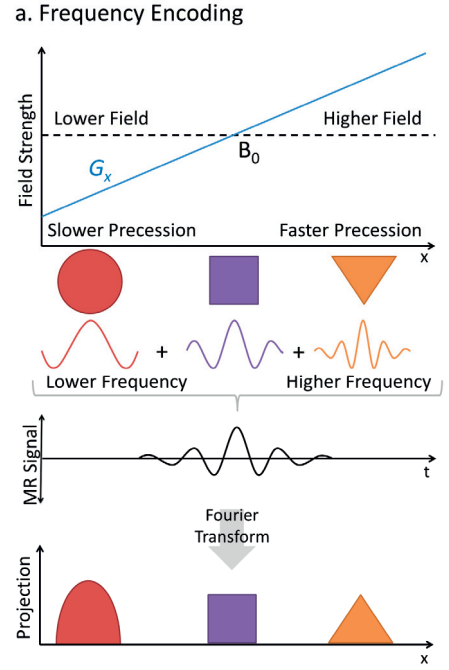


Figure 2.8: Frequency encoding of the MR signal by applying a gradient during sampling results in spins contributing to the signal with different frequencies depending on their location.

a. Phase Encoding

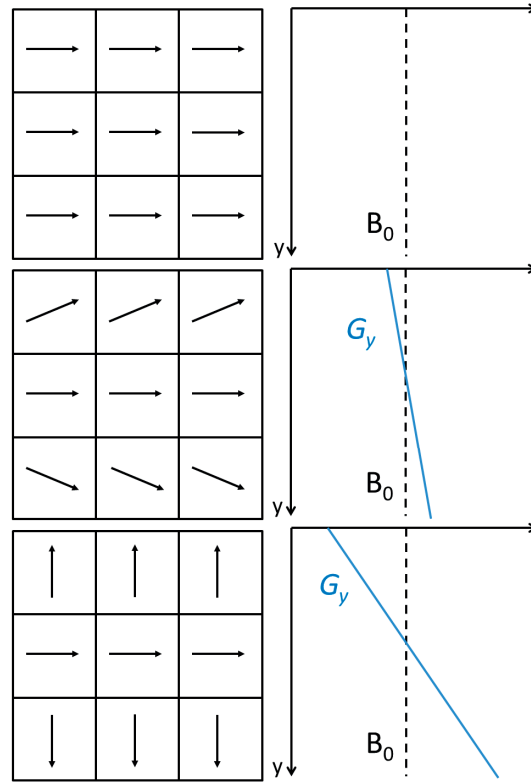


Figure 2.9: Accumulated phase of spins after applying no Gradient (top) a gradient with low amplitude (middle) and a gradient with high amplitude (bottom) along the y-direction.

MR signal in a way that all frequencies in k-space (k-space samples) are measured. After all samples were received (k-space is fully sampled), an inverse Fourier transform is applied to obtain the MR image.

2.2.3 Non Selective Excitation – 3D Imaging

Optionally to a sequence design using slice selection, a non-selective RF pulse can be used for excitation. Hence, no slice selecting gradient G_z is applied during the application of the RF pulse. Therefore, all spins within the homogeneous field of the scanner and not just within a 2D plane get excited. Consequently, acquisitions using this type of excitation are termed 3D sequences.

When using a 3D sequence, an additional dimension has to be spatially encoded by phase encoding. Therefore, not only a gradient in y-direction G_y but also a gradient in z-direction G_z is applied for a certain amount of time Δt_z prior to the frequency encoding step. Consequently,

k-space becomes 3D and the acquired MR signal is defined as:

$$s(t) = \int_x \int_y \int_z \rho(x, y, z) e^{(G_x x t + G_y \Delta t_y y + G_z \Delta t_z z)} dx dy dz \quad (2.10)$$

The final image volume is then achieved by performing a 3D Fourier transform.

Using this 3D approach, the MR signal is obtained from all spins within the scanner and therefore the SNR increases in comparison to a 2D approach with only a restricted amount of spins. Nevertheless, more repetitions are required to fill the entire 3D k-space, resulting in longer acquisition times. Furthermore, some sequence designs may not even be possible in 3D due to specific absorption rate (SAR) limitations.

The SAR quantifies how much energy is absorbed by the tissue and is defined as:

$$SAR = \frac{1}{V} \int_r \frac{\omega(r) |E(r)|^2}{\rho(r)} dr \quad (2.11)$$

with ω denoting the tissue conductivity, V the sample volume and E the electrical field of an RF pulse. The absorption of energy results in a temperature increase of the tissue that may pose safety problems. Therefore, an international guideline was defined that limits the SAR of MR sequences. Non-selective 3D pulses often result in much higher SAR in comparison to 2D pulses. Consequently, in some cases, they cannot be used due to safety constraints.

Despite the limitations, 3D imaging allows for isotropic high-resolution images (e.g. 1 mm x 1 mm x 1 mm voxel size) and may become standard in future clinical routine.

2.3 MR Pulse Sequence Designs

The contrast in an MR image highly depends on the order and configuration of the applied RF and gradient pulses, i.e. the sequence design. Every sequence design has advantages and disadvantages. This variability has produced numerous variations that were published ever since the NMR signal was discovered.

In previous sections the gradient echo sequence (see section 2.2) and a spin-echo (see section 2.1) were briefly explored. In the following sections, it is described how to use these types of MR acquisitions techniques to sample frequencies in k-space and how the contrast of the resulting images is manipulated by changing parameters in the sequence design.

2.3.1 Spin-Echo sequence

The spin-echo (SE) sequence is based on the discovery of Hahn that spins can be refocused after the application of an additional RF pulse to generate an additional NMR signal (see 2.1

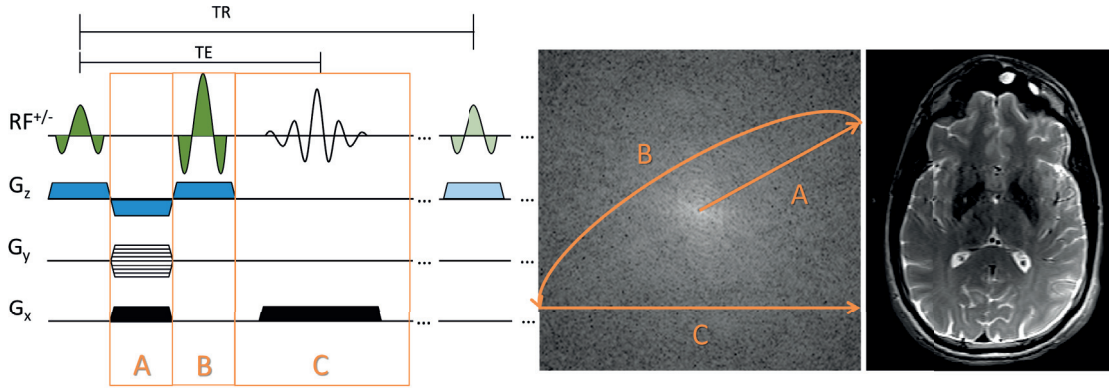


Figure 2.10: (left) An example of a spin-echo sequence, (middle) the corresponding k-space trajectory and (right) an example image with $TE = 100\text{ ms}$ and $TR = 3\text{ s}$.

for more detail). A basic SE sequence is illustrated in Figure 2.10. First a slice-selective 90° excitation pulse is applied. In k-space, this corresponds to starting the trajectory in the k-space centre. Subsequently, the phase encoding and the frequency prewinder gradients are applied to move the trajectory away from the k-space centre (required for spatial encoding). Then, at half way through the echo time, a 180° RF pulse is applied that inverts the phase of the spins causing them to refocus. Finally, a conventional frequency encoding is performed to sample a k-space line during the SE.

The advantage of this sequence is that the inversion of the phase cancels the effects of local field inhomogeneity. Hence, the image contrasts mostly depends on the equilibrium magnetization M_0 and the transverse relaxation T_2 , whereas a long TE increases the sensitivity to T_2 . However, when choosing a short TR, the spins do not have enough time to fully relax (according to T_1) before the next excitation pulse is applied. Therefore, various different contrasts can be achieved with a spin-echo sequence depending on TE and TR as summarized in Table 2.2.

	Short TE	Long TE
Short TR	T_1 -weighted	(commonly not performed)
Long TR	Proton-density-weighted	T_2 -weighted

Table 2.2: Image contrast of a spin-echo sequence depending on echo-time TE and repetition time TR.

It should be noted that multiple spin-echoes can be generated within one TR when applying multiple refocusing pulses. This variant of the spin echo sequence is usually referred to as multi-echo spin-echo (MESE). It is also called Carr-Purcell-Meiboom-Gill (CPMG) sequence if there is a 90° phase shift between excitation and refocusing pulse. The signal amplitude of each echo in a CPMG sequence decrease corresponding to T_2 relaxation and can thus be used to quantify T_2 (see section 2.5.1). Optionally, these multiple echoes can be used to sample multiple k-space lines within one TR to accelerate the acquisition, usually referred to as fast

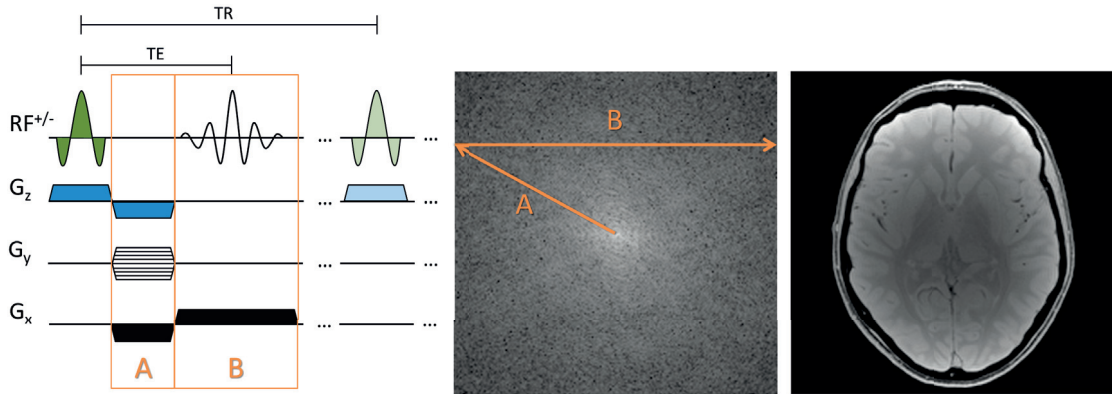


Figure 2.11: (left) An example of a gradient-recalled echo sequence, (middle) the corresponding k-space trajectory and (right) an example image with $TE = 4.3$ ms.

spin-echo (see section 2.6.1).

2.3.2 Gradient Recalled Echo Sequence

The GRE sequence starts with an excitation pulse. The flip-angle of this pulse can be varied and is usually lower than 90° . Again, in k-space, this corresponds to starting the trajectory at the centre as illustrated in Figure 2.11. The magnetization that was flipped into the transverse plane is then dephased by applying the phase-encoding and frequency prewinder gradients. This corresponds to moving the k-space trajectory away from the k-space centre. Subsequently, frequency encoding is performed to sample one line in k-space. Since there was no 180° pulse to invert the phase, the acquired signal is also dependent on local field inhomogeneity (T_2^*) and inhomogeneity of the main magnetic field (B_0) that usually result in signal voids close to air-tissue boundaries (e.g. above the nasal cavity). An advantage of the GRE sequence is that not all the longitudinal magnetization is flipped into the transverse plane (depending on the flip-angle). Hence, spins require less time to return to the equilibrium magnetization and a short TR can be used, yielding faster acquisition times than a SE sequence.

If the GRE sequence has a very short TR (i.e. $TR \ll T_2$), then besides a not fully relaxed T_1 magnetization, also a residual transverse magnetization is present before the next excitation pulse is applied. If this magnetization is undesired, for example for T_1 -weighted contrasts, a gradient or RF spoiler can be applied to destroy the transverse magnetization. The sequence is then usually referred to as spoiled gradient recalled echo (SPGR) or fast-low-angle-shot (FLASH) sequence. The resulting contrast mostly depends on T_2^* (longer TE, more T_2^* -weighting) and T_1 (higher flip-angle, more T_1 -weighting).

In some cases, the residual transverse magnetization is desired. Therefore no spoilers are applied and the contrast depends on the ratio T_1/T_2 . Furthermore, the phase is rewinded to avoid a dependency to the phase encoding. Moreover, to avoid artifacts from rapid flow (e.g. blood-flow); the integral of the applied gradients in all directions should be zero by

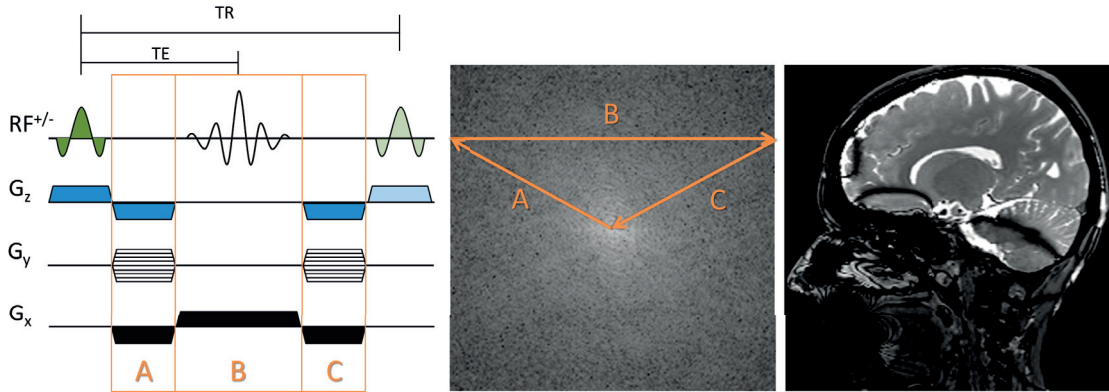


Figure 2.12: (left) An example of a balanced steady state free precession sequence, (middle) the corresponding k-space trajectory and (right) an example image showing typical banding artifacts in the frontal lobe, above the nasal cavity and cerebellum.

the end of the TR. In k-space, this corresponds to returning to the centre before the next excitation is applied as illustrated in Figure 2.12. The sequence is usually referred to as balanced Steady State Free Precession (bSSFP) sequence. The short TR and the T_1/T_2 contrast results in a fast sequence that has an excellent SNR. Therefore, bSSFP is often used to acquire high resolution images, e.g. of the nerves in the inner ear. However, the MR signal is very sensitive to inhomogeneity in the main magnetic field B_0 . Therefore, bSSFP images often exhibit signal-voids that are referred to as banding artifacts.

2.3.3 Magnetization Preparation

The previously described sequence designs have a typical contrast which often depends on the used sequence parameters. Magnetization preparation can be applied to further weight the contrast towards a tissue property. For example, an adiabatic 180° pulse can be applied to fully invert the equilibrium magnetization. Afterwards, spins return to the equilibrium magnetization depending on T_1 relaxation according to:

$$M_z(t) = M_0(1 - 2e^{-t/T_1}) \quad (2.12)$$

Hence, a T_1 contrast is imprinted into the contrast if a conventional imaging sequence is used to acquire k-space after a delay (in-version time TI). This type of magnetization preparation is called inversion recovery. The most famous acquisition types that use inversion recovery are magnetization prepared rapid acquisition GRE (MPRAGE) and fluid attenuated inversion recovery (FLAIR)

MPRAGE uses an inversion pulse to imprint a strong T_1 contrast into the image before it uses a fast GRE sequence to sample the MRI signal. In the example of the brain, an excellent contrast between white matter (WM) and grey matter (GM) is achieved due to the differences

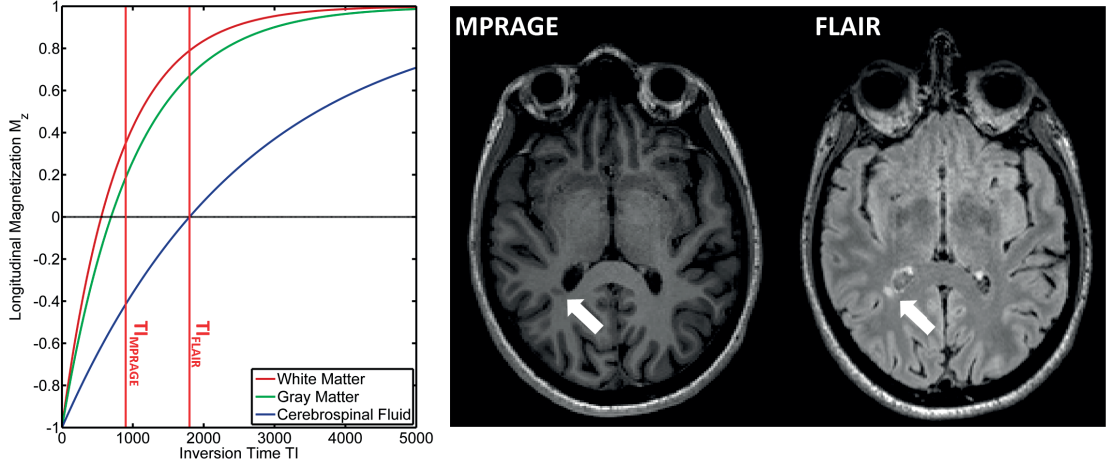


Figure 2.13: (left) Recovery of longitudinal magnetization in different tissues after an inversion pulse and example inversion times (TI). (right) Example MPRAGE and FLAIR contrast of a multiple sclerosis patient with a white matter lesion indicated with white arrows.

of the relaxation curves at the inversion time TI_{MPRAGE} . In contrary, FLAIR imaging uses the inversion recovery to null the signal from cerebrospinal fluid (CSF). To that end, TI_{FLAIR} is selected to be at the time when the magnetization of CSF is zero. Consequently, the fast spin-echo sequence that is typically used to sample k-space has no signal from CSF and imprints an additional T_2 contrast. This combined contrast of nulled CSF and T_2 -weighting is often used in clinical routine to search for lesions.

Figure 2.13 shows example relaxation curves of different brain tissues after an inversion pulse and example images for an MPRAGE and FLAIR sequence of a multiple sclerosis patient. Other known magnetization preparation methods are T_2 preparation to imprint T_2 relaxation, fat-saturation to remove the signal of fat or magnetization-transfer preparation to imprint the presence of macromolecules, diffusion and perfusion among many others.

2.4 Instrumentation

In the previous sections, the methods to go from protons, over a NMR signal, to an image were explained mentioning necessary components such as an external static field (B_0), a RF field (B_1), field gradients (G_x, G_y, G_z) and coils that receive the NMR signal. The following paragraphs give a brief overview of the used instrumentation of these components and how they enable to generate an image on a typical clinical scanner.

A homogeneous main static field (B_0) is a fundamental component of a MRI scanner. Different types of magnets were developed in the past: superconducting magnets, permanent magnets, and resistive and electromagnets. The most common type in clinical scanners is the superconducting magnet. It uses a strong current in a coil around the opening (bore) of the scanner to generate a horizontal magnetic field. The coil is made from conductors that have ideally no

resistance so that the current strength never decreases (superconductor). Helium is used as a cryogenic cooling fluid to cool down the superconductor to almost absolute zero temperature (-273.15°C) and reduce the resistance to almost zero. For superconducting magnets, the magnetic field is permanent, meaning that the field can only be ramped down by boiling off the liquid helium (quench). Usually this strong magnetic field extends beyond the magnet in all directions and thus poses a security risk. Most modern scanners are actively shielded to reduce these fringe fields. Actively shielded magnets use a coil design with opposite currents around the main coil to partially cancel the field outside the scanner.

In order to excite spins, a RF field (B_1) is required. Usually, a coil to excite the body (bodycoil) is built into the scanner hull to apply this RF field. The same coil can be switch from transmit to receive mode and thus be used to measure the NMR signal. The sensitivity of a coil to the signal from spins also depends on the distance between them. Therefore, coils are often designed for specific body-parts in order to place them closer to the region of interest. Examples are the head/neck-, foot/ankle-, spine-, and rectal-coils. The sensitivity of a coil can be spatially mapped resulting in sensitivity maps often used in modern reconstruction algorithms. The specialized coils often have more than one coil-element and are then referred to as multi-channel coil or coil-array. A modern, commercial head/neck coil can have up to 64 channels that facilitates higher acceleration of imaging sequences as explained in more detail in section “2.6 Accelerated MRI”.

Since the frequencies used in MRI are in bandwidths similarly to the frequencies we use in other life situations (e.g. radio and communication), the scanner room is shielded to avoid interference with the NMR signal. The RF shielding is realized by surrounding the scanner with a Faraday cage. Therefore, the scanner door has to be shut during scanning to close the cage. A set of three gradient coils (one for each spatial dimension) are integrated directly into the bore of the scanner and are used to produce spatially varying field strengths required for image encoding. The fields are generated by inducing a carefully controlled current into the coils as defined by the pulse sequence design. The loud noise that can be heard during the MRI acquisition originates from these gradient coils, because the conducting material vibrates due to rapidly changing currents.

In the example of a MRI scanner of Siemens (Erlangen, Germany), a network of three computers is used to control the scanner and execute the desired sequences. The host computer is the interface to the technician who operates the scanner by registering the patient information and selecting the desired imaging protocols. Once a sequence is started, the Scanner Control Unit is used to calculate and perform the required voltage and waveform for gradient and RF-pulses by directly controlling the scanner hardware. The received and analogue-digital converted MR signal is then send to the image reconstruction computer that applies the appropriate calculations to compute the image that will be finally displayed on the host computer.

Figure 2.14 shows a schematic drawing of all mentioned components and their connections.

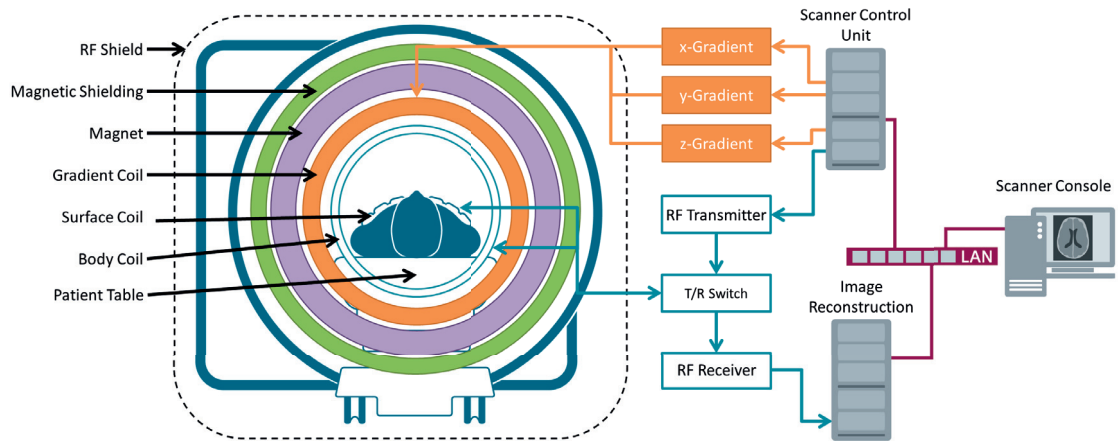


Figure 2.14: Schematic drawing of a MRI scanner and its components that are required to generate an image. Clip art of Siemens Healthineers was used in this figure.

2.5 Quantitative Magnetic Resonance Imaging

The sequence designs introduced in the previous chapter are all qualitative measures, meaning that the image contrast may be weighted towards a tissue property, but the intensities are not directly linked to a tissue property. Furthermore, intensities will vary when changing any sequence parameters (e.g. TR, TE and TI). Also, the contrast may depend on experimental conditions such as the B_0 homogeneity in a GRE sequence. To achieve better comparison, qMRI aims at directly measuring the tissue property, independent from the used sequence, hardware and parameters.

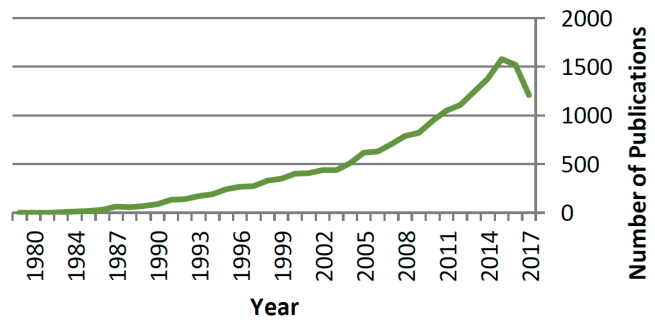


Figure 2.15: Number of publications per year according to PubMed search with the query “quantitative magnetic resonance imaging”.

In general, qMRI often acquires multiple qualitative images whereas one sequence parameter is varied for each acquisition which changes the signal intensity. A model of the spin behaviour is used to link this change in signal intensity to one or more tissue properties. Since multiple acquisitions are required, qMRI often results in long acquisition times. Furthermore, the accuracy of the quantification often depends on the accuracy of the spin model. Hence, in qMRI, there is a balance between acquisition-time and accuracy, resulting in sheer endless published methods in qMRI as shown by the number of publications by year in Figure 2.15.

The following sections will focus on the quantification of T_1 and T_2 starting from the more

basic methods and continue with more sophisticated faster acquisition methods.

2.5.1 T_2 Mapping

The most straight forward approach to quantify T_2 is using a SE sequence. As discussed earlier, the amplitude of a spin-echo depends on the tissue properties M_0 , T_2 and the sequence parameter TE (see equation 2.5). Therefore, to quantitatively map T_2 , a spin-echo sequence can be used to acquire multiple images with different TE's. Subsequently, a voxel-wise fitting is performed to find the best combination of T_2 and M_0 to represent the acquired data with the mono-exponential signal-model (equation 2.5). Notably, this assumes that the longitudinal magnetization fully recovers during the TR.

This approach often yields very accurate T_2 values. Its major drawback is the required acquisition time. For example, to acquire a T_2 map with a spin-echo sequence of a matrix size 256x256; with a TR of 4 s and only two echo times TE. The resulting acquisition time is approximately 34 min (TR x Number of Lines x Number of TE). However, sampling only two echoes will lead to high noise susceptibility. Therefore 16 echoes are commonly used, which linearly scales the acquisition time to 4:32h. Obviously, such long acquisition times are impractical and not feasible in a clinical setting.

To accelerate the acquisition, a CPMG sequence can be used to sample all echoes within a single TR by applying multiple 180° refocusing pulses. The example above would then result in an acquisition time of 17 min (TR x Number of Lines) which is much shorter in comparison to 4:32h. This approach has become the standard for quantitative T_2 mapping, but is still rarely used in clinical routine.

One problem arises when using a CPMG sequence for quantitative T_2 mapping. The signal-model (equation 2.5) only applies if the used refocusing pulses accurately invert the phase of the spins, which requires a homogeneous B_1 field and ideal (rectangular) slice profiles (see section 2.2.1). Since these requirements are difficult or even impossible to achieve, the acquired signal deviates from the signal-model. An additional T_1 related signal is superimposed on the mono-exponential decay which is called stimulated echo and causes an overestimation of T_2 . Several methods were proposed to mitigate this effect, for example by ignoring the first echo [14], estimating and removing the systematic bias [15] or directly fitting the stimulated-echo signal model [16, 17, 18].

Alternatively, other sequence designs can be used to estimate T_2 , e.g. by using a GRE acquisition. However, the GRE contrast does not directly depend on T_2 , but a T_2 magnetization preparation can be used to imprint a T_2 contrast. Again, this has to be repeated for various different T_2 weightings and the corresponding signal model has to be fitted to this series of images. This approach is still sensitive to B_1 inhomogeneity and is influenced by T_1 but showed good results in cardiac imaging [19]. A major advantage of the method is that it only requires a 180° pulse in the magnetization preparation but not in the actual acquisition of the

image. Therefore, it can be used as a 3D sequence without exceeding SAR limitations.

2.5.2 T_1 Mapping

The most basic and probably most accurate approach for quantitative T_1 mapping is using an inversion recovery in combination with a SE sequence. After an adiabatic inversion pulse, the longitudinal magnetization returns to the equilibrium magnetization according to T_1 . Therefore, when acquiring multiple spin-echo images at different inversion times TI, the signal-model of the recovery (equation 2.12) can be fitted to estimate M_0 and T_1 . This combination results in long and impractical acquisition times, similar to T_2 mapping with a single SE sequence.

Therefore, the Look-Locker approach aims at sampling the recovery curve at multiple TI within a single TR by tipping the magnetization into the transverse plane during the recovery with only a small flip-angle and performing a GRE readout. This allows getting images at different TI in a shorter acquisition time than a SE inversion recovery approach. However, the fitted T_1 values will be biased because the signal-model does not fully apply any more, since the magnetization gets partially flipped into the transverse plane. A retrospective correction has to be applied to correct this systematic bias.

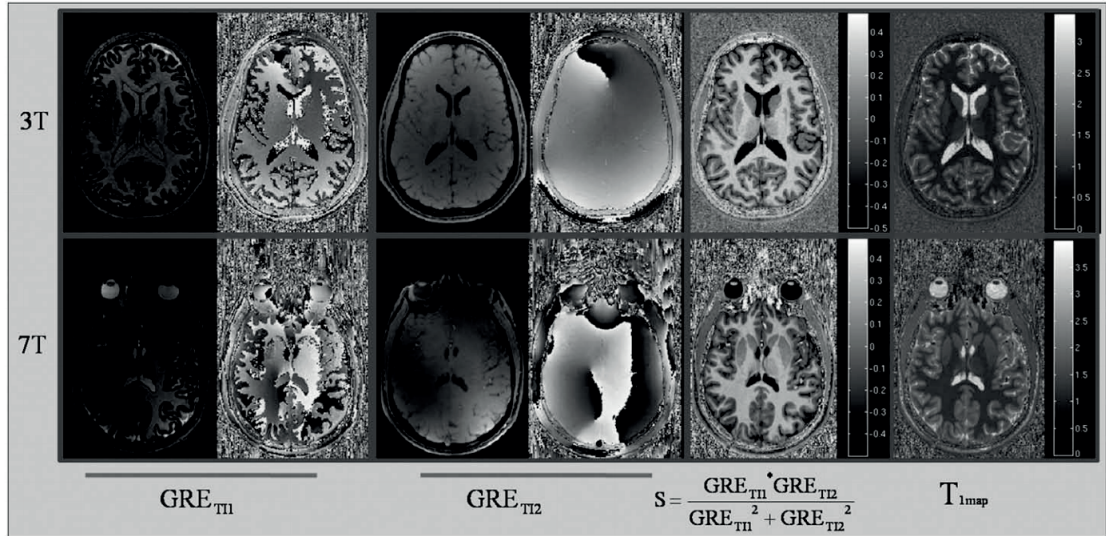


Figure 2.16: The GRE images (magnitude and phase) at different inversion times (T_{I1} and T_{I2}) that are used to generate the typical MP2RAGE contrast at 3T and 7T. Additionally, a T_1 map is generated. This figure is from the original publication of Marques et al. [20] (License-No.: 4191921011271).

The MP2RAGE [20] sequence is a similar approach that further shortens the scan time. It was originally developed to generate bias-free T_1 weighted images as shown in Figure 2.16. To that end, two GRE image readouts are used after an inversion pulse to sample multiple k-space lines for two images at two different TI's. During the image reconstruction, these two

images are combined in a way that the intensity bias cancels. Therefore, the resulting contrast depends mostly on T_1 . This direct dependency can be simulated (e.g. Bloch simulations) and used to estimate a T_1 map.

Variable-flip-angle (VFA) T_1 mapping is yet another way to quantify the longitudinal relaxation. It uses multiple SPGR acquisitions where the T_1 weighting is varied by changing the flip-angle α . The measured transverse magnetization mostly depends on the TR, T_1 , α and K (mixture of M_0 and T_2^*) according to the signal model:

$$M_{xy} = K \frac{1 - e^{-\frac{TR}{T_1}}}{1 - \cos \alpha e^{-\frac{TR}{T_1}}} \sin \alpha \quad (2.13)$$

The T_1 map is estimated by fitting this signal model to the data. Nevertheless, the accuracy highly depends on the homogeneity of the B_1 field and often requires a retrospective correction of the values according to an estimate of the B_1 inhomogeneity.

2.5.3 Multi Parametric Mapping

Besides the classical approaches that aim at either mapping T_1 or T_2 , multi-parametric mapping approaches aim at estimating them simultaneously.

For example Driven-Equilibrium Single-Pulse Observation of T_1 and T_2 (DESPOT1 and DESPOT2) [22] estimates first T_1 using a SPGR sequence in a VFA approach. Subsequently, a bSSFP sequence is acquired. Therefore, T_2 can be derived since its contrast depends on the T_1/T_2 ratio and T_1 is known from the SPGR sequence. DESPOT proved to provide relaxation values as a 3D sequence with short acquisition time, however, is sensitive to B_1 inhomogeneity (see also the VFA-SPGR approach) and the typical banding artifacts of bSSFP acquisitions.

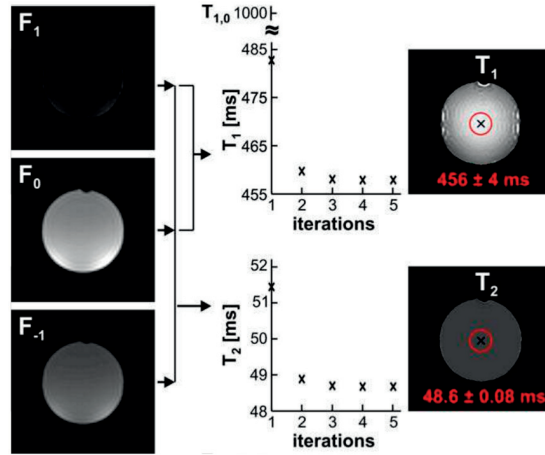


Figure 2.17: Example echoes (F_1 , F_0 and F_{-1}) from a TESS sequence and example T_1 and T_2 maps of a spherical phantom. This figure is from the original publication of Heule et al. [21] (License-No.: 4191920363996).

Another approach to simultaneously map T_1 and T_2 is triple echo steady state (TESS) [21].

It is based on an unbalanced steady state sequence, meaning it is a GRE sequence with a TR « T_2 and the integral off the gradient moment is not zero. In this configuration, the sequence generates three echoes within a single TR as shown in Figure 2.17. The relative amplitudes of these echoes depend on T_1 and T_2 and thus a signal-model can be fitted to estimate the

two parameters. TESS shows good accuracy on estimating T_2 , however the estimation of T_1 appears underestimated and B_1 sensitive. Furthermore, the acquisition is sensitive to flow and motion since it is an unbalanced SSFP sequence.

Probably the most recent and prominent approach for multi-parametric mapping is MR fingerprinting (MRF) [23]. MRF moves away from a classical sequence design with steady states towards a pseudo-random acquisition. The signal response (fingerprint) is ideally unique for each combination of tissue properties. To map T_1 and T_2 , spin-models are used to create a dictionary of simulated signal responses for a range of T_1 and T_2 values (e.g. using Bloch or the extended-phase-graph (EPG) simulations). The actual acquired signal is compared with each dictionary entry. The T_1 and T_2 values of the entry that best fits the acquired signal are assumed to be the real tissue properties. This innovative approach had a large impact in the MR community and may be a big leap towards a fully quantitative MRI exam. However, the accuracy of T_1 and T_2 depends on how well the spin-model reflects the actual micro structure of the tissue, leaving potential room for improvement to this new technology.

2.5.4 Synthetic Contrasts

Ever since MRI was introduced to the clinical work flow, radiologists were trained and many medical guidelines were developed on images with weighted contrast. When suddenly introducing qMRI to the clinic, this experience and guidelines would be lost. This may also be one of many reasons why the transition from qualitative to quantitative MRI is a long term process.

One way to address this problem is synthetic weighted contrast. The parametric maps that were determined with qMRI techniques could be used in conjunction with the known signal-models to artificially create images with the same contrast as conventional imaging. In this way, the well-known contrast, on which radiologists were trained, is provided besides the quantitative information.

For example, after estimating T_2 and M_0 , the forward signal-model of the spin-echo sequence (equation 2.5) can be used to generate a T_2 weighted image with any TE. With that approach, the conventional image contrast is generated synthetically from a qMRI sequence without requiring additional weighted sequences. The conventional imaging techniques may then be replaced by qMRI techniques if the synthetic contrast is at least equally good as the conventional contrast.

2.6 Accelerated MRI

One major disadvantage of MRI in comparison to other imaging modalities, such as CT, is the long acquisition time required to sample the entire k-space. In the past, an entire field of research has focused on accelerating the MR acquisition. Several approaches were proposed in

the course of this research. In the following sections, some of these approaches are presented.

2.6.1 K-Space and Sequence Sampling Techniques

Segmented acquisitions are one of many ways to accelerate MRI. In segmented approaches, it is attempted to generate multiple echoes within a single TR that allows sampling multiple k-space lines. The acquisition is faster since now less TR's are required to fully sample k-space.

For example, the segmented acquisition of a T_2 -weighted image, usually named “Rapid Acquisition with Relaxation Enhancement” (RARE) or fast spin-echo (FSE) [24] is filling k-space using multiple refocusing pulses after excitation in order to acquire multiple k-space lines within one TR. Further acceleration can be achieved by using the Gradient- and Spin-Echo (GRASE) technique, which generates multiple gradient echoes on top of a spin echo [25]. These gradient echoes are exploited to acquire multiple different k-space lines on a spin-echo, yielding even more lines per TR. However, filling k-space with data acquired at different echo times leads to blurring. Moreover, the addition of gradient echoes may lead to unwanted sensitivity to magnetic field inhomogeneity (B_0) and susceptibility differences (T_2^*).

Partial Fourier imaging is another technique to accelerate an acquisition. This technique samples only a fraction of k-space $>50\%$ and exploits the conjugate symmetry of k-space in the image reconstruction. However, in doing so, the resulting image becomes more susceptible to system imperfections.

Interleaved slice sampling is a widely used acceleration technique in 2D imaging. Sequence designs with a short acquisition but long TR (e.g. spin-echo) have a long unused delay until another excitation is performed. Interleaved slice sampling exploits this down-time and performs the data acquisition of other slices.

2.6.2 Parallel Imaging

MR data is sampled in the Fourier domain (k-space) and it can be mathematically shown that a certain amount of data has to be sampled to allow reconstructing of an image free of aliasing artifacts (termed the Nyquist-Shannon sampling theorem). However, parts of the sampled k-space data might be redundant or prior knowledge might be used to synthesize parts of the data, which offers the possibility to sample less (undersample) data than the Nyquist theorem demands. This leads to a reduction in acquisition time, because in a typical scan the acquisition time scales with the amount of data sampled. More advanced reconstruction techniques are required to incorporate prior-knowledge about the expected MR signal within the reconstruction to exploit redundancies in the data and thus facilitate undersampling.

Parallel imaging techniques such as generalized autocalibrating partially parallel acquisition (GRAPPA) [26] and sensitivity encoding (SENSE) [27] are prominent examples of undersampled acquisitions and are commonly used in clinical routine. These techniques exploit the data

redundancy generated by multiple receiver coils in order to recover missing k-space samples, thus reconstructing an artifact free image.

GRAPPA assumes that a missing k-space sample (target sample) can be interpolated by a linear combination of its neighbours and its representation in all receiver coils (source samples) as it is illustrated in Figure 2.18. This prior knowledge is used to retrieve missing k-space lines by first, train this linear dependency (autocalibration), and second, use the previously learned dependencies to synthesize missing k-space points.

The linear dependency of a k-space sample to its neighbouring samples can be mathematically described using a matrix representation as following,

$$t = W * s, \quad (2.14)$$

where t is a vector of one target sample represented in each coil element and s a vector of source samples for each coil element. The linear dependency between vector t and s is described by a matrix of weights W . GRAPPA assumes that these weights are identical for each sample in k-space. Thus, the weights can be determined by fitting them in a least squares sense onto a fully sampled calibration dataset using the following equation:

$$W = T * S^H (S^H S)^{-1}, \quad (2.15)$$

where T and S are matrices containing multiple target t and source vectors s , collected from the calibration dataset. Finally, the previously found weights are used to synthesize missing samples (target samples) by applying equation 2.14 onto its neighbours (source samples). K-space is fully sampled after the missing samples were reconstructed and a direct inverse Fourier transform and coil combination (e.g. sum of squares reconstruction) are applied to retrieve the desired image without major aliasing artifacts.

In contrary to GRAPPA, the parallel imaging approach SENSE performs the reconstruction in image space. It requires an estimate of the coil sensitivities which is derived from either a fully sampled k-space centre or an additional low-resolution acquisition. This prior knowledge can then be used to remove the undersampling artifacts (folding) from the image, for example by

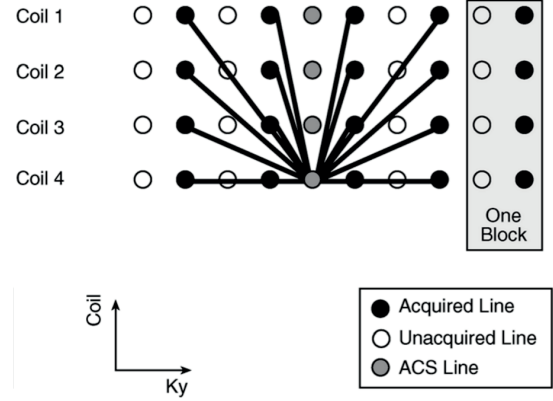


Figure 2.18: Illustration of the linear dependency in parallel imaging, using multiple receiver channels. This figure is from the original publication of Griswold et al. [26] (License-No.: 4191920647937).

using a conjugate gradient SENSE reconstruction (cg-Sense). In a cg-SENSE reconstruction, an inverse problem is formulated that models the entire reconstruction process in a cost function:

$$X = \arg \min_X \frac{1}{2} \sum_{c=0}^N \|PF\{S_c X\} - Y_c\|_2^2, \quad (2.16)$$

with X denoting the current estimate of the image, P the binary sampling mask, F the Fourier transform, S the coil sensitivities, Y the undersampled data and N the number of coils. A conjugate gradient descent [28] is used to minimize this cost-function, iteratively removing the image artifacts. This cost-function is often the basis for iterative image reconstructions such as compressed sensing.

2.6.3 Compressed Sensing

Another approach, compressed sensing, is a technique introduced in signal processing by Donoho in 2006 [29] and first applied in MRI by Lustig et al. [30]. Compressed sensing uses the prior knowledge that the acquired image has a sparse representation in some basis as shown in an example for the wavelet domain in Figure 2.19. In other words, compressed sensing assumes that the MR image is compressible. For a compressed sensing acquisition, k-space is incoherently sampled, thus noise-like artifacts appear in the image when a direct inverse Fourier transform is performed. To remove the artifacts caused by the undersampling, an iterative reconstruction similar to cg-SENSE is used, but with the addition of regularization that enforces sparsity by penalizing coefficients in some domain (e.g. Wavelet, finite difference) with a l1-norm:

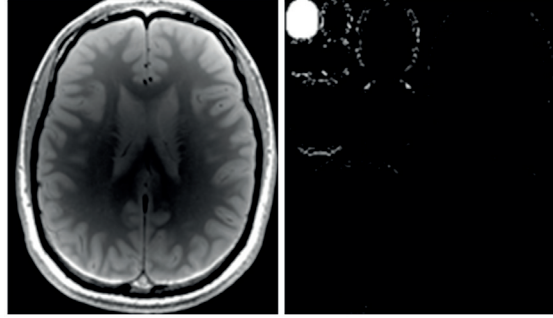


Figure 2.19: An example image (left) and its sparse representation in the wavelet-domain (right).

$$X = \arg \min_X \frac{1}{2} \sum_{c=0}^N \|PF\{S_c X\} - Y_c\|_2^2 + \lambda \|\Psi\{X\}\|_1 \quad (2.17)$$

with Ψ denoting the wavelet transform and λ a regularization parameter which is usually manually tuned to adjust how much sparsity is enforced.

Usually, acquisitions for quantitative imaging possess an additional dimension besides the spatial dimensions which is used for the fitting of the signal model. This dimension is referred to as parametric dimension and is for example the TE direction in T_2 mapping. This domain

is exploited by compressed sensing algorithms by finding an operator that transforms this dimension into a sparse representation, facilitating higher acceleration factors compared to a compressed sensing reconstruction using only spatial regularization. Velikina et al. describes the basic concept of compressed sensing in parametric mapping [31]. Another compressed sensing approach for quantitative mapping was proposed by Doneva et al., suggesting a sparse representation by applying an over-complete dictionary, learned from the data model [32].

2.6.4 Model-Based Reconstruction

Model-based iterative reconstruction algorithms use a physical model of the signal as prior information. In conjunction with an iterative reconstruction, this prior information allows to recover missing samples in undersampled k-space. In doing so, the model-parameters are fitted directly to the undersampled data, recovering the missing samples and resulting in quantitative maps.

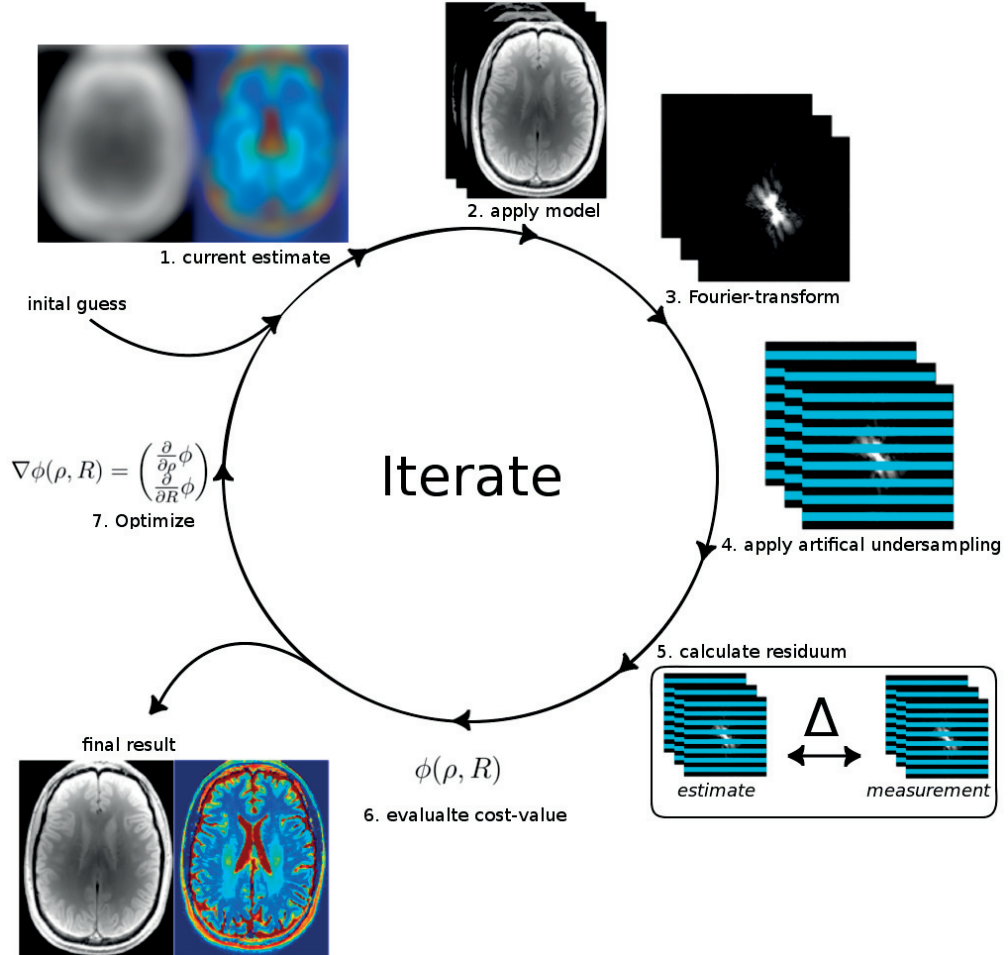


Figure 2.20: An illustration of model-based reconstruction for quantitative T2 mapping.

Various methods were proposed for different sequences with their respective signal-model

[14, 17, 33, 34, 35]. In the following, a model-based reconstruction is explained on the example of quantitative T_2 mapping with a CPMG sequence that corresponds to the signal-model of a mono-exponential decay (see equation 2.5).

As illustrated in Figure 2.20 the reconstruction is started by calculating an initial guess of the M_0 image and the T_2 map by standard fitting of the undersampled data. Subsequently, the forward signal model is applied to calculate simulated image data for all scanned TE times, i.e. a set of estimated T_2 -weighted contrast images.

These images are Fourier-transformed. In order to compare only k-space points which were actually sampled, the resulting estimated k-spaces are multiplied by a binary mask representing the employed block-sampling scheme (“artificial subsampling”). Subsequently, the difference between the actually measured data and the estimated k-space data are calculated. The l2-norm of this residual k-space yields a cost value.

Having this cost value, the algorithm checks whether the error between its estimation and the measured data meets a fixed termination criterion. If the criterion is not met, the iterative reconstruction tries to improve the M_0 and T_2 estimations. To this end, a CG descent optimizer is used, which needs the derivative maps for all fitted parameters. This process is repeated until one of two stop criteria is fulfilled: either an error threshold is reached or the maximal number of iterations.

2.6.5 Simultaneous Multi Slice

With simultaneous-multi-slice (SMS), data of several slices can be measured at the same time rather than sequentially. This approach facilitates promising acceleration factors in 2D MRI, because usually many different slices need to be acquired, for example to cover the whole brain. To that end, the conventional acquisition and reconstruction needs to be modified.

First, In order to acquire multiple slices simultaneously, the standard RF pulse of the measurement needs to be adapted to excite multiple slices at the same time. This is achieved by multiplexing the excitation-RF pulses of individual slices, yielding a multi-band RF-pulse which enables simultaneous acquisition of slices [36]. However, this approach increases the power deposition dramatically such that the SAR limits are easily exceeded, which is a major limitation of multi-band

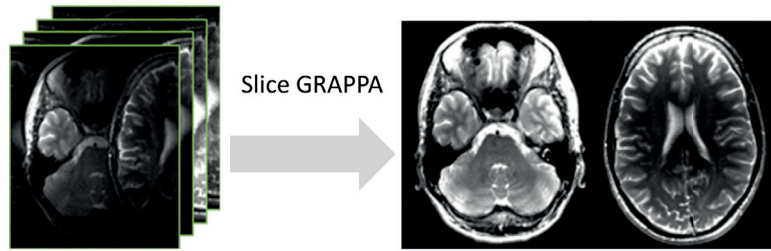


Figure 2.21: Example for the simultaneous acquisition of two slices with the overlaying slices for each coil-element (left) and the with Slice-GRAPPA (SG) separated coil-combined slices (right).

acquisitions. Power independent of Number of Slices (PINS) RF-pulses addresses this problem and is a method to excite multiple slices with low-power by multiplying existing RF pulses with a Dirac comb function. This multiplication is similar to undersampling and thus causes aliasing along the slice direction. Therefore, a comb of slices is excited without increasing the power deposition [37].

Second, when applying a direct inverse Fourier transform on data of simultaneously acquired imaging slices, all slices will be aliased within the resulting image. Therefore, the reconstruction needs to separate the data of each single slice prior to the standard reconstruction. Split-slice-GRAPPA (SG) [38] is one method to perform such a separation. It uses the prior-knowledge of linear dependencies between multiple receiver coils, similar to the parallel-imaging technique GRAPPA (see also section 2.6.2). First, these linear dependencies need to be trained on calibration data; rapidly acquired, low resolution images with single-slice excitation pulses. After the separation of the data, the k-space is reconstructed in a standard fashion, e.g. using a direct Fourier transform and sum-of-square coil combination.

More recently, controlled aliasing SMS was introduced, proposing to shift the signal from different simultaneously excited slices relative to each other, rendering their separation significantly more robust. The slice shifts can be introduced by varying the RF phases [39] or by applying short gradient blip pulses [40].

3 Accelerated T_2 Mapping Combining Parallel MRI and Model-Based Reconstruction

The content of the following Chapter is based on the draft of the article: “Accelerated T_2 Mapping Combining Parallel MRI and Model-Based Reconstruction - GRAPPATINI” with planned submission to the Journal of Magnetic Resonance Imaging (JMIR). The manuscript was co-authored by Tilman J. Sumpf, Elisabeth Weiland, Jens Frahm, Jean-Philippe Thiran, Reto Meuli, Tobias Kober and Gunnar Krueger. All co-authors contributed to the idea and reviewed the manuscript.

Abstract: The purpose of this chapter is to accelerate T_2 quantification and simultaneously generate synthetic T_2 -weighted (T_2 -w) image contrast for clinical research and routine. A recently developed model-based approach for rapid T_2 and M_0 quantification (MARTINI), which is based on undersampled k-space data, was extended by parallel imaging (GRAPPA) to enable high-resolution T_2 mapping with simultaneous access to T_2 -w images within less than 2 min for the entire brain. The accuracy and reproducibility of the accelerated T_2 quantification was assessed. Validations comprised MRI studies of an experimental phantom and the brain, knee, prostate and liver from healthy volunteers. Synthetic T_2 -w images were generated from computed T_2 and M_0 maps and compared to conventional fast spin-echo (SE) images. The experimental results demonstrate that GRAPPATINI with up to 10-fold accelerated acquisitions provides T_2 maps and synthetic T_2 -w images consistent with reconstructions of full k-space CPMG-type acquisitions. Synthetic T_2 -w contrasts from various body regions closely resemble conventional fast SE images. In conclusion, GRAPPATINI provides highly reproducible and fast whole-brain T_2 maps and arbitrary synthetic T_2 -w images in clinically compatible acquisition times of less than 2 min. These abilities are expected to support more widespread clinical applications of quantitative T_2 mapping.

3.1 Introduction

Quantitative mapping promises to improve both clinical and neuroscientific applications of MRI [41]. Extending the widespread clinical use of T_2 -w MRI, quantitative T_2 measurements are expected to facilitate the diagnosis of clinically relevant pathologies such as seen in neurodegenerative, inflammatory, or cartilage diseases [42]. The classical approach to T_2

Chapter 3. Accelerated T_2 Mapping Combining Parallel MRI and Model-Based Reconstruction

mapping is a CPMG sequence [43]. As discussed in section 2.5.1 " T_2 Mapping", such an acquisition becomes very long – for example, T_2 mapping of the whole brain at 1 mm in-plane resolution may require more than 15 min. Besides open issues in cross-platform capabilities and reproducibility, such long scan times are an obstacle for an initial clinical exploration.

A prominent method for accelerating such acquisitions is undersampling k-space with respect to the Nyquist-Shannon theorem and using prior knowledge to recover the non-sampled data. A widely established undersampling technique is parallel imaging, coarsely divided into k-space-based methods (e.g. Generalized autocalibrating partially parallel acquisition = GRAPPA) [26] and image-based methods (e.g. Sensitivity Encoding = SENSE) [27] as described in more detail in section 2.6.2 "Parallel Imaging".

Another category of accelerated parametric mapping techniques are model-based reconstructions, which incorporate physical or physiological signal models as prior knowledge in an iterative reconstruction which is described in section 2.6.4 "Model-Based Reconstruction". A technique of particular interest to this work is termed "Model-based Accelerated Relaxometry by Iterative Non-linear Inversion" (MARTINI) [14]. Assuming a mono-exponential T_2 decay, MARTINI recovers missing samples by estimating T_2 maps directly on undersampled k-space data. Notably, MARTINI ignores the first spin echo (SE) to mitigate T_2 overestimation due to stimulated echoes.

The multitude of acceleration methods and their respective advantages and limitations give rise to the question to what extent they are orthogonal and whether some of these techniques can be advantageously combined. This work follows this idea by combining GRAPPA with MARTINI in order to exploit prior knowledge from both local k-space dependencies and the signal model of a CPMG sequence. The clinical motivation for this combination is to establish a 2D whole-brain T_2 mapping protocol at reasonable resolution and within an acquisition time of < 2 min that achieves similar reproducibility and image quality as the previously reported 5-fold accelerated MARTINI acquisition. Furthermore, such protocol also allows for the simultaneous generation of synthetic T_2 -w images with contrasts comparable to conventional fast SE acquisitions.

3.2 Materials and Methods

All acquisitions were performed at 3 T (Magnetom Skyra and Trio, Siemens, Germany) using a commercially available 20-channel, 32-channel and 64-channel head coil, 15-channel knee coil and 64-channel body coil. Prior to scanning, informed written consent was obtained from each volunteer.

3.2.1 Acquisition

For T_2 mapping with MARTINI, a CPMG sequence with a block-sampling pattern was suggested [14]. This pattern continuously samples segments (blocks) of k-space, shifting the k-space position of sub-sequent sampling blocks in the echo dimension by one block width. The block width is defined by the number of phase-encoding steps divided by the MARTINI acceleration factor (AF). An exemplary block-sampling is shown in Figure 3.1a. In the following, we will refer to the sequence using this undersampling pattern as the “MARTINI sequence”.

Here, we suggest achieving an even higher reduction in scan time by further undersampling the blocks. To that end, a classic parallel imaging scheme with two-fold acceleration is used, i.e. only every other (phase-encoding) line is acquired. Since the first echo is not used in the MARTINI reconstruction, the reference lines necessary

for GRAPPA are obtained by filling a central part of k-space with the first spin echo of each phase-encoding step. Therefore, in this implementation, no additional scan time is required to acquire a calibration dataset for the GRAPPA reconstruction. An exemplary GRAPPATINI sampling scheme is shown in Figure 3.1b (reference lines marked in green). In the following, we will refer to the sequence using this undersampling pattern as the “GRAPPATINI sequence”.

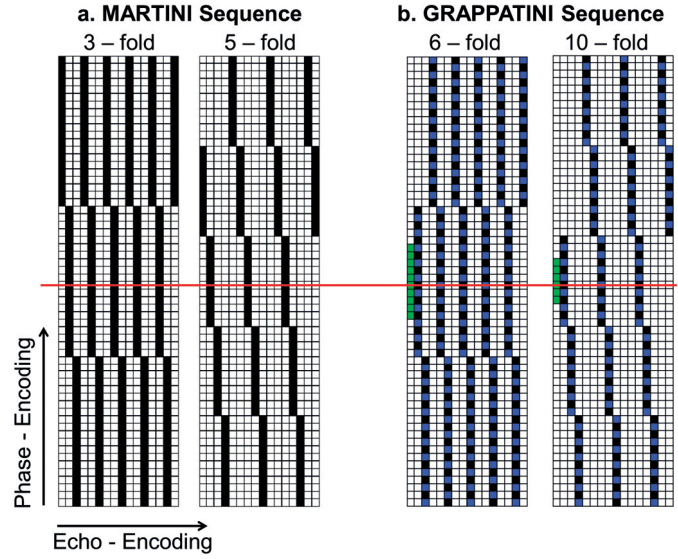


Figure 3.1: (1a) MARTINI sampling pattern and (1b) the proposed GRAPPATINI sampling pattern with black squares indicating sampled and white squares non-sampled data for an exemplary image matrix with 60 phase encoding lines and 16 echoes. The readout dimension is orthogonal to the shown k-space plain. The red line indicates the k-space centre with zero phase-encoding. The green samples in the GRAPPATINI pattern indicate the sampled first echo lines used for GRAPPA calibration. The blue squares indicate non-sampled k-space lines that are reconstructed using GRAPPA only.

Chapter 3. Accelerated T_2 Mapping Combining Parallel MRI and Model-Based Reconstruction

3.2.2 Reconstruction

First, a 3x3 GRAPPA kernel was calculated from the central k-space data, sampled with the first echo (green in Figure 3.1b). This is accomplished by linear fitting weights that describe the dependency of the calibration data to their corresponding neighbouring samples as described in literature [26]. The subsequent GRAPPA reconstruction uses this kernel to recover the missing lines (blue in Figure 3.1b) within all sampling blocks. The resulting blocks are continuous and thus constitute a standard MARTINI dataset as illustrated in Figure 3.1a. Lastly, the MARTINI reconstruction was employed to obtain T_2 and M_0 maps based on the block-sampled data by minimizing a cost function as described previously [14]:

$$M_0, T_2 = \arg \min_{M_0, T_2} \frac{1}{2} \sum_{c=0}^N \sum_{t \in TE} \left\| PF \left\{ S_c M_0 \exp \left(-\frac{t}{T_2} \right) \right\} - Y_{t,c} \right\|_2^2, \quad (3.1)$$

where TE is the vector of echo times, P a binary mask representing the sampling pattern, F the discrete Fourier transform operator, M_0 the equilibrium magnetization, $Y_{t,c}$ the actually acquired k-space data from coil element c at echo time t , N the number of receiver coils, and S_c the complex coil sensitivities. The coil sensitivities were computed using the NLINV algorithm [44] modified to estimate the global image phase. Notably, algorithms such as ESPIRiT [45] cannot be used since they calculate the relative phase between coils only, which would require estimating the global image phase in the model as well. Subsequent to the computation of T_2 and M_0 maps, synthetic T_2 -w images with arbitrary TE values can be generated using the forward signal model (i.e. a mono-exponential decay) for comparison with clinical routine T_2 -w image contrasts.

3.2.3 Artificial Undersampling for Ground-Truth Comparison

Fully sampled k-space data of phantom and in vivo experiments were retrospectively undersampled by zeroing the respective k-space samples to mimic MARTINI and GRAPPATINI experiments. This artificial undersampling enables comparison to the ground truth as calculated from the fully sampled data.

A multi-purpose phantom (five compartments with different concentrations of $MnCl_2 \cdot 4H_2O$, Siemens E-38-19-195-K2130) was used to assess the performance of the methods. For that purpose, k-space was fully sampled with a standard 2D CPMG sequence and protocol parameters as shown in Table 3.1. Reference T_2 values from the phantom were obtained by performing a mono-exponential fit on multiple single-echo SE acquisitions.

In addition, three healthy volunteers were scanned using the same sequence parameters. The phantom and volunteer studies were retrospectively undersampled and reconstructed according to both MARTINI (5- and 10-fold) and GRAPPATINI (10-fold) sampling schemes. Prior work [14] and experience-based qualitative radiological assessment let us choose a 5-fold MARTINI whole-brain protocol as a benchmark. This benchmark protocol was found to repre-

	Brain			Knee			Prostate			Liver	
	a. CPMG	b. GRAPPATINI	c. Fast SE	d. GRAPPATINI	e. Fast SE	f. GRAPPATINI	g. Fast SE	h. GRAPPATINI	i. Fast SE		
TA	17:23 min	3:46 min	2:37 min	6:22 min	2:52 min	4:19 min	5:27 min 3 Averages	2:50 min	2:01 min 2 Averages		
Acceleration	Fully sampled	10-fold	Factor 9, GRAPPA 2	6-fold	Factor 9, GRAPPA 2	10-fold	Factor 11, GRAPPA 2	10-fold	Factor 9, GRAPPA 2		
TR	6520 ms	4000 ms	4000 ms	48800 ms	3790 ms	5290 ms	7500 ms	5849 ms	6474 ms		
TE	9 ms	10.9 ms	77 ms	10 ms	80 ms	10.8 ms	100 ms	8.8 ms	100 ms		
Echoes	17	16	1	10	1	16	1	16	1		
Matrix	160 x 192	512 x 270	512 x 270	260 x 320	260 x 320	320 x 270	320 x 320	400 x 260	448 x 206		
Resolution	1.1 x 1.1 x 3 mm ³	0.4 x 0.8 x 3 mm ³	0.4 x 0.8 x 3 mm ³	0.6 x 0.5 x 3 mm ³	0.6 x 0.5 x 3 mm ³	0.6 x 0.6 x 3.5 mm ³	0.6 x 0.6 x 3.5 mm ³	0.8 x 0.8 x 6 mm ³	0.9 x 0.9 x 5 mm ³		
Slices	30	43	43	36	36	20	20	16	16		
Concatenations	1	2	1	2	1	1	1	1	1		

Table 3.1: Sequence parameters of all sequences and experiments employed in this study.

Chapter 3. Accelerated T_2 Mapping Combining Parallel MRI and Model-Based Reconstruction

sent a good compromise between acquisition time and image quality. For evaluation of the reconstruction quality, the resulting T_2 maps were compared to the MARTINI reconstruction of the fully sampled k-space by calculating the root-mean-squared difference (RMSD) and by visual inspection of the relative difference (criteria = contrast and apparent SNR).

3.2.4 Acquisition of Undersampled Data and Reproducibility

In contrast to validations using retrospective undersampling, truly undersampled acquisitions applied a slightly modified gradient pattern, which theoretically may lead to a different artefact pattern than in retrospectively undersampled data, e.g. due to slightly modified eddy currents, differences in motion sensitivity etc. Therefore, one healthy volunteer was scanned with a GRAPPATINI prototype sequence (Table 3.1a, yielding TA = 1:44 min) implementing the sampling pattern as illustrated in Figure 3.1b, a MARTINI sequence (TA = 3:27 min) and a fully sampled CPMG sequence (TA = 17:23 min) with the same parameters.

For initial exploration of the reproducibility of the proposed sequence, the same GRAPPATINI sequence (with TA = 1:44 min) was used to scan and rescan five additional healthy volunteers without repositioning. Regions of interest (ROIs) were manually drawn within the white matter (WM) of the frontal lobe and the Globus Pallidus in order to calculate the intra-subject scan-rescan standard deviation (SD) and the inter-subject SD between subjects within these ROIs.

In order to demonstrate the potential for a more widespread use of GRAPPATINI in clinically feasible acquisition times, high-resolution T_2 maps from the brain, knee, prostate and liver were acquired in healthy volunteers. Synthetic T_2 -w image contrasts were generated and visually compared to conventional T_2 -w images, acquired at similar resolution using a fast SE sequence (sequence parameters in Table 3.1b-i). All images were calculated on the scanner's image reconstruction computer equipped with a 16-core processor (Intel(R) Xeon(R) CPU E5, 2.1GHz) and 8 GB of RAM yielding reconstruction times of 2 min for the entire slice group depending on the image matrix size.

3.3 Results

3.3.1 Artificial Undersampling for Ground-Truth Comparison

T_2 maps of the phantom experiments and their relative difference to the fully sampled reconstruction are shown in Figure 3.2a. The mean T_2 values in the various compartments (T_2 ranging from 18 to 150 ms) deviated less than 5% for 5-fold MARTINI and 10-fold GRAPPATINI reconstructions, except for the compartment with the shortest T_2 = 18 ms where values deviated 8% on average. The 10-fold MARTINI deviates further especially for compartments with short T_2 values (18 ms with 55 % error, 25 ms with 14% error). The 10-fold GRAPPATINI T_2 map mostly resembled the 5-fold MARTINI reconstruction though at a subtle increase in

noise. These qualitative observations were confirmed by the RMSD (Figure 3.2e). The RMSD of the GRAPPATINI reconstruction is 2.6% higher than the 5-fold MARTINI but well below the RMSD of the 10-fold MARTINI reconstruction (28.7% higher than 5-fold MARTINI), although it requires the same acquisition time. Due to stimulated echo signals, the T_2 values of all CPMG acquisition are usually overestimated in comparison to the single-echo SE acquisition (see Figure 3.3a) as already reported in literature [15]. Together, the phantom experiments revealed an approximate overestimation of 20% for most of the T_2 range except for short T_2 (<20 ms) with an overestimation of 70%.

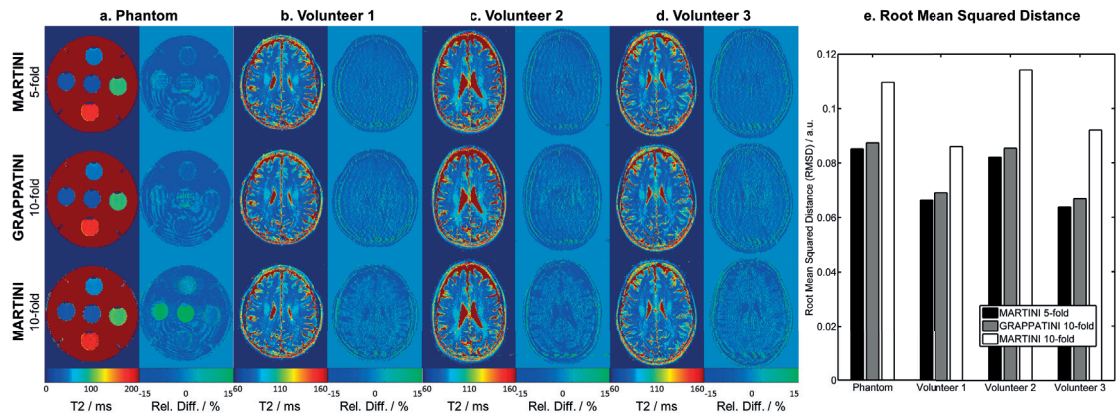


Figure 3.2: T_2 maps and relative difference to ground truth, full k -space acquisition for a (2a) multi-purpose phantom, (2b-d) in vivo experiments using MARTINI (acceleration 5 and 10) and GRAPPATINI (acceleration 10) based on retrospective undersampling of fully sampled data. (2e) The root mean squared distance (RMSD) of the reconstructed data to the fully sampled data from all experiments in comparison.

Phantom results were confirmed by retrospectively undersampled in vivo data of three healthy volunteers. Figure 3.2b-d shows the reconstructed T_2 maps and relative difference. Similarly, aliasing artifacts are observed to increase when going from 5-fold to 10-fold accelerated MARTINI, whereas a comparison of 5-fold MARTINI to 10-fold GRAPPATINI reveals a marginal increase in noise (average 30.4% increase in SD within WM ROI across subjects) in the centre of the brain. In general, the observed artifacts of the GRAPPATINI reconstruction resemble the artifacts of the 5-fold MARTINI reconstruction, although the acquisition time is halved.

Aliasing was observed especially in vessels (e.g. sagittal sinus) where flow signals potentially result in a violation of the T_2 signal model. These artifacts appear less severe in GRAPPATINI when compared to 10-fold MARTINI. The RMSD behaves similarly to what was observed in the phantom experiment: when going from 5-fold to 10-fold MARTINI, the RMSD increased 37.6% on average which is more than using GRAPPATINI (average RMSD increase 4.3%) (see also Figure 3.2e).

Chapter 3. Accelerated T_2 Mapping Combining Parallel MRI and Model-Based Reconstruction

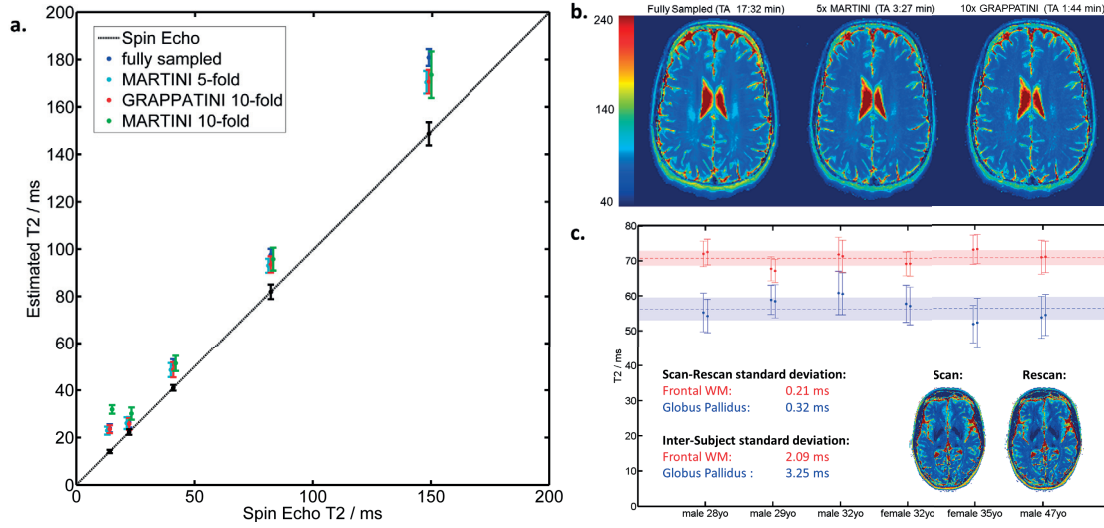


Figure 3.3: (a) Mean T_2 and its standard deviation of all reconstructions in comparison to the values obtained with a single-echo SE sequence. (b) T_2 maps for comparison calculated based on a fully sampled sequence (TA 17:32 min), a 5-fold undersampled MARTINI sequence (TA 3:27 min) and a 10-fold undersampled GRAPPATINI sequence (TA 1:44 min). (c) Mean T_2 values within regions of interest in the frontal white matter (red) and Globus Pallidus from six healthy subjects that were scanned twice. Error bars indicate the standard deviation within the region of interest and the coloured ranges the standard deviation across subjects.

3.3.2 Acquisition of Undersampled Data and Reproducibility

Additional data of a healthy volunteer which was obtained by truly undersampled GRAPPATINI in comparison to MARTINI and a fully sampled CPMG sequence is shown in Figure 3.3b. Similar to the retrospective undersampling, the 10-fold GRAPPATINI reconstruction resembles the 5-fold MARTINI results except for an increase in noise. Therefore, we conclude that the modified gradient pattern when using a truly undersampled acquisition does not appear to introduce additional artifacts.

For initial assessment of the reproducibility in T_2 measurements, back-to-back scans (no repositioning) with GRAPPATINI were performed in six subjects. The mean T_2 of ROIs in the frontal WM and Globus Pallidus were computed in all subjects (see Figure 3.3c). The mean T_2 values between scan and rescan showed a standard deviation of 0.21 ms in the frontal lobe WM and 0.32 ms for the Globus Pallidus. Furthermore, mean T_2 values between subjects showed a $\approx 10\times$ higher standard deviation of 2.09 ms in the frontal lobe WM and 3.25 ms in the Globus Pallidus. Exploratory high resolution T_2 maps, simulated T_2 -w images, and conventional fast SE images with similar T_2 weighting of brain, knee, prostate and liver applications are shown in Figure 3.4. Simulated contrasts from the brain acquisitions still yield reasonable SNR levels (0.96 μL voxel size) and closely resemble contrasts of the conventional T_2 -w images. In contrast to the brain, T_2 maps of the knee exhibit a higher SNR due to the coil geometry. Prostate T_2 maps show a good contrast between transitional and peripheral zone. Liver T_2

maps, however, exhibit some motion artifacts although the free-breathing sequence was triggered using a navigator at the liver dome.

3.4 Discussion

Phantom and in vivo results demonstrate that the combination of GRAPPA and MARTINI provides T_2 maps very comparable to those from MARTINI in only half the acquisition time ($TA = 1:44$ min for whole-brain studies at 1 mm in-plane). The 10-fold GRAPPATINI appears to provide improved artifact behaviour in comparison to 10-fold MARTINI and usually closely resembles a 5-fold MARTINI reconstruction, except for an increase in noise (30.4% see results) due to the higher degree of undersampling and noise amplification by GRAPPA.

Model-based reconstructions are typically sensitive to signal behaviour that deviates from the model used in the cost function. In the case of T_2 mapping, a mono-exponential decay approximates quite well the signal evolution when excluding the first echo to minimize stimulated echo contributions. However, it is a simplified model that does not take into account effects like blood flow, partial volume, multiple components (e.g. due to myelin), stimulated echoes and motion, among many others. In both MARTINI and GRAPPATINI reconstructions, signal energy that violates the model is distributed as aliasing artefact depending on the undersampling pattern. For that reason, aliasing artifacts become stronger and have lower frequencies with increasing MARTINI acceleration factors, i.e. decreasing width of sampling blocks. GRAPPATINI enables a reduction of the acquisition time while maintaining the k-space block size, maintaining similar residual artifacts of the MARTINI reconstruction while gaining in acquisition time. Inversely, GRAPPATINI could be used to double the block size while maintaining the acquisition time which consequently reduces aliasing artifacts.

MARTINI intrinsically includes a multi-channel image reconstruction by using complex coil sensitivities within its cost function (equation 3.1). The question arises why the 10-fold accelerated SENSE-based reconstruction is outperformed by 5x2-fold accelerated GRAPPATINI, which results in more benign image artifacts in the presence of model violations. It is our understanding that this improved artefact behaviour originates from the fact that GRAPPA recovers k-space lines by only relying on local k-space dependencies as a model. Therefore, the reconstruction is less sensitive to signal violations along the T_2 decay, inaccuracies of the coil-sensitivity maps used in MARTINI, or other potential model violations.

GRAPPATINI, however, introduces additional noise in the resulting T_2 maps. It is well known that the SNR scales with $\frac{1}{g\sqrt{AF}}$ (AF denoting the acceleration factor, g being impacted by coil design) when undersampling an MRI dataset [46]. When not considering any effect of the regularization during reconstruction, a loss of 30% in SNR is expected when adding the additional GRAPPA, which is in line with the experimental observation in this work (see Figure 3.2).

B_1 field inhomogeneity and finite RF pulse durations lead to imprecise refocusing pulses

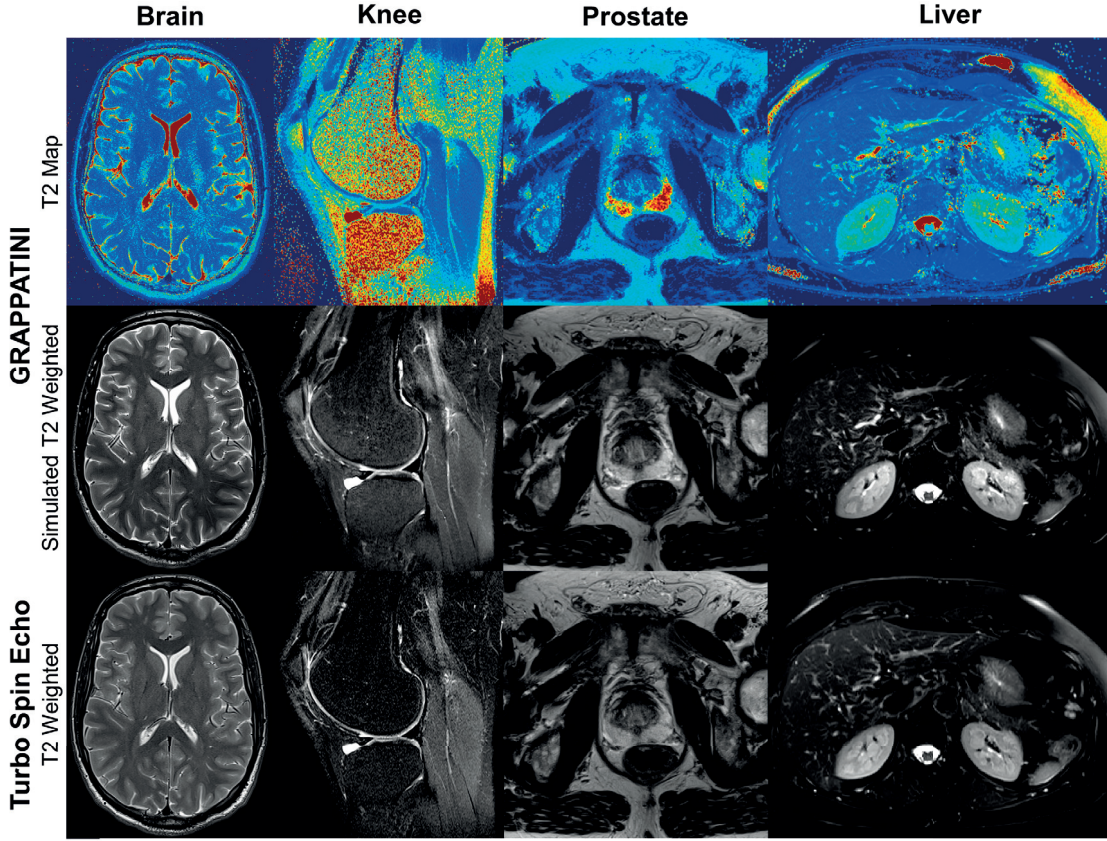


Figure 3.4: T_2 maps and simulated T_2 contrasts of the brain, knee, prostate and liver acquired with the GRAPPATINI sequence. For comparison, T_2 contrasts acquired with a conventional fast SE sequence are shown as well.

which do not imprint a 180° flip angle across the slice profile and represent a fundamental challenge in quantification attempts. The resulting stimulated echoes are a well-known effect in CPMG-based T_2 -mapping techniques; they mix longitudinal magnetization (i.e. T_1 -governed components) into the measured signal. Subsequent mono-exponential fitting of this signal will yield overestimated T_2 values, especially if the first echo is not discarded. Phantom experiments in this work revealed a $\approx 20\%$ overestimation for this particular set of sequence parameters and even higher overestimation for short T_2 values (< 20 ms). Despite the high overestimation, which represents a bias to an accurate T_2 quantification, the measured T_2 values were reproducible for both intra- (< 0.4 ms SD) and inter- (< 4 ms SD) subject within the same scanner platform. Depending on study type (longitudinal or cross-sectional) such variability will allow to detect pathological abnormalities of this magnitude. As an alternative solution for coping with stimulated echoes, signal models were proposed by either using Bloch simulations [18] or direct analytical solutions [16, 17], resulting in more accurate but not necessarily more reproducible T_2 estimation. A model-based approach that also addresses stimulated echoes is proposed in [17].

In comparison to MR fingerprinting [23, 47], the proposed method provides a single tissue parameter and generates synthetic T_2 -w images, whereas MR fingerprinting estimates multiple parameters simultaneously (e.g. T_1 and T_2). In terms of limitations as mentioned above (such as blood flow, partial volume, multiple components (e.g. due to myelin), stimulated echoes, magnetization transfer effects, motion and others), both methodologies are susceptible to respective violations. Further investigations may explore the sensitivities of each approach to the individual sources of image artifacts and will be addressed in Chapter 5.

The synthetic T_2 -w images showed similar contrast and noise in comparison to conventional fast SE images. Observed contrast differences in the absence of artifacts may arise from discarding the first echo in the GRAPPATINI reconstruction, whereas this echo usually contributes to fast SE MRI. Furthermore, the synthetic T_2 -w images have the advantage that no k-space data from different echoes is mixed and thus avoids T_2 blurring as present in fast SE sequences, occurs. Furthermore, the TE of the image can be changed retrospectively. Therefore, in the absence of other artifacts such as motion, a single GRAPPATINI acquisition may even lead to a more representative characterization of the object and potentially replace multiple fast SE acquisitions with different T_2 -weighting, gaining total acquisition time. For example, knee acquisitions, where typically three different contrasts (proton density as well as intermediate and strong T_2 -weighting) are acquired, could be optimized by using a single GRAPPATINI acquisition.

In conclusion, this work demonstrates the feasibility of combining model-based MARTINI reconstruction with GRAPPA parallel imaging to further accelerate T_2 mapping with simultaneous access to synthetic T_2 contrasts. The results reveal a more robust reconstruction of parametric maps with less aliasing artifacts in comparison to a conventional MARTINI reconstruction at the same acceleration. Although the additional undersampling by GRAPPA slightly decreases SNR, a two-fold time gain is expected to offer an acceptable compromise for a wide variety of clinical applications. GRAPPATINI allows for a determination of quantitative T_2 maps in clinically feasible acquisition and reconstruction times, which opens up the proposed method to an extensive clinical exploration. Lastly, initial assessments of the scan-rescan reproducibility of quantitative T_2 measurements in selected brain ROI are promising, as the intra-subject scan-rescan deviations appear $\approx 10\times$ smaller compared to the inter-subject differences that are dominated by the biological origin of tissue properties.

4 Fast Model-Based T_2 Mapping using SAR-Reduced Simultaneous-Multi-Slice Excitation

The content of the following Chapter is based on the draft of the article: “Fast Model-based T_2 Mapping using SAR-Reduced Simultaneous-Multi-Slice Excitation” with planned submission to Magnetic Resonance in Medicine (MRM). The manuscript was co-authored by Jennifer Schulz, Lauren J. Bains, José P. Marques, Reto Meuli, Jean-Philippe Thiran, Gunnar Krueger, David G. Norris and Tobias Kober. All co-authors contributed to the idea and Tobias Kober reviewed the manuscript.

Abstract: The purpose of this chapter is to obtain high-resolution T_2 maps from the whole brain in two minutes by combining low-power simultaneous multi-slice excitation pulses with an adapted undersampling pattern and a model-based reconstruction. A multi-echo spin-echo sequence was modified to acquire multiple slices simultaneously using power independent N-Slices (PINS) pulses, ensuring low specific absorption rate requirements. In addition, the acquisition was undersampled to achieve further acceleration. Data was reconstructed by subsequently applying parallel imaging to separate signals from different slices, and a model-based reconstruction to estimate quantitative T_2 from the undersampled data in each slice. The employed signal model is based on extended phase graph simulations that also account for non-ideal slice profiles and B_1 inhomogeneity. In-vivo experiments with three healthy subjects were performed to compare accelerated T_2 maps to fully sampled single slice acquisitions. T_2 values were compared using manually drawn regions of interest in the white matter of the frontal lobe and the Globus pallidus. The accuracy of the T_2 values was assessed with phantom experiments by comparing the T_2 values to single-echo spin echo measurements. In-vivo results showed that conventional multi-echo spin-echo, simultaneous multi-slice and undersampling results in similar mean T_2 values within regions of interest when using the proposed reconstruction technique. However, both SMS and undersampling results in higher standard deviations (≈ 6 ms) in comparison to a conventional sequence (3 ms). The T_2 values were reproducible between scan and rescan within subjects and were in similar ranges across subjects. Phantom experiments were used to demonstrate that the model-based reconstruction accurately estimates T_2 and is able to account for non-ideal slice profiles and B_1 -field inhomogeneity. The proposed method is a fast T_2 mapping technique that

Chapter 4. Fast Model-Based T_2 Mapping using SAR-Reduced Simultaneous-Multi-Slice Excitation

enables robust whole brain acquisitions at 0.7 in-plane resolution and 3 mm slice thickness in 2 minutes.

4.1 Introduction

The previous Chapter achieved highly accelerated acquisitions for quantitative T_2 maps by combining parallel imaging and model-based reconstruction. The question arises if there may be other acceleration techniques that can be combined similarly, achieving even more acceleration. For example, another approach to accelerate 2D MRI sequences is to simultaneously acquire multiple slices (simultaneous multi-slice, SMS) instead of only one, as discussed in section 2.6.5. The superimposed signals from the different slices are disentangled using methods similar to parallel imaging, i.e. by exploiting the varying spatial sensitivities in multiple receiver coils. SMS excitation pulses are created by multiplexing sinc pulses, resulting in a larger power deposition and hence restrictions due to specific absorption rate (SAR) safety constraints. This is especially the case for multiplexed refocusing pulses, as used in T_2 mapping CPMG sequences; safety limits are easily reached which render the application of SMS refocusing for these types of sequences almost impossible. This problem was addressed by Power independent N-Slices (PINS) pulses. The crucial difference of PINS to traditional SMS pulses is that their power deposition is approximately only two times larger than that of one single sinc pulse, over-coming the SAR-induced limits for SMS, especially at 3T.

Stimulated echoes are always present in a CPMG sequences due to B_1 inhomogeneity and non-ideal (i.e. not rectangular) slice profiles (see more detail in section 2.5.1). If a mono-exponential decay is fitted over the different echoes, the resulting T_2 value will be overestimated as it is the case in the previous Chapter 3, where T_2 estimates are reproducible, but systematically biased.

Shorter acquisition times are crucial for adoption of qMRI in the clinical practice. This chapter addresses this problem by combining different acceleration approaches while accounting for systematic biases in the T_2 measurements in order to obtain accurate and reproducible, high-resolution T_2 maps of the whole brain in two minutes. To this end, we combine simultaneous slice excitation using PINS pulses with an undersampled acquisition scheme and a subsequent model-based reconstruction accounting for stimulated echoes.

4.2 Materials and Methods

4.2.1 Acquisition

A standard CPMG sequence was modified in order to excite and receive the signal from multiple slices simultaneously. To that end, the standard excitation pulse was replaced by a multi-band (MB) pulse (i.e. multiple multiplexed slice selective pulses); the refocusing pulses were replaced by PINS pulses. Due to the principle of PINS pulses to use aliasing in slice direction to excite multiple slices, their pattern spreads indefinitely, which might affect

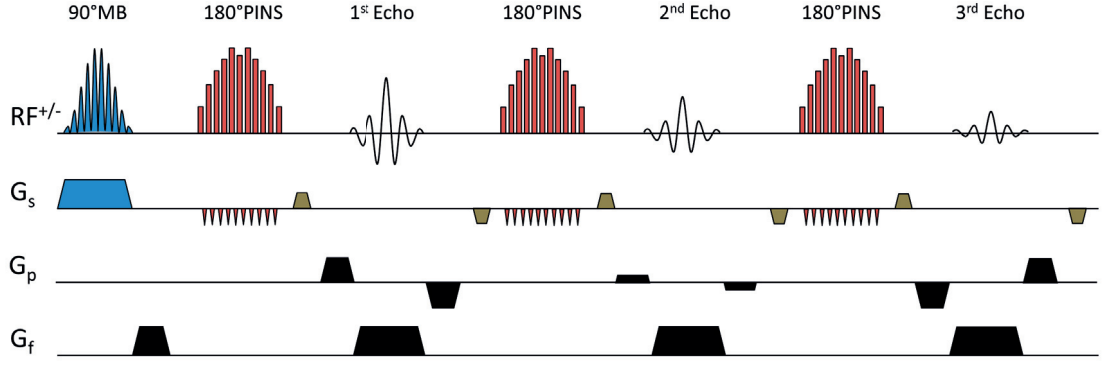


Figure 4.1: CPMG sequence diagram with transmit and receive radio-frequency (RF+/-), slice-, phase- and frequency-encoding gradients (G_s, G_p, G_f). Excitation is performed with a multiband-pulse (blue) and refocusing with PINS pulses (red). Additionally, gradient blips (green) were added for controlled aliasing of slices along the phase-encoding direction.

areas of the body which are not in the intended FOV. Therefore, initial usage was restricted to sagittal slices (moving the aliasing into R-L direction). Due to the use of a classical MB pulse for excitation and PINS pulses only for refocusing, the full flexibility in slice positioning is ensured while the advantageous SAR characteristics of the PINS pulses are exploited, bearing in mind that the main SAR deposition in a CPMG acquisition is due to the repeated refocusing. Lastly, gradient blips were added to the sequence to achieve controlled aliasing along the phase encoding direction, depending on the slice location as previously described in literature [40]. The corresponding sequence diagram is shown in Figure 4.1.

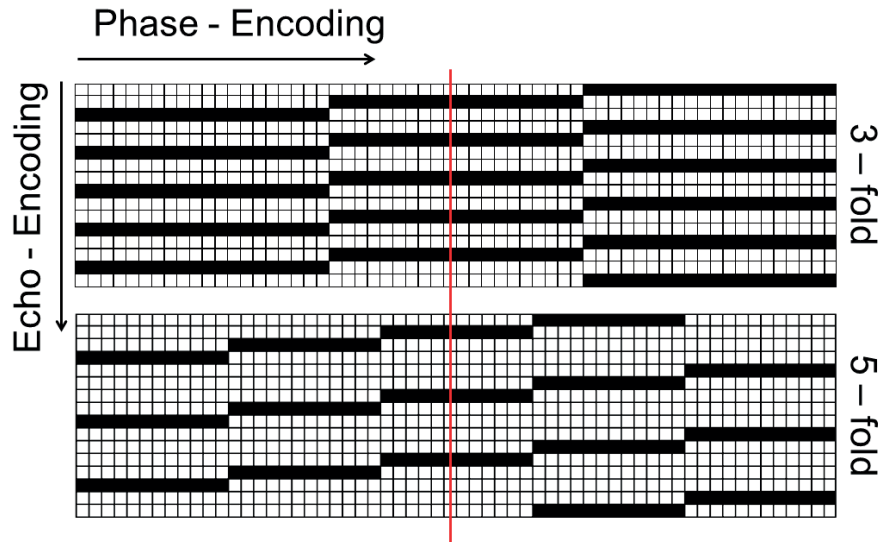


Figure 4.2: Example undersampling patterns for 3-fold and 5-fold acceleration. White samples are skipped during acquisition and black squares indicate sampled k -space points. The red line marks the k -space centre, thus samples with zero phase encoding.

Chapter 4. Fast Model-Based T_2 Mapping using SAR-Reduced Simultaneous-Multi-Slice Excitation

Furthermore, the sequence was undersampled using a block-sampling scheme as originally suggested in [14], i.e. only a segment (block) of k-space is sampled in each echo, whereas the blocks are shifted along the phase-encoding direction between echoes. Example sampling patterns for 60 phase-encoding steps and acceleration factors of three and five are shown in Figure 4.2. To ensure an equal distribution of sampling blocks within k-space, the following heuristic was used: (i) number of phase-encoding lines should be dividable by the undersampling factor and (ii) the undersampling factor itself should be an odd number.

Prior to the modified CPMG sequence, a short spoiled GRE sequence was acquired (matrix size 64x64, TE = 1.91 ms, TR = 228 ms, FOV and slice thickness matched with SMS CPMG sequence), sampling reference lines to train the kernels for the slice-GRAPPA reconstruction.

4.2.2 Reconstruction

All numerical simulations, data analysis and visualizations were performed using MATLAB R2012a (The MathWorks Inc., Natick MA, USA).

Data was reconstructed by subsequently applying a split-slice-GRAPPA and a model-based iterative algorithm. First, GRAPPA kernels were trained on the external gradient echo data. In order to have fully sampled k-spaces, data from adjacent echoes were collapsed, i.e. assuming three-fold acceleration, undersampled data from three consecutive echoes were combined to form one fully sampled k-space, similar to multi-echo RARE images [24]. The split-slice GRAPPA algorithm was then applied on the multiple of full k-space datasets as previously reported [38]. Fully sampled RARE-type k-space datasets for each slice were thus obtained. Subsequently, the data for each slice was de-collapsed to yield the same block-wise undersampled data structure as before, yet now for each slice. An illustration of the reconstruction pipeline and how data was collapsed is shown in Figure 4.3a.

At this point, the k-space data resembles a single-slice, block-undersampled dataset and any model-based reconstruction algorithm that can handle this sampling could be used to estimate T_2 , e.g. assuming a mono-exponential decay [14] or using a generating function that accounts for stimulated echoes [17]. However, the conjugate gradient algorithms used in these methods estimate T_2 and M_0 directly from k-space data using a single cost function. To achieve a stable convergence for a robust reconstruction of T_2 maps, additional measures have to be introduced, e.g. a gradient scaling to account for differences in the magnitude of T_2 and M_0 values or repeated restarts of the conjugate gradient algorithm. To avoid similar data-dependent measures, we propose a split algorithm similar to [48]. This algorithm will be referred to as “Split Algorithm for Fast T_2 mapping”, short SAFT.

SAFT, as illustrated in Figure 4.3b, splits the optimization problem in multiple sub-problems resulting in a three step algorithm: Step A is optimizing the correspondence to the acquired data (data consistency), step B is optimizing the correspondence to the signal model (model consistency), and Step C employs spatial regularization for a more robust reconstruction.

These steps are repeated iteratively to estimate the free variables of the model (T_2 , B_1 and M_0) and are explained in more detail in the following sections.

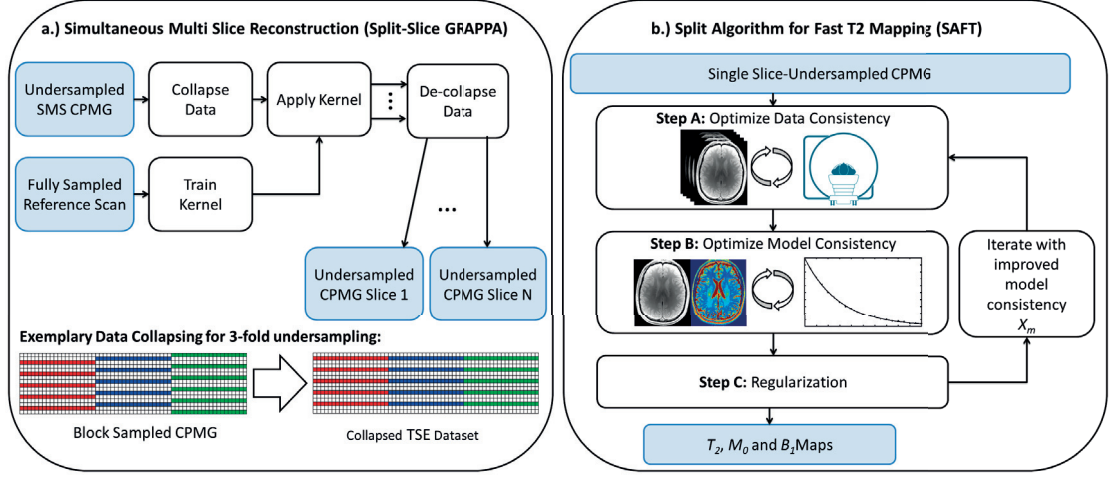


Figure 4.3: a.) The application of split-slice GRAPPA on the undersampled k -space data to separate the signal from different slices. Prior to the application of the kernel, the data sampling blocks (red, blue and green) from multiple echoes are collapsed to yield full k -space data. b.) Illustration of the model-based reconstruction that estimates T_2 , M_0 and B_1 maps by iteratively improving data consistency, model consistency and regularization.

Step A: Data Consistency

The data consistency cost term models the imaging process including undersampling, Fourier transformation and coil combination and is very similar to a typical cg-SENSE reconstruction with an additional term enforcing the signal model onto the data. The images X at each echo-time TE is estimated by minimizing the difference to the k -space data Y as follows:

$$X = \underset{X}{\operatorname{argmin}} \frac{1}{2} \sum_{t \in TE} \left(\sum_{c=0}^N \|PF\{S_c X(t)\} - Y_{t,c}\|_2^2 + \alpha \|X(t) - X_m(t)\|_2^2 \right), \quad (4.1)$$

where S are the complex coil-sensitivities, N the number of coils, F the Fourier transform operator, and P the sampling mask. The weight α enforces similarity to CPMG images X_m which are consistent with the signal model, i.e. images synthesised from the latest T_2 , B_1 and M_0 estimates (see step B). Since X_m is calculated in the next step and is yet unknown, the similarity weight α is set to zero to avoid any model influence in the first iteration.

Step B: Signal Model Consistency

The model consistency cost term uses the current image estimate X from the data consistency (step A) to obtain the current best fit to the signal model. Theoretically, any signal model

Chapter 4. Fast Model-Based T_2 Mapping using SAR-Reduced Simultaneous-Multi-Slice Excitation

(e.g. analytical stimulated echo, Bloch simulations, mono-exponential decay etc.) and any fitting method (e.g. dictionary, log-linear or least-squares) can be used here. In order to use a numerical signal model, we decided to use the same approach as MR fingerprinting [23, 47], i.e. a dictionary fitting that matches the data to a model calculated using the extended phase graph (EPG) [49] methodology. To that end, the EPG algorithm from Weigel et al. [50] was used to simulate the CPMG signals for a range of T_2 values (5 ms, 6 ms, ... 100 ms, 200 ms ... 4000 ms), and B_1 efficiency factors (0.6, 0.62 ... 1) and a fixed $M_0=1$. Furthermore, different B_1 depositions due to imperfect slice profiles were accounted for by discretizing both the excitation and refocusing slice profiles into 65 bins. After simulating each bin, the signals were summed across the profile and stored in a dictionary together with the respective T_2 and B_1 used during simulation. An example slice profile for the MB excitation and the PINS refocusing are shown in Figure 4.4 together with simulated signals. To perform the fitting, a brute force search was used to find the best match for each voxel in image X with a simulated signal in the dictionary. The better the signal decay in the voxel matches a dictionary entry, the greater is the dot-product between the two signal-vectors. Therefore, the dictionary entry with the highest dot-product is assumed to be the most representative for this voxel. As a result, the parameters that were used to simulate this entry can be attributed to this voxel. During the simulation of the dictionary entry, M_0 is fixed ($M_0=1$). Therefore, before calculating the dot-product, the signals need to be normalized to account for variations in M_0 . Scaling factors are calculated with $s_{sim} = \|v_{sim}\|_2^{-1}$ for the signal in the dictionary entry and $s_{acq} = \|v_{acq}\|_2^{-1}$ for the acquired signal in the voxel, where v_{sim} and v_{acq} denote the discrete signal decays respectively. The equilibrium magnetization is then estimated using these scaling factors following $M_0 = s_{sim}/s_{acq}$.

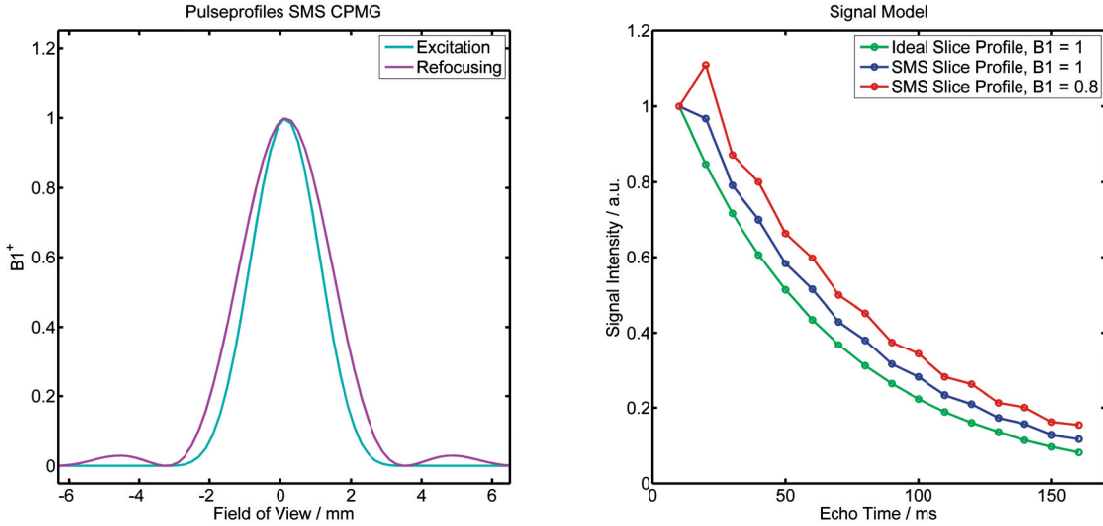


Figure 4.4: (left) Example slice-profiles of the multi-band excitation (cyan) and PINS refocusing (purple) for 3 mm slice thickness. (right) Signals simulated with the extended phase graph (EPG) formalism for a CPMG sequence with $\Delta TE = 10$ ms and 16 echoes and tissue properties $T_2 = 60$ ms and $T_1 = 800$ ms with a rectangular slice-profile (green) and the SMS slice profile without (blue) and with transmit field inhomogeneity (red).

The entire process of step B is comparable to maximizing the dot-product between the CPMG images X and the simulated signals of the EPG sequence depending on T_2 , M_0 and B_1 :

$$\begin{pmatrix} T_2 \\ M_0 \\ B_1 \end{pmatrix} = \arg \max_{T_2, M_0, B_1} X \cdot M_0 EPG(T_2, B_1). \quad (4.2)$$

Step C: Spatial Regularization

In a last step, prior knowledge on the characteristics of the T_2 and B_1 maps is exploited to regularize the results obtained in the signal model consistency step (step B). B_1 biases manifest themselves as smooth variations across the FOV. This is imposed on the obtained B_1 map by convoluting it with a 2D Gaussian kernel G :

$$B'_1 = B_1 * G(\sigma). \quad (4.3)$$

where σ is the standard deviation of the kernel. Furthermore, we assume the T_2 map to be sparse in the Wavelet domain. Subsequent application of a Wavelet transform Ψ , a soft-threshold T with the strength λ , and the inverse wavelet transform imposes this regularization:

$$T'_2 = \Psi^{-1} T(\Psi T_2, \lambda). \quad (4.4)$$

Subsequently, the regularized parameter maps T'_2, B'_1 together with M_0 (from step B) are used in the forward EPG signal model to calculate CPMG images for all echo times $X_m(t)$ based on the current (T'_2, B'_1, M_0) estimates:

$$X_m = M_0 EPG(T'_2, B'_1). \quad (4.5)$$

The intensities of X_m are model consistent, since they were calculated using the numerical signal model (EPG simulation).

Iterative Loop and Convergence

Subsequently, a new iteration is started feeding the CPMG images X_m , which were calculated based on the current estimate of T_2 , B_1 and M_0 into the data consistency term (equation 4.1) in step A. Notably, the similarity weighting α is set to a value greater than zero after the first iteration. The process of alternatively calculating step A, B and C is then repeated until a maximum number of 15 iterations is reached. For all reconstructions, a manually tuned Gaussian kernel ($\sigma=3$ mm), wavelet soft-threshold ($\lambda=10$ ms) and similarity weight ($\alpha=1$) were used.

Chapter 4. Fast Model-Based T_2 Mapping using SAR-Reduced Simultaneous-Multi-Slice Excitation

4.2.3 In Vivo Studies

All measurements and calibrations were performed on a clinical 3T whole-body system (MAGNETOM Skyra, Siemens Healthcare GmbH, Erlangen, Germany) with actively shielded magnetic field gradient coils using a commercially available 64-channel head/neck coil. Prior to scanning, informed written consent was obtained from all volunteers.

Data from three healthy volunteers were acquired using the proposed undersampled CPMG-PINS sequence (Figure 4.1) with a slice acceleration factor of five (i.e. five slices are acquired simultaneously) and three different undersampling factors: $R=1$ (i.e. fully sampled), $R=3$ and $R=5$. Relevant sequence parameters were: $TR=3s$, 16 echoes with $\Delta TE=10$ ms, matrix size 320×210 , FOV 220×192 mm², 50 slices, 3 mm slice thickness with 0.3 mm slice gap. The acquisition times for the different combinations of acceleration factors resulted in 10:30 min for 5-fold (5x1) acceleration, 3:30 min for 15-fold (5x3) and 2:06 min for 25-fold (5x5) acceleration. The measurement of the low-resolution GRE sequence (matrix size 64×64 , FOV 220×192) required to calculate kernels for the split-slice-GRAPPA reconstruction added another 14 s acquisition time. To study the reproducibility of the T_2 values, the 25-fold (5x5) accelerated acquisition was repeated without repositioning the volunteer in order to evaluate the scan-rescan variability of the obtained T_2 values in manually drawn regions of interest (ROI).

For comparison, a fully sampled standard single-slice excitation CPMG sequence was acquired using the same sequence parameters, except for the number of slices, which had to be set to ten to keep the same repetition time as in the prototype sequence. The acquisition time for this 10-slices comparison scan was 10:30 min. In theory, comparable slice coverage would result in a scan time of 52:30 min (5 x 10:30 min) using the standard sequence. ROIs were manually drawn in the white matter (WM) of the frontal lobe and the Globus Pallidus (GP) to compare T_2 values.

4.2.4 Phantom Studies

Phantom experiments were performed to quantitatively validate the T_2 values estimated with the proposed method. To that end, a multi-purpose phantom (five compartments with different concentrations of $MnCl_2 \cdot 4H_2O$, Siemens E-38-19-195-K2130) was scanned using the same protocols as in the in-vivo studies. Additionally, multiple single-echo spin-echo acquisitions with different TE's (10 ms, 15 ms, 20 ms, 40 ms, 80 ms, 150 ms) were performed in order to estimate the ground truth T_2 values within the compartments using a non-linear fit.

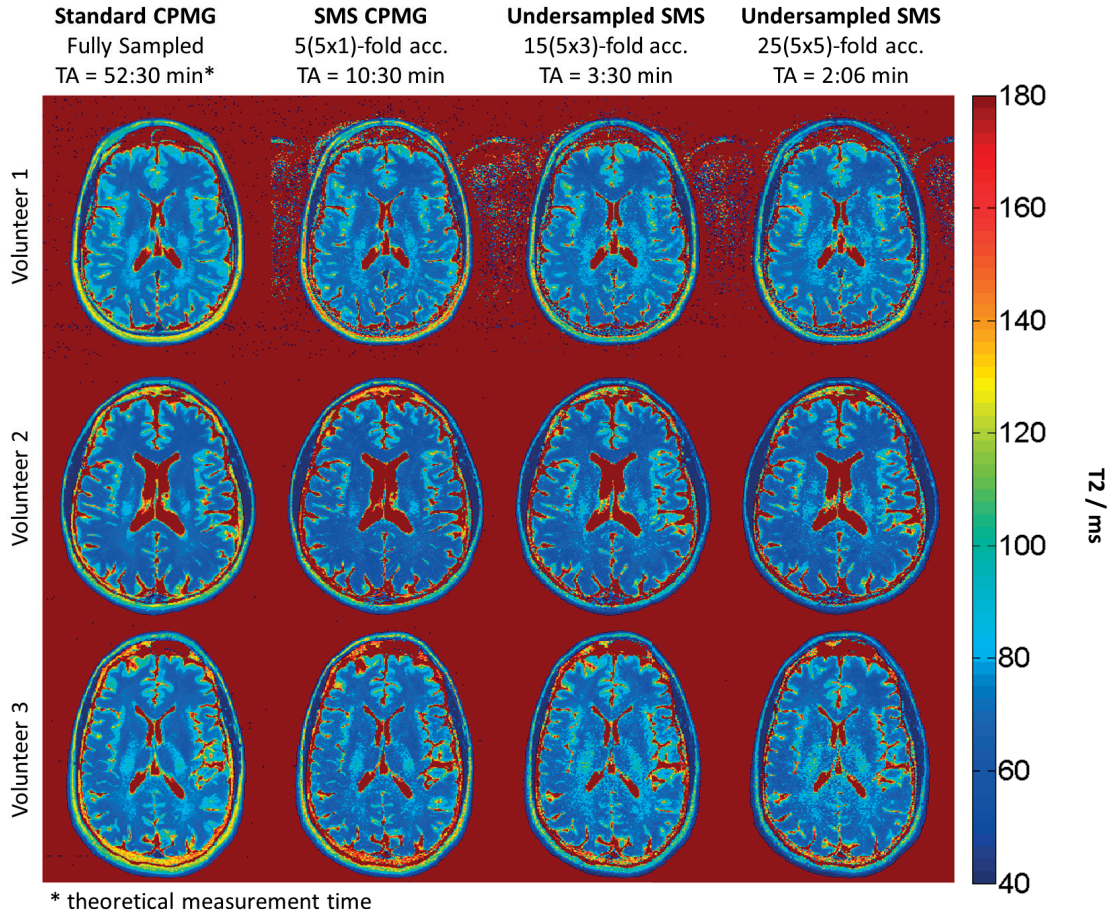


Figure 4.5: Axial slices from the T_2 maps of all volunteers that were reconstructed with the proposed method and acquired with different methods, left to right: the gold standard single-slice CPMG, SMS CPMG and undersampled SMS CPMG ($R = 3$ and $R = 5$).

4.3 Results

4.3.1 In Vivo Studies

T_2 maps from the single-slice CPMG and the SMS CPMG sequences with different acceleration factors are shown in Figure 4.5. Note that the single-slice CPMG values are considered the gold-standard measurement. A similar overall T_2 value range is observed in the SMS CPMG maps compared to the gold standard. The maps from the accelerated slice-GRAPPA reconstruction with and without additional undersampling exhibit non-uniform noise amplification. These findings are supported by comparing T_2 values drawn from the ROIs (see Table 4.1): overall, mean values of the SMS CPMG measurement are in good agreement; the acquisition of multiple slices however introduces an increase in standard deviations (SD). As an example, the T_2 values in the WM frontal lobe show a mean value of 65.6 ± 2.1 ms in single-slice CPMG versus 63.4 ± 4.8 ms in SMS CPMG. A slight additional increase in SD is observed in the

Chapter 4. Fast Model-Based T_2 Mapping using SAR-Reduced Simultaneous-Multi-Slice Excitation

		Standard CPMG fully sampled	SMS CPMG 5(5x1)-fold	SMS CPMG 15(5x3)-fold	SMS CPMG 25(5x5)-fold White
White Matter (Frontal Lobe)	Volunteer 1	65.6 \pm 2.1	63.4 \pm 4.8	62.9 \pm 5.4	64.2 \pm 5.0
	Volunteer 2	61.7 \pm 3.1	61.5 \pm 5.2	62.4 \pm 5.6	62.0 \pm 6.2
	Volunteer 3	70.4 \pm 2.5	71.3 \pm 5.4	69.9 \pm 4.0	66.9 \pm 4.6
Globus Pallidus	Volunteer 1	54.6 \pm 4.4	53.1 \pm 6.1	52.8 \pm 7.7	51.8 \pm 7.9
	Volunteer 2	46.4 \pm 4.0	46.8 \pm 6.8	46.9 \pm 7.7	45.8 \pm 10.5
	Volunteer 3	56.6 \pm 3.9	57.4 \pm 7.1	57.2 \pm 8.5	54.9 \pm 8.0

Table 4.1: Mean and standard deviation of T_2 values (in ms) within regions of interest manually drawn into the white matter of the frontal lobe and Globus Pallidus, for each subject and T_2 sequence.

undersampled SMS acquisitions, while the mean T_2 values stay in good agreement with the gold standard.

The same ROI's were used to compare T_2 values between scan and rescan within one subject and across subjects. The mean and standard deviation in ROIs of the WM and GP for each subject between scans are shown in Figure 4.6. The T_2 values differ 0.6 ms on average between scan and rescan and exhibit a low variation between scans (SD = 0.39 ms in WM, 0.43 ms in GP). The T_2 values across all subjects (within a similar age range of 27 ± 2 years) also show a small standard deviation (2.79 ms in WM, 4.40 in GP).

4.3.2 Phantom Studies

Figure 4.7 shows an agreement plot of the T_2 values from the different accelerated acquisitions with T_2 values of the single-slice, single spin-echo acquisition. All acquisitions agree well with the reference values. However, T_2 is slightly overestimated (≈ 2 ms), especially for the undersampled acquisition at lower T_2 values (< 30 ms). Furthermore, the standard deviations for low (< 20 ms) and high T_2 values (> 140 ms) are larger (≈ 8 ms versus ≈ 3 ms), presumably due to the fact that too little short echo times (for measuring low T_2 values) or too little long echo times (for long T_2 values) are sampled with the used echo spacing and number of echoes.

4.3.3 SAR Aspects

The main motivation for the proposed sequence design of using a classical MB excitation and PINS refocusing pulses was to obtain a CPMG sequence that is able to acquire many slices (e.g. 50), and echoes (e.g. 16) at a short TR (e.g. 3 s) without exceeding the SAR limitations at 3T. Pulse simulations were used to calculate the B_1^2 for every used pulse and showed that the expected SAR reduction was achieved since the PINS refocusing pulses deposit similar power ($B_1^2 = 6.3 \text{ mT}^2$) in comparison to the standard single-slice refocusing pulse ($B_1^2 = 6.9 \text{ mT}^2$), although it refocuses four more slices. This low power deposition of the PINS pulses facilitated the use of this sequence design despite the approximately five times higher B_1^2 of

the multi-band excitation (11.1 mT^2) in comparison to the single-slice excitation ($B_1^2 = 2.7 \text{ mT}^2$). With this configuration the SMS CPMG sequence was on average at 60% of the SAR limit for 50 slices during the in-vivo experiments. Contrary, the single-slice CPMG sequence reached 40% of the SAR limit, but only for the acquisition of 10 slices.

4.3.4 Computational Requirements

The image reconstruction of one dataset with 50 slices requires approximately 7 hours on an office computer with 16 GB of RAM and an Intel Core i7-3770K CPU @3.50GHz running a 64bit Windows 7 operating system.

The algorithm has its peak memory footprint when the split-slice GRAPPA kernel is applied and highly depends on the matrix size of k-space. In the case of the in-vivo experiments this corresponds to approximately 5.5 GB (matrix size 320×210 , 16 echoes, 64 coils, 5 simultaneous slices). Ironically, due to the collapsing of the undersampled k-space prior to the kernel application, the footprint is linearly reduced by the undersampling factor R.

4.4 Discussion

We have shown that the proposed multi-band/PINS simultaneous multi-slice sequence design combined with regular undersampling and an EPG signal model applied with dictionary fitting yields accurate T_2 maps of the whole brain with high resolution in two minutes.

The results show that the employed slice-profile-sensitive EPG simulation takes the major artifactual effects on the signal into account, notably stimulated echoes originating from incomplete refocusing of the spins which are inevitable due to B_1^+ field inhomogeneity and non-ideal slice profiles. However, the model is still an approximation and does not account for the detailed micro-structure of human tissue. One main assumption of the model used in this work is that it models only one compartment, i.e. one single isochronal with a specific T_2 relaxation time per voxel. This is obviously a simplification and will not account for differently behaving compartments such as intra- and extracellular water compartments. Furthermore, the model does not take magnetization transfer (MT) between free water protons and macromolecules into account which may affect the signal. Future work should hence focus on studying in more detail how these effects bias the T_2 estimation. Ideally, the model should be extended to fully incorporate these effects and additional tissue properties; this will however decrease the computational stability of the fitting and require either additional signal encoding or an optimised reconstruction to keep the same acquisition times. It should be noted, however, that despite these shortcomings, the T_2 values measured here are in good agreement with the gold-standard single-slice single spin-echo acquisition.

When accelerating, both SMS and the additional undersampling result in amplification of noise, which manifests in increasing standard deviations at higher acceleration factors. Never-

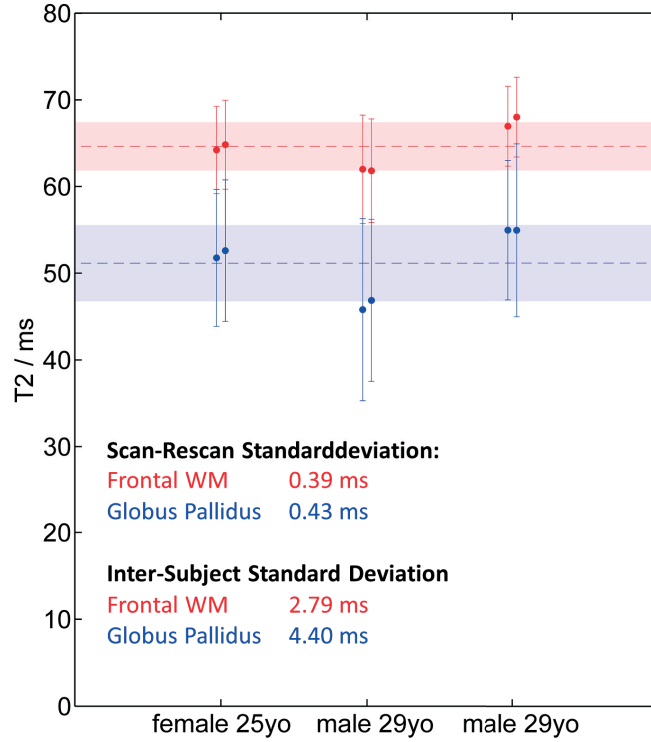


Figure 4.6: Mean T_2 values of scan and rescan for each subject with error bars indicating the standard deviation. Red are values from the white matter in the frontal lobe and blue from the Globus Pallidus. The dashed lines indicate the mean across all subjects and the filled area its standard deviation.

theless, the accuracy of the estimation remains unbiased. Furthermore, despite the increased standard deviations, T_2 values were reproducible in scan-rescan acquisitions and across subjects. This is an important observation since reproducibility is probably even more important than accuracy in a clinical context; for example, in a multiple sclerosis follow-up measurement, T_2 maps have to be comparable and even small changes might indicate pathology, e.g. an increased inflammation of the “normal appearing white matter”, something which is very hard to observe by the naked eye.

The original motivation of using PINS pulses instead of multi-band pulses were the SAR limitations, which especially come into play at 3T: the application of multiple 180° RF pulses easily exceeds the SAR limits, even with conventional single-slice acquisitions. We demonstrated that the power deposition per slice is lower with the proposed pulse scheme. Such a scheme may hence enable using spin-echo-based T_2 mapping at ultra-high fields, i.e. 7T and beyond.

One major limitation of the proposed method is that the reconstruction algorithm is rather complex in comparison to a direct Fourier Transform and mono-exponential fitting. This complexity involves multiple regularization parameters (α , λ , σ) and rather long computational times. The regularization parameters were manually optimized as it is common practice in

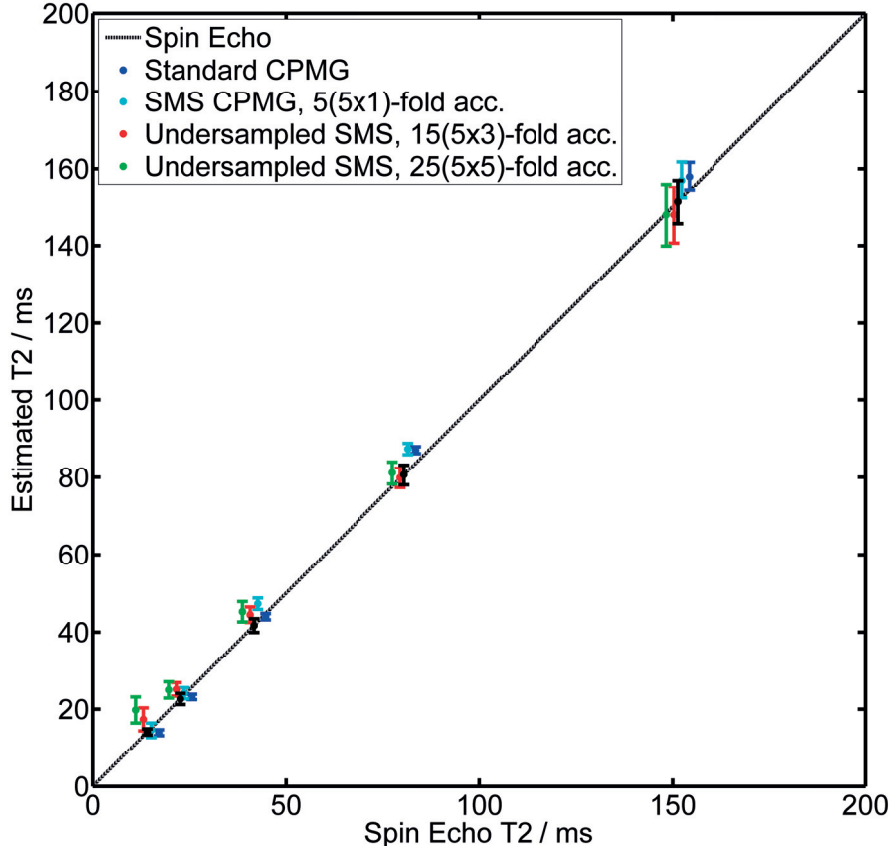


Figure 4.7: Mean T_2 values within five different compartments of a phantom from the different acquisitions reconstructed with the proposed SAFT algorithm against the reference values derived from a Spin-Echo sequence. Error bars indicate the standard deviation and the markers were horizontally jittered to minimize overlaps.

compressed sensing [30]. In future works, these parameters should be automatically adapted, also depending on image content, and maybe altered in each iteration. The long computational time of the reconstruction algorithm still prohibits its use in clinical routine. However, the performance of the current implementation on an office computer can certainly be improved with code optimization, parallelization across slices and hardware acceleration on an image reconstruction server.

An alternative combination of SMS and model-based reconstruction could be realized by solving it as a single inverse problem rather than two subsequently applied reconstructions. To that end, one has to also model the aliasing of the simultaneously acquired slices and their respective coil sensitivities within the data consistency term (equation 4.1). However, we avoided this approach since this will further increase the computational costs and we also assume that combining the reconstruction into a single inverse problem may result in a worse artifact behaviour and robustness towards model-violations (e.g. blood-flow, inaccurate coil sensitivities).

Chapter 4. Fast Model-Based T_2 Mapping using SAR-Reduced Simultaneous-Multi-Slice Excitation

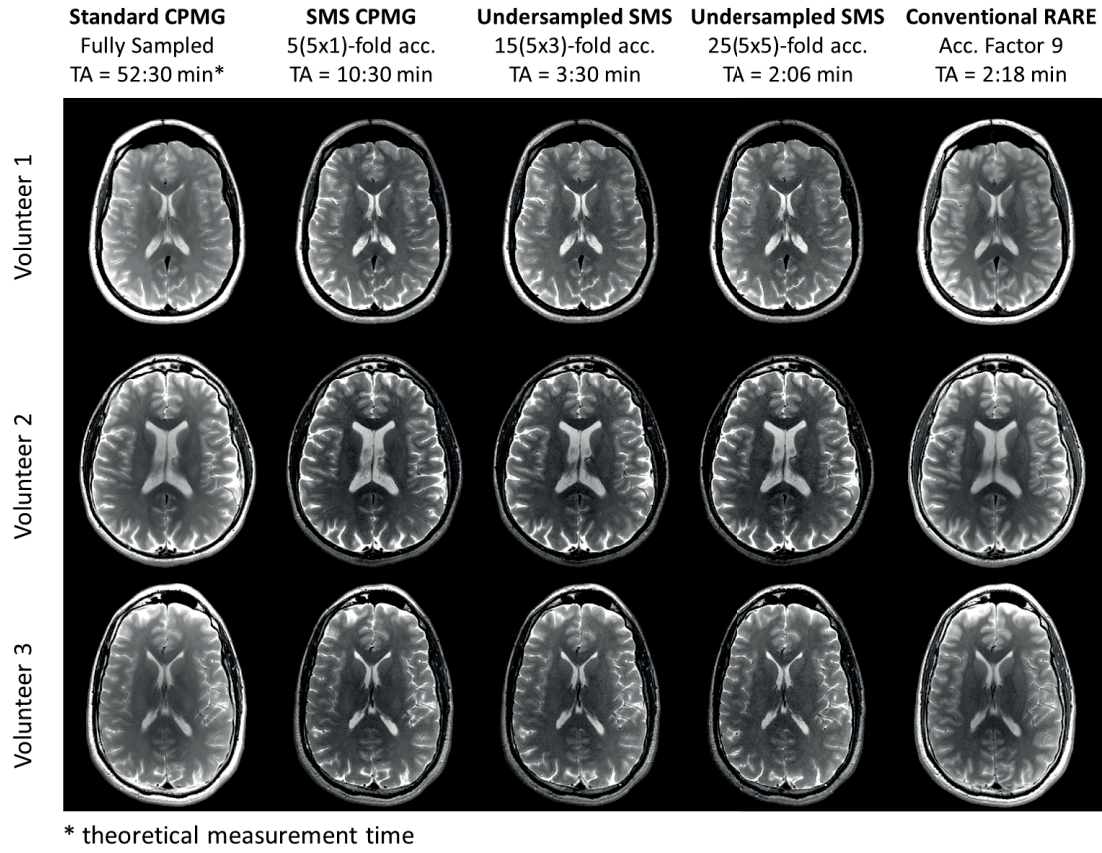


Figure 4.8: Simulated T_2 weighted contrasts from all volunteers in comparison to conventional T_2 weighted RARE images. From left to right: single-slice standard CPMG sequence, SMS CPMG sequence and undersampled SMS CPMG sequence ($R = 3$ and $R = 5$) in comparison to the gold standard RARE image. An alternative

For the integration in a clinical work-flow, it can be beneficial to synthesise conventional T_2 -weighted contrasts from the quantitative M_0 and T_2 maps. That allows providing clinicians with a regular contrast which is widely used in clinical practice while having the additional quantitative information. An example of synthesised contrast compared to real TSE acquisitions can be seen in Figure 4.8.

In future work, multi-PINS pulses, a combination of multi-band and PINS pulses [51], should be explored for quantitative mapping. These pulses may allow reducing the slice thickness without worsening the slice profile. Furthermore, applying a wave gradient during read-out [52] could help to further reduce inter-slice leakage in the slice-GRAPPA reconstruction and should be explored as well.

PINS-SAFT may be used to explore other clinical applications of quantitative T_2 mapping in a standard clinical setting. For example, in abdominal imaging, where a greater amount of slices could be acquired within a single breath-hold or even during a free-breathing sequence triggered to acquire multiple slices at end-expiration. However, we only demonstrated a proof

of concept here and larger clinical studies are required to further validate the T_2 values and the synthetically generated T_2 -weighted contrast.

In conclusion, a new sequence design was proposed that enables undersampled SMS CPMG acquisitions at 3T without exceeding SAR limits. The proposed combination of split-slice GRAPPA and a model-based reconstruction that accounts for stimulate echoes resulted in accurate and reproducible T_2 values in phantom and in in-vivo experiments of three healthy volunteers.

5 Mitigating the Effect of Magnetization Transfer in Magnetic Resonance Fingerprinting

The content of the following Chapter is based on the draft of the article: “Mitigating the Effect of Magnetization Transfer in Magnetic Resonance Fingerprinting” currently under a major revision in NeuroImage. The article manuscript was co-authored by Tobias Kober, Tiejun Zhao, Kai Tobias Block, Florian Knoll, Jean-Philippe Thiran, Gunnar Krueger, Daniel K Sodickson and Martijn A Cloos. All co-authors contributed to the idea and reviewed the manuscript.

Abstract: Magnetic Resonance Fingerprinting (MRF) is a promising new model-based technique for rapid quantitative imaging. Like with all model-based techniques, its robustness and accuracy depends on the validity of the underlying assumptions. In the case of MRE, it is generally assumed that the spin dynamics can be adequately described by the Bloch Equations, acting on a single pool of spins. In this work, we show that interactions between the solid spin pool and the free pool, called magnetization transfer (MT), can affect the MRF signal train and that the strength of the MT effect is primarily dependent on the radio-frequency (RF) bandwidth. In vivo experiments are performed to study the impact of MT on the estimated T_1 and T_2 values. Subsequently, an alternative model, which explicitly incorporates MT, is proposed to correct the T_1 and T_2 values and to mitigate their dependence on the RF bandwidth. The proposed method is tested with phantom and in vivo data, and the results are compared to literature values. Furthermore, simulations are performed to evaluate the robustness of the suggested numerical model to violations of the underlying assumptions. In conclusion, the proposed method allows for more accurate estimation of tissue relaxation in the presence of macromolecules by introducing a signal model accounting for MT into the image reconstruction.

5.1 Introduction

Quantitative magnetic resonance (MR) measurements strive to estimate tissue-specific parameters with minimal experimental bias. Until recently, such methods have mostly focused on relatively simple spin evolutions for which analytic signal solutions can be derived. Early techniques developed to measure the relaxation time, for example, relied on a series of

Chapter 5. Mitigating the Effect of Magnetization Transfer in Magnetic Resonance Fingerprinting

inversion-recovery measurements to estimate the longitudinal relaxation time (T_1) [53, 54] and spin-echo measurements to estimate the transverse relaxation time (T_2) [43, 55]. Although such measurements can provide excellent results, they are generally too long to be used in routine clinical examinations.

For years, the search for faster methods has strived to obtain a balance between acquisition speed, model simplicity, accuracy, and precision [31, 33, 56]. One of the most widely used approaches in the last years is the DESPOT1 and DESPOT2 technique [22], combining four (or more) fast measurements to quantify both T_1 and T_2 . Although DESPOT12 is fast and SNR efficient, it is also sensitive to experimental imperfections [57, 58] and magnetization transfer (MT) effects [59].

The impact of MT is especially high in the brain, and it was shown that it has significant correlations with myelin content and axonal count [60]. Therefore, MT can also be exploited as a biomarker for neurological disease where the myelination of the brain is altered, e.g. multiple sclerosis [61]. However, MT effects cannot be described by basic Bloch Equations used in most fast quantitative MRI techniques. If a comprehensive spin model is applied to these sequences, a dependency on additional experimental factors, such as the RF bandwidth, becomes apparent; this dependency can influence the T_1 or T_2 estimation accuracy. In theory, all of these effects can be corrected using information from additional measurements, but each additional scan increases the acquisition time and adds complexity, such as requirement for co-registration in the case of inter-scan motion. Moreover, each additional parameter increases the complexity of the analytical form of the signal model.

Recently, a new framework for quantitative MRI, magnetic resonance fingerprinting (MRF), has been proposed [23]. MRF moves the focus away from monotone sequences that drive the spins in a steady-state with analytic solutions. Instead, it uses more diverse sequence patterns that produce continuously changing transient states, paired with a numerical signal model. The additional degrees of freedom that become available with MRF enable faster imaging and provide the opportunity to deliberately entangle and encode multiple tissue properties and experimental conditions within a single measurement. MRF has sparked great interest in the research community, as it may enable moving from qualitative to quantitative MRI with short examination times, which would result in an extremely powerful tool for neuroscience and various clinical applications. The role of MT effects on MRF, however, has not been explored. In this work, we first demonstrate that the quantification of T_1 and T_2 values, based on MRF measurements, may be influenced by MT. Subsequently, we show that this bias can be avoided by incorporating a more comprehensive numerical signal model in combination with a small modification to the acquisition scheme.

5.2 Theory

The original MR fingerprinting implementation was modelled based on the basic Bloch Equations. These equations describe the spin dynamics assuming that the sample in each voxel

can be characterized by a single T_1 and T_2 relaxation constant in combination with the proton density PD (here denoted as M_0) that scales the overall magnitude of the signal [23]. This model accurately describes simple phantoms, such as those containing homogeneous compartments with different relaxation times. However, as for most quantitative MRI techniques, this model is only an approximation for the heterogeneous microscopic structure present in organic samples. In addition to the fact that each voxel may contain multiple free water compartments, each containing a different chemical environment with distinct effective T_1 and T_2 [62, 63], it also does not take into account that there is physical interaction between hydrogen atoms in free water molecules and those bound to macro-molecules, known as the MT effect. The partial influence of different T_1 and T_2 contributions in a single voxel leads to a reproducible best single-compartment model fit. However, neglecting the dynamic interaction between free and bound hydrogen atoms may result in a sequence- and protocol-dependent T_1 and T_2 bias. Such dependencies are obviously contrary to the idea of quantitative MR and should thus be minimized. In the next section, we will first outline the common model for magnetization transfer, as detailed by Henkelman et al. [64], from which we will subsequently construct a simplified model for use in our fingerprinting signal framework.

5.2.1 Common Model of Magnetization Transfer

The magnetization-transfer effect is typically described with a two-pool model as illustrated in Figure 5.1a. The two pools represent the net magnetization produced by hydrogen atoms in free water and those bound to macromolecules. The equilibrium magnetization of these pools is denoted as M_{0f} and M_{0b} . The spectral distribution of the pools, a narrow Lorentzian for free water and a wide super-Lorentzian for the bound pool, depend on the transverse relaxation times T_{2f} and T_{2b} , respectively. A detailed description of the line shapes can be found in Morrison et al. [65]. Due to the differences in line shape, a given RF-pulse affects each of these pools differently. In particular, the amount of saturation depends on the overlap between the pulse bandwidth and the spectral distribution of the spin pool, i.e. pulses with a larger bandwidth will saturate the solid pool more quickly. After (partial) saturation, their magnetization will return to equilibrium. In principle, each compartment can have a different characteristic longitudinal relaxation time (T_{1f} and T_{1b} in Figure 5.1a). In addition, the two pools exchange magnetization with each other at a fixed rate, described with one constant for each direction (k_b and k_f). For a more detailed description of common MT models, see Henkelman et al. [64].

5.2.2 Simplified Model

The original fingerprinting methods, which rely on the basic Bloch Equations or the Extended Phase Graph Formalism [49], consider only the T_{1f} and T_{2f} relaxation constant in combination with the proton density PD and, in some cases, experimental conditions, such as inhomogeneities in the main magnetic field B_0 [23] or variations in the radio-frequency field B_1 [47]. Considering that the proton density PD (here denoted as M_{0f}) scales the overall

Chapter 5. Mitigating the Effect of Magnetization Transfer in Magnetic Resonance Fingerprinting

magnitude of the signal, these dictionaries are generally limited to three or four dimensions.

Each new model parameter adds an additional dimension to the dictionary – scaling up the computational efforts necessary to create and use them. Thus, including the additional five dimensions required for the common MT model leads to impractical, if not infeasible, computational times for both creating the dictionary with the necessary Bloch simulations and the reconstruction itself. Furthermore, the typical MRF sequence design may not encode all these parameters strongly enough to perform reliable dictionary fitting. Therefore, we propose a simplified MT model that condenses the additional degrees of freedom into one single parameter MT^* . Although this parameter no longer reflects a quantitative MT estimation, it is designed to estimate the MT bias and enables more accurate estimation of free water pool T_{1f} and T_{2f} relaxation times.

The simplified model is realized by discretizing the longitudinal magnetization of the bound pool into multiple Nb frequency bands (1-100 Hz, 101-200 Hz, ... , 9.901-10.000 Hz). At the beginning of the simulation, the magnitude of the longitudinal magnetization M_{zb} , in each band i , depends on M_{0b} and the bound pool frequency line shape G :

$$M_{zb,i} = M_{0b}G_i. \quad (5.1)$$

Here, we used the super-Lorentzian line shape with the assumption that $T_{2b}=10 \mu s$, based on the previously reported value range of 9-11 μs [65, 66]. When applying an RF pulse, only a fraction of the bound pool bands is saturated. The level of saturation depends on the shape, flip angle, and bandwidth of the pulse. In the numerical simulation, saturation is performed by multiplying the longitudinal magnetization M_{zb} with a Gaussian saturation profile W for each band i . Therefore, the longitudinal magnetization after saturation M_{zb+1} is defined as:

$$M_{zb+1,i} = M_{zb,i}W_i. \quad (5.2)$$

For illustration, two exemplary super-Lorentzian line shapes G and exemplary saturation profiles W are shown in Figure 5.1c-d. Following each RF pulse, the longitudinal magnetization of the bound pool relaxes back towards the equilibrium state. Therefore, a relaxation operator is applied using the assumption from [66] that $T_{1b} = 1s$. To this end, the longitudinal magnetization of the bound pool M_{zb} within each band i is changed during one TR (denoted as t) to M_{zb+1} , following:

$$M_{zb+1,i} = M_{zb+1,i}E_1 + M_{0b}G_i(1 - E_1) \quad (5.3)$$

$$\text{with } E_1 = \exp(-t/T_1).$$

Furthermore, the exchange of magnetization between the bound and free water pool is simulated by applying an exchange operator, as previously suggested by Gloor et al. [67], which

mainly depends on the exchange rate parameters k_f and k_b as well as the equilibrium magnetizations M_{0f} and M_{0b} . One additional consideration that must be taken into account during application of the exchange operator is the discretization of the slice profile into N_f different flip-angle bins [23], [47] and the discretization of the bound pool into different frequency bands. Typically, the slice profile is binned to account for B_1^+ variations across the slice profile. Therefore, the transfer of magnetization from the free pool to each band in the bound pool was calculated based on the sum over the slice profile. Conversely, the transfer of magnetization to each bin in the slice profile is calculated based on the sum over the line shape of the bound pool. Thus, the longitudinal magnetization of the bound pool M_{zb} and the free water pool M_{zf} change according to:

$$M_{zb+1,i} = M_{zb,i} \exp(-k_b t) + \left(\sum_{k=0}^{N_f} M_{zf,k} \right) M_{0b} G_i (1 - \exp(-k_b t)), \quad (5.4)$$

$$M_{zf+1,k} = M_{zf,k} \exp(-k_f t) + \left(\sum_{i=0}^{N_b} M_{zb,i} \right) M_{0f} (1 - \exp(-k_f t)), \quad (5.5)$$

The exchange rates are known to be linked through the fractional pool size at equilibrium ($k_b = k_f / M_{0b}$). In the simulation, the equilibrium magnetization of the free pool is fixed to 1 – note that the PD is ultimately determined by the ratio between the simulated and measured signal. In the simplified model, the effect of MT can thus be narrowed down to two variables, the exchange rate k_f and the bound pool size M_{0b} , which can be condensed into a single scaling variable MT^* when using literature values and the assumption of having the same ratio between k_f and M_{0b} : $k_f = MT^* \times 40 s^{-1}$ and $M_{0b} = MT^* \times 0.13$ [68]. A schematic drawing of the simplified model is shown in Figure 5.1b, where the above-introduced assumptions are shown in rectangular boxes and the free parameters that need to be estimated in circles.

Notably, besides fixing parameters to literature values and condensing two parameters into a single MT^* parameter, multiple major assumptions were made to simplify the common MT model. First, the contribution of signal from the transverse magnetization of the bound pool is neglected during the simulation because the reported T_{2b} values of the bound pool ($\approx 9-11 \mu s$) are orders of magnitudes shorter than the TR in the sequence (typically 7-11 ms). Therefore, the transverse magnetization of the bound pool will dephase completely before the application of the next pulse, or even the readout. Second, following [67], the subsequent application of saturation, relaxation, and exchange operators assume that these effects can be decoupled and still yield a good approximation in comparison to solving the differential Bloch Equations.

Chapter 5. Mitigating the Effect of Magnetization Transfer in Magnetic Resonance Fingerprinting

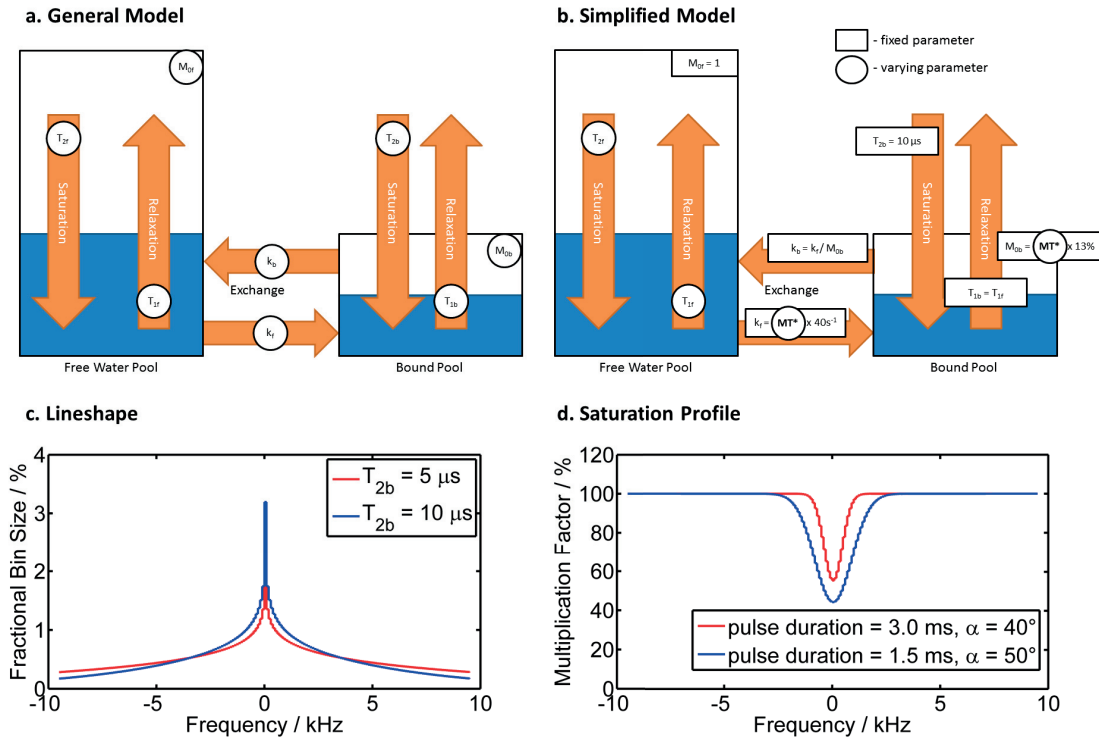


Figure 5.1: (a) Illustration of the common magnetization-transfer model with two pools and (b) simplification of the model, with boxes indicating fixed and circles indicating varying model parameters. (c) Line shape of the bound pool for different T_{2b} relaxation parameters and (d) saturation profiles of pulses with different durations and flip angles in the same frequency domain.

5.3 Methods

5.3.1 In-Vivo Experiments

To study the impact of MT, we used the prototype sequence design and reconstruction algorithm of PnP-MRF, originally proposed by Cloos et al. [47], as basis and included the simplified, two-pool MT model in the reconstruction. Four different configurations were evaluated. First, we compared the measured T_{1f} and T_{2f} values obtained when using 2 ms vs. 4 ms long excitation pulses (bandwidth 1500Hz vs. 750Hz) in the standard PnP-MRF sequence to validate that there is an observable MT effect at all. The third and fourth sequence configurations incorporated a change of the RF pulse duration at set time intervals in the RF train, as shown in Figure 5.2. We will refer to the process of changing the RF bandwidth as “MT encoding” in the rest of the paper since it introduces MT-dependent modulations of the signal, i.e. encodes MT in the fingerprints. For one dataset, the duration was varied between 1.5 ms and 3 ms, for the other between 2 ms and 4 ms, corresponding to 2000 Hz / 1000 Hz and 1500 Hz / 750 Hz, respectively.

All datasets were reconstructed as described by Cloos et al. [47], each using the corresponding

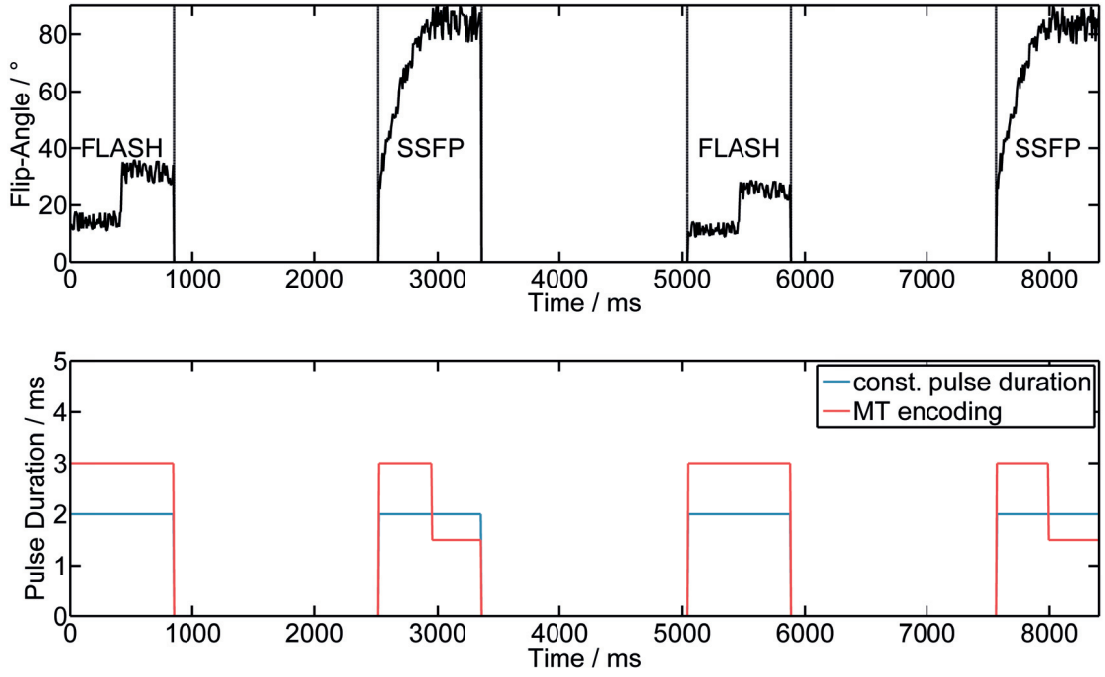


Figure 5.2: Sequence design used in this study with a train of flip angles and constant TR according to the PnP-MRF sequence. The pulse duration of MT encoding (red lines) is varied throughout the sequence.

dictionary with either a one-pool or two-pool model. The dictionary for the first two experiments using constant pulse durations was computed based on the single-pool Extended Phase Graph Formalism, including an eight-bin slice profile. Only eight bins were used since increasing the numbers of bins did not show differences in the fingerprints in a separate test (not shown). The more comprehensive, two-pool Extended Phase Graph Model was used to create dictionaries for both MT-encoded sequences (for each combination of variable pulse durations individually) and the standard PnP-MRF sequence (constant pulse duration). For both models, the transmit field B_1^+ is a free variable and, thus, an additional dimension in the dictionary.

All experiments were performed using a whole-body 3-Tesla MRI system (MAGNETOM Skyra with TimTX TrueShape, Siemens Healthcare, Erlangen, Germany). The built-in birdcage body coil was used for excitation, and a standard 24-channel phased-array head/neck coil was used for reception. An axial slice through the brain of four healthy volunteers was imaged using a matrix size of 160x160, 240mm FOV, 5mm slice thickness, TR of 7ms, and 10 radial spokes per time point. For three of the volunteers, an additional high-resolution acquisition was performed (320x320 matrix size, all other parameters remained unchanged).

The study was approved by our institutional review board (IRB). Written informed consent was obtained prior to the examination.

5.3.2 In Silico Experiments

Following the sequence parameterization used for the in-vivo experiments, several theoretical limits of the proposed simplified MT model were evaluated. Since the proposed simplified MT model assumes fixed values for T_{1b} , T_{2b} and a fixed ratio between M_{0b} and k_f , the possible bias caused by the violation of these assumptions was studied. To that end, fingerprints were generated using the two-pool model and a range of values for each parameter. The resulting fingerprints were then matched with the dictionary constructed using the fixed literature values. The resulting estimates of T_1 and T_2 were subsequently compared to the original values used to generate these fingerprints.

5.3.3 In Vitro Experiments

We assume that the bias observed in biological samples when changing the RF bandwidth originates from MT. Therefore, there should not be any bandwidth dependency when imaging a manganese chloride phantom. Furthermore, the acquisition with MT encoding and using a two-pool model should result in the same values as the gold standard and not show any MT bias, i.e. $MT^*=0$. To test this hypothesis, the same experiment as in vivo was performed on an in-house-built manganese chloride-doped phantom with seven compartments. The T_1 and T_2 values from the different pulse durations and spin models were compared to the gold-standard values estimated with multiple single-slice single spin-echo and inversion-recovery acquisitions (TR = 6.5 s, 192 x 192 matrix, 192 mm x 192 mm FOV, TI = 25, 50, 100, 200, 400, 800, 1600, 3200, 6400 ms, TE = 12, 18, 24, 36, 48, 72, 96, 144, 192, 288, 384 ms).

5.4 Results

5.4.1 In Vivo Experiments

T_1 and T_2 maps obtained with acquisitions using constant pulse durations of 2 ms and 4 ms show a clear difference (Figure 5.3a). Although the T_1 maps appear almost identical, the T_2 values obtained with the shorter pulse duration are lower. However, both seem to overestimate T_1 systematically compared to literature values [69] ($T_1 \approx 1.1$ s versus $T_1 \approx 0.8$ s) T_2 maps acquired with both pulse durations underestimate the T_2 of white matter when compared to literature values [69] ($T_2 = 40$ ms versus $T_2 \approx 60$ ms).

Figure 5.3b shows the T_{1f} , T_{2f} and MT^* maps of the same subject obtained from the data acquired using the sequence with MT encoding and a two-pool model. Now, both the T_{1f} and T_{2f} maps show values in the same range as reported in literature and appear less dependent on the pulse duration. The MT^* bias maps show a difference between the two pulse durations – MT^* values are generally higher for the 4/2ms compared to the 3/1.5ms pulse durations. The MT^* bias maps show the strongest effect in white matter, a weaker effect in grey matter, and no MT bias in cerebrospinal fluid, which correlates with the myelination of a

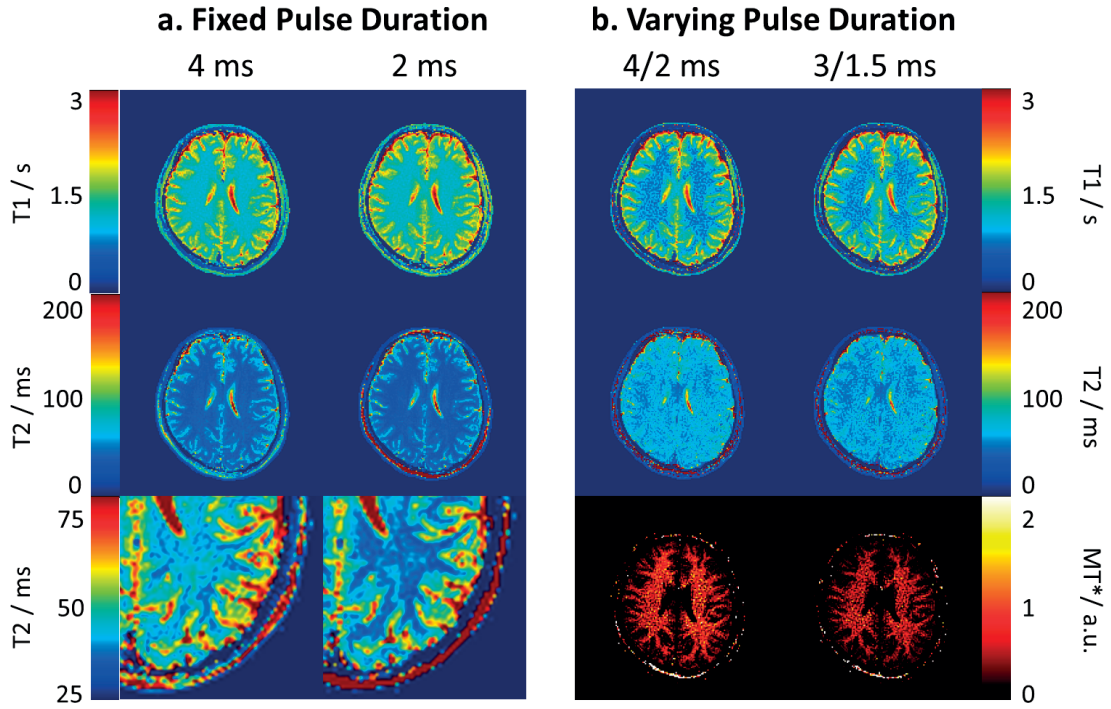


Figure 5.3: (a) Representative example of one subject showing quantitative T_1 and T_2 maps reconstructed from acquisitions with different RF pulse durations and a dictionary that does not account for magnetization transfer effects and (b) the same slice acquired with varying pulse duration (MT encoding) reconstructed using individual dictionaries that take into account the MT^* bias.

healthy brain. Furthermore, all maps experience more noise in comparison to the single-pool model, presumably due to the additional dimension in the dictionary. These results could be reproduced in all subjects for both the lower- and higher-resolution settings. Quantitative maps from all subjects obtained with MT encoding and the two-pool model are shown in Figure 5.4a. Notably, a strong MT bias is consistently observable in the corpus callosum, which could be linked to the higher fibre density and, thus, higher myelin content - i.e. increased presence of macro molecules - in these regions. The quantitative maps acquired at higher resolution, as example shown for one subject in Figure 5.4b, exhibit lower SNR, but T_1 and T_2 values are comparable to the low-resolution acquisitions Figure 5.5a-b show the mean T_1 and T_2 values from all subjects within the occipital white matter in a box plot. Notably, T_2 values between different pulse duration settings considering only a single pool show a significant difference ($p = 0.03$), whereas using MT encoding and a two-pool model, values do not show a significant difference any more. Furthermore, the acquisitions using the two-pool model and MT-encoding yield T_1 and T_2 values closer to literature values.

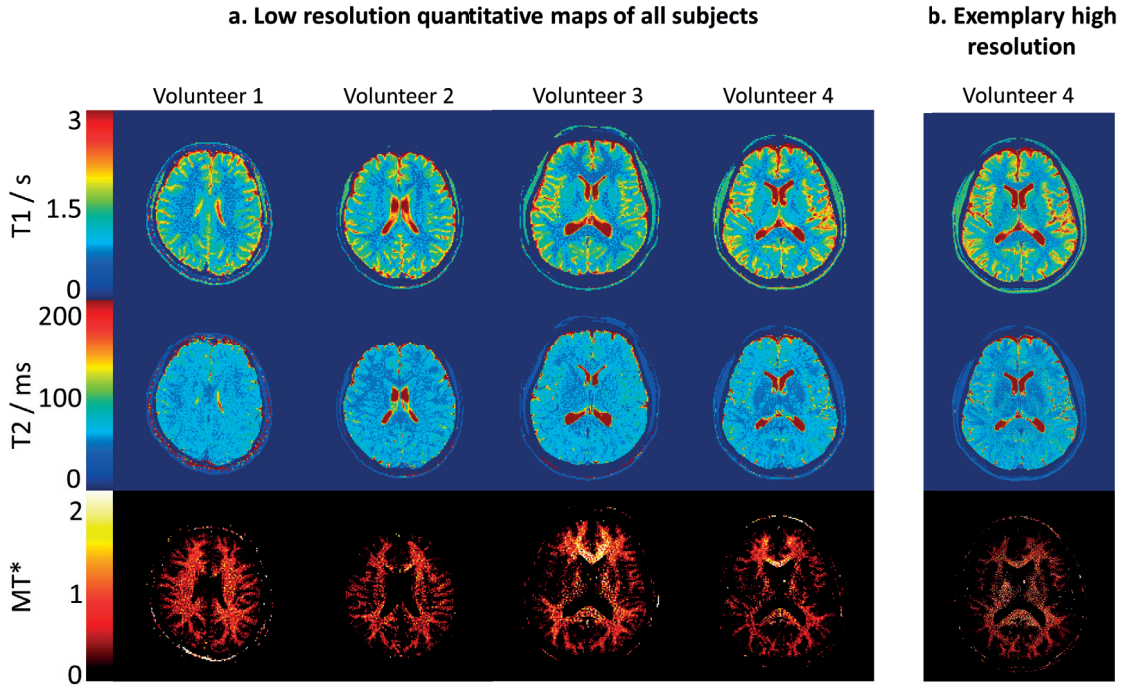


Figure 5.4: (a) Quantitative T_1 , T_2 and MT^* maps obtained with MT-encoding (3/1.5 ms pulse durations) and a two-pool model. (b) Example quantitative maps acquired with the same protocol parameters but in higher resolution.

5.4.2 In Silico Experiments

Fingerprints obtained from the dictionaries simulated with and without taking into account MT are compared in Figure 5.6. The two simulated tissues “A” (no MT) and “B” (with MT) show different signal evolutions (Figure 5.6a). In particular, the Steady-State Free-Precession (SSFP) section of the sequence results in lower signal intensity due to the loss of longitudinal magnetization transferred to the bound pool. This signal drop is similar to a fingerprint with shorter T_2 , longer T_1 , and no MT effect and creates thus ambiguous dictionary entries (Figure 5.6b). It may explain the overestimation of T_1 and underestimation of T_2 observed in the in vivo experiments (Figure 5.3a). Even if the MT effect is modelled, the dictionary still contains fingerprints that cannot be mapped uniquely to one combination of T_1 and T_2 since very similar signal evolutions are simulated using a different set of tissue properties (Figure 5.6b). Varying the pulse duration in the RF train (MT encoding) reduces this ambiguity, allowing MT effects to be distinguished from T_2 (Figure 5.6c).

Simulated fingerprints that deliberately violate the assumptions in the simplified MT model were matched to the proposed dictionary that was built assuming fixed values for T_{1b} , T_{2b} , M_{0b} , and k_f . The T_{1f} , T_{2f} , and MT^* observed in these experiments are plotted in Figure 5.7. In general, the model appears to be relatively insensitive to such variations. It can be observed that deviations from the proposed assumptions may lead to variations in the quantification of MT^* , but do not affect the estimation of the relaxation parameters that characterize the free

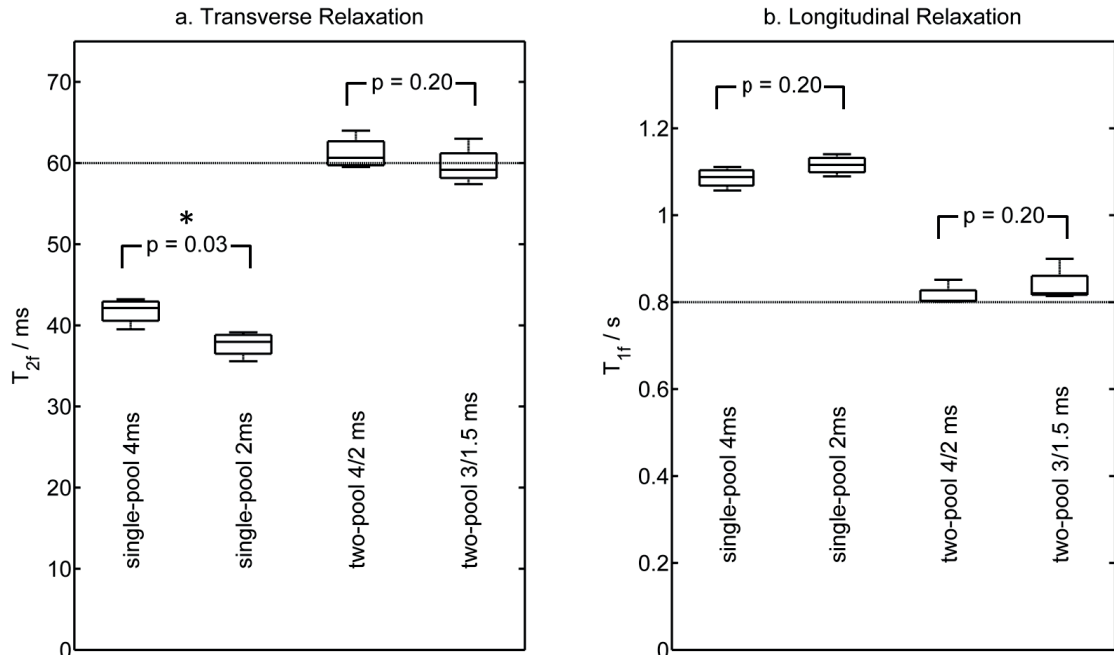


Figure 5.5: The estimated mean relaxation values (c) T_2 and (d) T_1 , measured in occipital white matter of all subjects ($N = 4$). Wilcoxon rank-sum tests show only in the single-pool T_2 values a significant difference ($p = 0.03$, see also asterisk) between pulse durations. Horizontal lines indicate expected literature values.

water pool. In more detail, the MT model assumes that T_{1b} equals T_{1f} , and it can be seen that the quantification is fairly robust to violations of this assumption. However, a small linear bias of T_{1f} can be observed when the T_{1b} of the bound pool is varied in a range of 200 ms around the correct assumption. Furthermore, T_{1f} and T_{2f} are very stable when T_{2b} is varied, meaning that the estimation is rather independent from the line shape of the bound pool. Stronger effects can be seen when the bound pool size (as a fraction of the free-water pool size) or the exchange rate is varied. A proportional bias in the quantification of MT can be observed, which compensates for the violation of the assumption and, thus, still yields accurate T_{1f} and T_{2f} estimates. In conclusion, the simulations demonstrate that the assumptions mainly affect the quantification of the MT pool and allow for more accurate estimation of the free-water pool relaxation if MT effects are present.

5.4.3 In Vitro Experiments

The quantitative T_1 and T_2 values obtained from the phantom experiments in comparison to the gold-standard methods for both the single- and two-pool model are shown in Figure 5.8. Estimations from the single-pool model, two-pool model, and different pulse durations result in similar T_1 and T_2 values that showed no significant difference to the gold-standard methods. However, values from the two-pool model showed higher standard deviation, which presumably originates from fitting an additional parameter (MT^*). Furthermore, the results

Chapter 5. Mitigating the Effect of Magnetization Transfer in Magnetic Resonance Fingerprinting

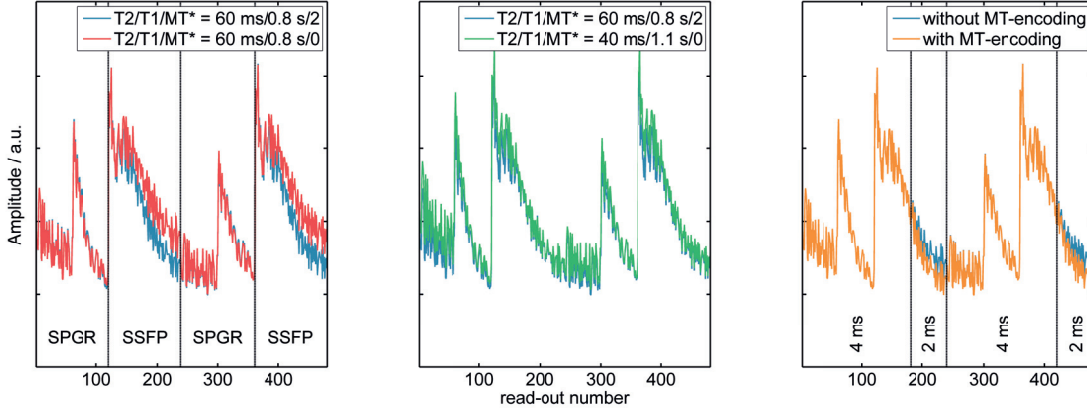


Figure 5.6: Comparison of different fingerprints generated using the proposed model to demonstrate the effect of MT. (a) Comparison of finger-prints with identical relaxation ($T_1=800$ ms, $T_2=60$ ms) but with (grey) and without (red) MT. (b) Comparison of the same fingerprint with MT effect (grey) to a fingerprint without MT but different relaxation (green, $T_1=1100$ ms, $T_2=40$ ms), demonstrating the ambiguity of the resulting signal evolutions. (c) Demonstration of the same fingerprint ($T_1=800$ ms, $T_2=60$ ms, $MT^*=1$) but with the difference when using MT encoding (orange) in comparison to constant pulse duration (grey).

appear to be unaffected by changing the pulse duration, and the two-pool model only shows noise in the MT^* map, which indicates that the previously observed bias is a biological effect that is not present in a typical phantom, further supporting the theory that the bias originates from MT.

5.5 Discussion

Our results provide evidence of the possible influence of MT when using MRF to quantify T_1 and T_2 values in the brain. Therefore, we propose a signal model that encompasses MT bias to eliminate these effects from MRF quantification measurements.

When using the PnP-MRF sequence, the observed T_2 value of white matter is dependent on the RF pulse duration and, in general, appears to underestimate T_2 and overestimate T_1 compared to literature values. Notably, this bias is not present in in-vitro experiments, which indicates that it originates from the biochemical complexity of the in-vivo environment that cannot be captured using a phantom containing uniform liquid samples. These observations are in line with the predictions from the theoretical model. Shorter pulse duration, i.e. broader pulse bandwidth, saturates the bound pool more rapidly, which results in a loss of magnetization in the free-water pool due to magnetization transfer.

The introduced simplified two-pool MT model reflects the micro-structure within the voxel better, thus resulting in more accurate T_1 and T_2 estimations. However, this model was highly simplified by including many assumptions, e.g. by fixing model parameters to literature

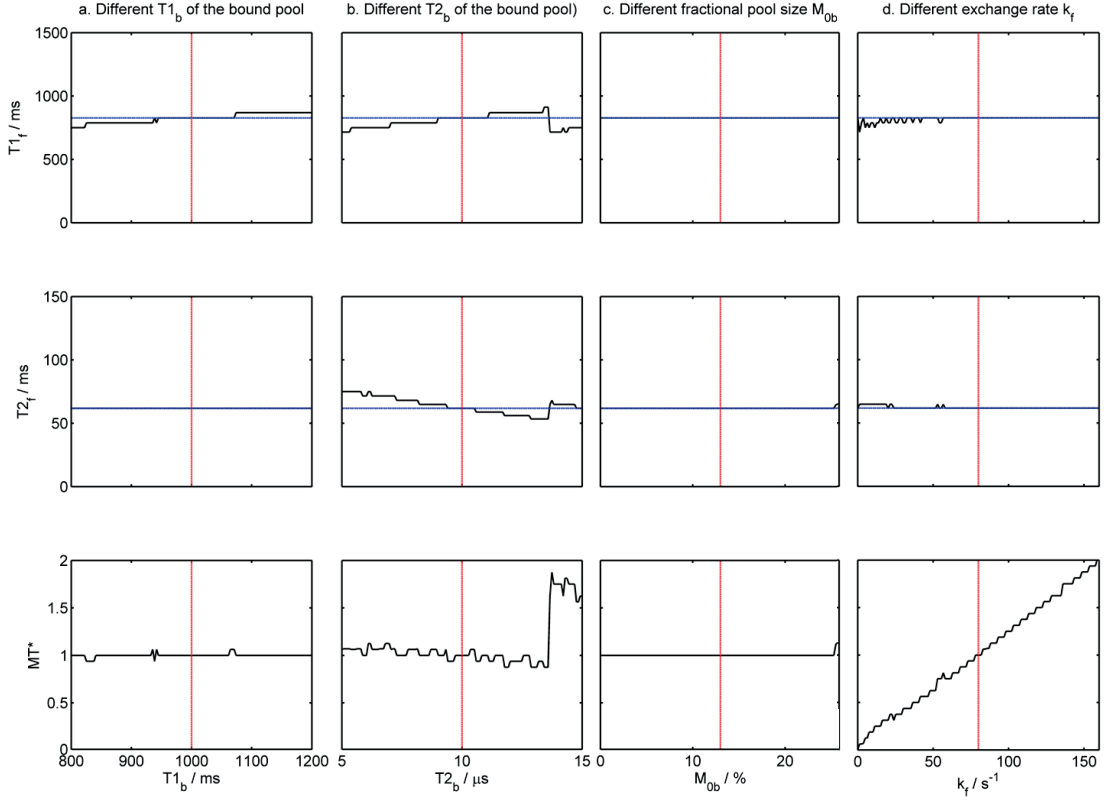


Figure 5.7: Estimated quantitative T_{1f} , T_{2f} , and MT^* values (black) compared to the ground truth used in the simulation of the fingerprint (blue dotted line) in dependency of violating the assumption of fixed T_{1b} , T_{2b} , M_{0b} , and k_f . The parameter combination where all the assumptions are met is marked with a red dotted line.

values. Furthermore, it is assumed that brain tissue has not more than two pools and multiple compartments, and physiological effects such as diffusion and perfusion are neglected. The proposed model is thus still an approximation of the actual micro-structure and biochemical environment. Ideally, the simulation of the fingerprints would use a complete model of tissue micro-structure. Apart from the computational time needed to compute such a dictionary, the fitting robustness would likely suffer as many of the more subtle effects are poorly encoded within the fingerprint. For example, although MT is better reflected in the fingerprint by varying the pulse duration during the sequence, the difference is still small and, thus, yields relatively noisy MT^* bias maps as seen in our experiments. In a more general scope, one open research question is thus how much detail is required to model tissue micro-structure and how well these effects can be encoded within a fingerprint. In the opinion of the authors, the first and foremost criterion is the reproducibility of the tissue property estimation, which should be independent from sequence parameters. With the proposed two-pool model, the applied PnP-MRF sequence has become less dependent on the pulse duration and, therefore, provides improved reproducibility. Although the two-pool model relies on certain assumptions regarding the measured sample, the estimation error caused by possible violations of these

Chapter 5. Mitigating the Effect of Magnetization Transfer in Magnetic Resonance Fingerprinting

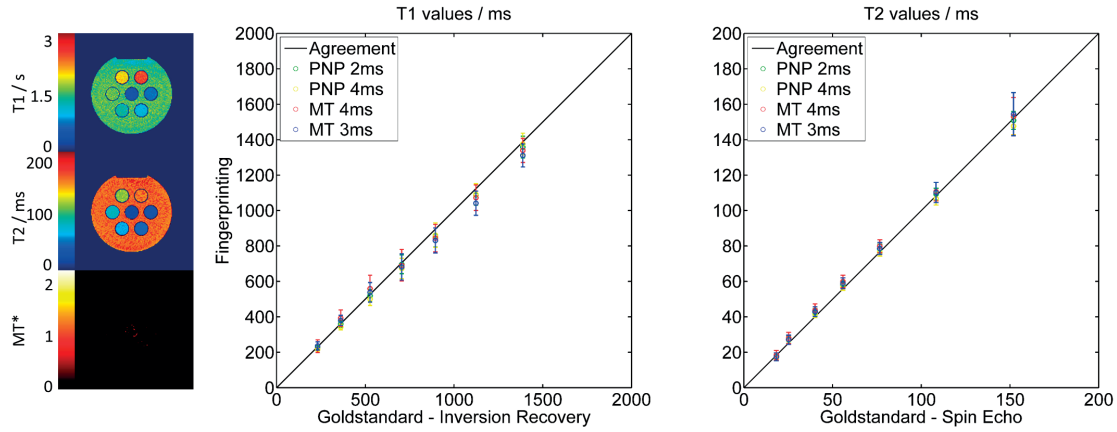


Figure 5.8: Exemplary quantitative maps from a phantom obtained with MT encoding and a two-pool model (3 ms and 1.5 ms varying pulse duration). The mean and standard deviation of the compartments from the different methods, constant pulse duration (PNP 2 ms and 4 ms) and MT encoding (MT 4 ms and 3 ms), are plotted against gold-standard values obtained from single spin-echo and inversion-recovery sequences.

assumptions will mainly be reflected in the MT^* and not in the estimation of T_1 and T_2 , as it was demonstrated in the performed simulations. As a consequence, the signal model proposed here does not allow for quantification of MT.

Alternatively, one could also attempt to minimize MT bias effects by desensitizing the sequence. For example, a longer TR will allow the bound pool to recover more longitudinal magnetization between excitation pulses but leads to less efficient acquisition times. Furthermore, longer pulse durations with a narrower saturation profile in the frequency domain could be considered to minimize the effect on the bound pool. However, longer pulse duration will also require longer TR, leading again to a less efficient acquisition. The sequence design, i.e. flip angles and spoilers, has an impact on the MT effect as well. Here, the experiments used the PnP-MRF sequence design. Other sequence designs or reconstruction methods may be less sensitive to MT and may result in a different bias, in terms of effect size and direction (overestimation vs. underestimation). This should be further investigated.

Future work should also focus on the phantom design to better reflect the micro-structure of tissue and to incorporate multiple pools or compartments. The performed phantom experiments did not show any dependency on pulse duration whereas the in-vivo experiments did. Therefore, quantitative validation of the MT effect is difficult, as standardized phantoms to measure the impact are not available.

For simplicity, all experiments were performed using a single-slice acquisition. The acquisition of multiple slices, interleaved or sequential, will introduce further saturation of the bound pool that needs to be accounted for in the spin history: the on-resonant pulses from other slices cause off-resonance saturation of the bound pool elsewhere, depending on the relative slice distance and used slice-selection gradient [70]. The model proposed here can be easily

extended to interleaved multi-slice acquisition by applying additional shifted saturation profiles, as shown in Figure 5.2, according to the slice order. This modification will, however, restrict the slice parameters of the acquisition protocol to the trained dictionary.

In general, the MT effect and its impact on the accuracy of the relaxation estimation should be further studied in the context of MR fingerprinting. The model proposed here should be further investigated to improve SNR efficiency and to explore the possibility of a more complete quantification of the MT parameters, e.g. independently fitting the exchange rate and fractional pool size. Quantitative MT would be of high interest for application in the brain, as the myelin sheaths surrounding the axons mainly consist of macromolecules. Therefore, it may potentially be applicable as an early marker for demyelination.

In conclusion, it was demonstrated that the MRF relaxation parameter estimation can be influenced by the RF pulse duration. Based on the hypothesis that these effects are caused by MT, the numerical model used to simulate the fingerprints was extended to a simplified two-pool model. Additionally, the original PnP-MRF sequence design was modified to apply different pulse durations in the RF train to better differentiate between MT and T_2 effects in the fingerprint. The proposed modification provided parametric maps that are shown to be less dependent on the pulse duration. The obtained quantitative values correspond well with those reported in the literature.

6 True constructive interference in the steady state

The content of the following Chapter is based on the postprint version of the article: “True constructive interference in the steady state (trueCISS)” published in Magnetic Resonance Imaging (DOI: 10.1002/mrm.26836). The article was co-authored by Damien Nguyen, Jean-Philippe Thiran, Gunnar Krueger, Tobias Kober and Oliver Bieri. Damien Nguyen contributed equally to this work and the remaining co-authors contributed to the idea and reviewed the manuscript.

Abstract: The purpose of this chapter is to introduce a novel time-efficient method, termed true constructive interference in the steady state (trueCISS), that not only solves the problem of banding artifacts for balanced steady-state free precession (bSSFP) but also provides its genuine, that is, true, on-resonant signal. After a compressed sensing reconstruction from a set of highly under-sampled phase-cycled bSSFP scans, the local off-resonance, relaxation time ratio, and equilibrium magnetization are voxel-wise estimated using a dictionary-based fitting routine. Subsequently, on-resonant bSSFP images are generated using the previously estimated parameters. Due to the high undersampling factors used, the acquisition time is not prolonged with respect to a standard CISS acquisition. From a set of 16 phase-cycled SSFP scans in combination with an eightfold undersampling, both phantom and in vivo whole-brain experiments demonstrate that banding successfully can be removed. Additionally, trueCISS allows the derivation of synthetic bSSFP images with arbitrary flip angles, which enables image contrasts that may not be possible to acquire in practice due to safety constraints. TrueCISS offers banding-free bSSFP images with on-resonant signal intensity and without requiring additional acquisition time compared to conventional methods.

6.1 Introduction

In the last decades, the use of steady-state free precession (SSFP) sequences rapidly has increased. Among the different variants first introduced by Carr in 1958 for NMR spectroscopy [71], balanced SSFP (bSSFP) in particular offers the highest signal-to-noise ratio (SNR) per unit of time among all MRI sequences [72]. However, bSSFP imaging is prone to field inhomogeneities [71, 73] that may lead to signal voids; these appear as dark bands in the image and

thus frequently are referred to as banding artifacts.

Commonly, banding is addressed by a series of multiple bSSFP acquisitions with different radio frequency (RF) phase-cycling schemes, in combination with a suitable reconstruction method, such as maximum-intensity projection [73], complex sum [74], sum of squares and magnitude sum [75], or other [76]. The most common approach, termed constructive interference in the steady state (CISS), acquires only two phase cycles and combines them with a maximum-intensity projection, offering a good trade-off between acquisition time and banding artifact reduction. A major drawback of these image-based combinations is that the derived pixel intensity no longer reflects the genuine, that is, on-resonant bSSFP signal magnitude typically presumed for quantification techniques based on bSSFP sequences. For low flip angle bSSFP acquisitions, these methods tend to modify the intrinsic bSSFP signal (see Figure 6.1c–d), which can impede the radiological assessment because clinicians usually are more familiar with the on-resonant, that is, genuine, bSSFP contrasts.

An introductory example of this behaviour is presented in Figure 6.1, showing the signal behaviour and contrast difference (to the on-resonant signal) for various multiple acquisition techniques based on the bSSFP magnetization derived with the Freeman-Hill formula [77] ($T_1/T_2 = 870/70$ ms, repetition time (TR) = 5 ms and off-resonances between 0° and 360°) for a flip angle of 15° (Figure 6.1a,c) and for a flip angle of 50° (Figure 6.1b,d). Generally, the combined signal and thus the contrast, as generated with the various reconstruction methods, deviates from the genuine bSSFP signal properties and strongly depends on the flip angle as well as on the tissue properties. Typically, the prominent T_1/T_2 image contrast, as commonly associated with bSSFP, only can be achieved over the complete frequency spectrum in the limit of a 90° flip angle [77]. Furthermore, most of the multiple-acquisition combination techniques assume that the steady-state signal resembles a plateau within the passband region, that is, for off-resonances within $\pm 1/(3 \text{ TR})$ for phase-cycled bSSFP, which only is true in the high flip angle regime. This may pose considerable problems due to specific absorption rate (SAR) limitations; especially at higher field strengths.

Consequently, it is much more advantageous to use parameter estimation techniques to derive bSSFP artifact free images from a signal model coupled with an optimization algorithm [78, 79, 80, 81]. To the best of our knowledge, the most recent work was reported by Björk et al. [79], in which the Freeman-Hill formula [77] was fitted onto four phase-cycled bSSFP images using a linearised signal model in combination with linear least-square fitting followed by a Gauss-Newton non-linear search (LORE-GN).

Generally, parameter estimation techniques require multiple phase-cycled acquisitions to provide a well-conditioned framework for the fitting procedure. Obviously, this leads to longer acquisition times compared to a conventional CISS acquisition requiring only two phase cycles. In this regard, the acceleration of exhaustive data scans using compressed sensing techniques has become more and more practicable, overall providing high acceleration factors [30] especially for applications with additional dimensions such as the time domain in car-

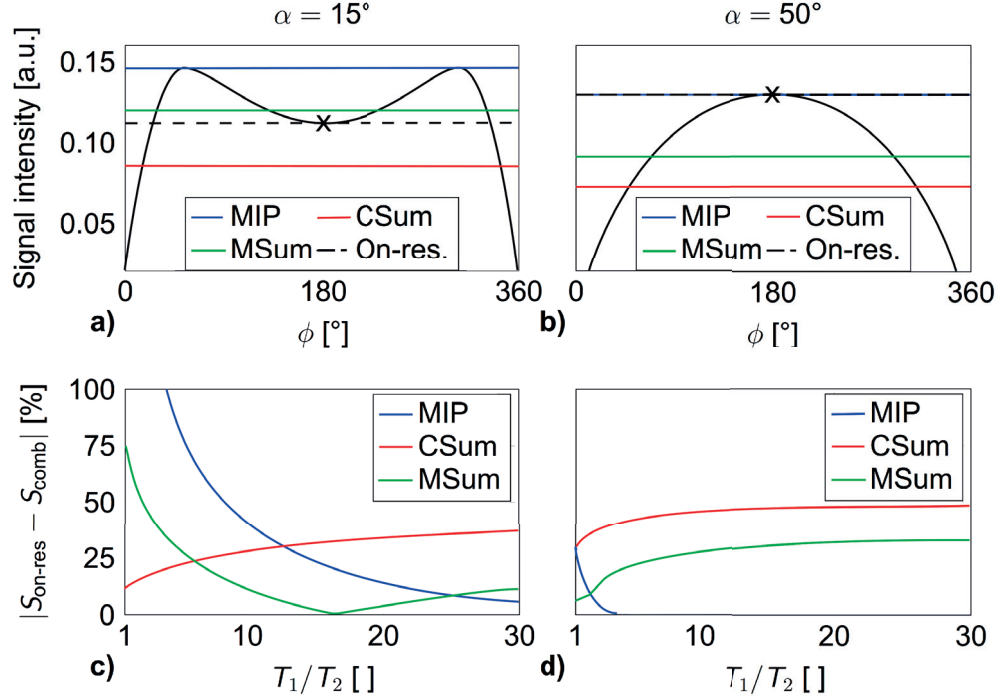


Figure 6.1: MIP CSum and MSum reconstruction of 16 phase-cycled complex bSSFP profiles for $T_1/T_2 = 870/70$ ms, repetition time=5 ms, for a flip angle of 15° (a) and for a flip angle of 50° (b). For completeness, a single bSSFP frequency response profile also is shown, indicating the on-resonant signal amplitude (X). Relative deviation between the on-resonant bSSFP signal amplitude and the average combined signal intensity for the various methods for a low flip angle 15° (c) and a high flip angle (d). Note how the contrast between tissues is more dependent on their relaxation time properties in the low flip angle regime. bSSFP, balanced steady-state free precession; CSum, complex sum; MIP, maximum intensity projection; MSum, magnitude sum; T_1 , longitudinal relaxation time; T_2 , transverse relaxation time; TR, repetition time; on-res, on-resonant; comb, combined.

diovascular imaging [82]. The acquisition of multiple phase cycles within the CISS sequence reflects such an additional dimension with redundant information, allowing high acceleration factors, as already demonstrated by Cukur et al. [83] and Ilicak et al. [84].

In this article, we propose to use a compressed sensing reconstruction in combination with a dictionary-based parameter estimation technique to retrieve the genuine bSSFP signal (i.e., independent from a multiple-acquisition combination technique and used flip angle) from a set of highly undersampled bSSFP scans with different phase-cycling schemes. The estimated parameters are then used to reconstruct artifact free images with a pixel intensity that reflects the true, on-resonant, bSSFP signal amplitude. Due to the high undersampling, this results in scan times comparable to conventional CISS imaging. In addition, because all relevant parameters (i.e., M_0 and T_1/T_2) are known, synthetic bSSFP contrast images can be derived from these data, which are not directly measurable in practice.

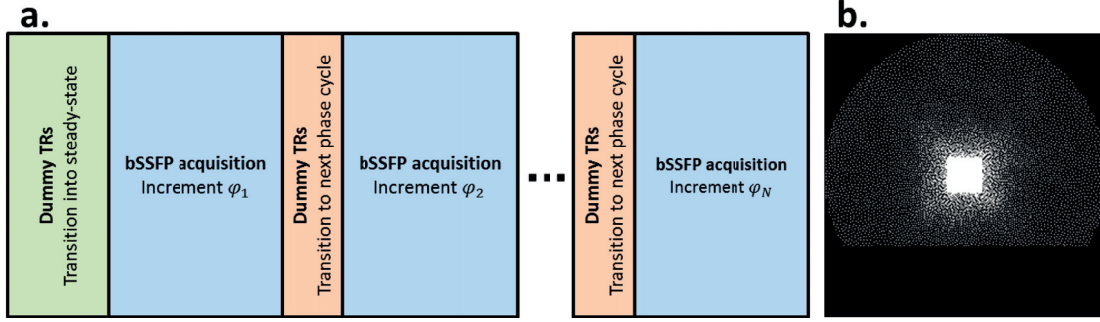


Figure 6.2: Diagram of a true constructive interference in the steady state acquisition in which each blue block represents an undersampled 3D bSSFP acquisition with different RF phase-cycling scheme (RF phase increment). Initially, some dummy TRs (green block) are played out to allow transition into steady state. In between the bSSFP acquisitions, a fixed number of dummy TRs (red blocks) are played out with linearly increasing RF phase increments (from ϕ_j to ϕ_{j+1}) to mitigate transient effects (a). Exemplary k-space sampling pattern for a scan with a phase-encoding matrix size of 320x320. White pixels indicate sampled k-space locations, whereas black pixels show ignored k-space points (b). bSSFP, balanced steady-state free precession; RF, radiofrequency; TR, repetition time.

6.2 Methods

6.2.1 Acquisition

A conventional bSSFP sequence was modified to acquire within a single scan a set of N acquisitions with constant but distinct RF phase increments (ϕ_i). Throughout this work, we only consider the simplest scheme of equidistantly distributed RF phase increments:

$$\phi_i = \frac{2\pi}{N} (j - 1), j = 1, 2, \dots, N. \quad (6.1)$$

A schematic representation of the acquisition scheme can be found in Figure 6.2a.

To shorten the overall scan time, a highly undersampled pseudo-random phase-encoding scheme, based on a variable-density Poisson disk distribution [85][86, 87, 88], was implemented to generate a different incoherent sampling pattern for each phase cycle. Additionally, elliptical scanning, that is, skipping of k-space samples at the edges of k-space [88]; and partial Fourier, that is, omitting parts of k-space by allowing the compressed sensing algorithm to intrinsically exploit its complex conjugate symmetry (see chapter 13.7 in [13]), are applied to further reduce scan time. A fully sampled reference region in the centre of k-space is acquired for every phase-cycled scan to estimate the coil sensitivities used during reconstruction [45]. An exemplary sampling pattern for a single acquisition is shown in Figure 6.2b.

6.2.2 Reconstruction

We consider a train of RF pulses with a constant flip angle, α , and a constant RF phase increment, ϕ , in combination with balanced gradient moments. As commonly done, finite RF pulse effects as well as magnetization transfer (MT) and diffusion effects are neglected. In the limit of a TR much smaller than the transverse (T_2) and longitudinal (T_1) relaxation times, the complex bSSFP signal is approximatively given by (see also ref [89]),

$$M_+(\alpha, \phi_j, \Phi, \Lambda) \approx M_0 \frac{2 |\cos(\Phi - \phi_j)| \sin \alpha}{1 + \cos \alpha + 2 \cos(\Phi - \phi_j) + (4\Lambda - 2 \cos(\Phi - \phi_j) \sin^2(\frac{\alpha}{2}))} \quad (6.2)$$

In Equation 6.2 M_0 denotes the equilibrium magnetization; $\Lambda \equiv T_1 / T_2$ refers to the relaxation time ratio; ϕ refers to the RF pulse phase increment (see also Equation 6.1); and Φ refers to the local phase offset due to field inhomogeneities. TrueCISS images are reconstructed as outlined below. In short,

1. A compressed sensing reconstruction is used to recover all missing samples from the incoherent undersampled acquisition scheme. This results in a series of fully sampled bSSFP images featuring different RF phase increments ϕ_j .
2. From the signal model (see also Equation 6.2), the three parameters (M_0 , Λ , and Φ) are estimated using a dictionary-based fitting algorithm.
3. An on-resonant bSSFP signal image, termed true-CISS, is derived from the parameter maps.

The compressed sensing reconstruction of the undersampled bSSFP data combines a Fourier transformation (F) across the ϕ -dimension and a wavelet transformation (Ψ) in the spatial domain [30, 31, 90] as sparse regularization. The first of the sparsifying transformations relies on the inherent periodic nature of the bSSFP signal along the phase-cycle dimension. Because of that property, the bSSFP profile can be expressed as a Fourier series [91] with rapidly decaying Fourier coefficient amplitudes, thus providing a sparse representation. This result can also be derived rigorously using the Fourier representation of the SSFP signal, also known as SSFP configuration theory [92]. The following cost function was used for the optimization problem:

$$L(Y_c, \lambda) = \frac{1}{2} \sum_c \|PF_{xy}\{C_c X\} - Y_c\|_2^2 + \lambda \|\Psi_{xy}\{F_\phi\{X\}\}\|_1 \quad (6.3)$$

where the first term ensures consistency between measured and estimated data, and the second term enforces sparsity. In Equation 6.3, X refers to the estimated fully sampled bSSFP image series, C_c to the complex coil sensitivities, Y_c to the measured under-sampled k-space

data, P to the sampling pattern represented as a binary mask, and λ is a regularization parameter. The cost function is minimized using the split algorithm proposed in [48], which provides better conditioning of the optimization problem and thus results in faster convergence as compared to conventional techniques. Calculation of the complex coil sensitivities was performed in two steps: the first order SSFP echo image was estimated using a Fourier analysis of the fully sampled k-space centres [93], then the coil sensitivities were computed using an eigenvalue-based estimation [45] on the previously obtained image.

After the compressed-sensing reconstruction, a dictionary based algorithm is used to yield voxel-wise estimates for M_0 , Λ , and Φ from Equation 6.2 because Equation 6.2 has multiple local minima and is not differentiable at $\phi - \Phi = \{\frac{1}{2}\pi, \frac{3}{2}\pi\}$. In contrast to conventional optimization algorithms such as gradient descent methods, dictionary-based fitting only requires knowledge of the forward signal model. To that end, a dictionary of signals with $\Lambda = \{1, 1.1, 1.2, \dots, 30\}$ and $\Phi = \{0^\circ, 5^\circ, 10^\circ, \dots, 355^\circ\}$ is generated from Equation 6.2 for $M_0 = 1$ and the actual imaging parameters that were used to acquire the data (i.e., ϕ_j and α). This allows comparison of the acquired signal in each voxel to the simulated signals in the dictionary using the squared norm (L2-norm) of the difference as a distance metric. The dictionary entry with the smallest distance to the measured data is considered the best least-squares approximation of the acquired signal. Its corresponding Λ and Φ values are then attributed to the voxel. Because M_0 is fixed during the training of the dictionary, the simulated and acquired signals need to be normalized to account for variations in M_0 before the comparison. To that end, scaling factors are calculated with $s_{sim} = \|M_{sim}\|_2^{-1}$ for the simulated signal in the dictionary and $s_{acq} = \|M_{acq}\|_2^{-1}$ for the actual acquired signal, in which M_{sim} and M_{acq} denote the discrete signals, respectively. The equilibrium magnetization is then estimated using these scaling factors with $M_0 = s_{sim}/s_{acq}$.

Finally, genuine on-resonant bSSFP images, termed true constructive interference in the steady state (trueCISS), are reconstructed from Equation 6.2 in the limit of $(\phi - \Phi) \rightarrow 0$ in combination with the estimated M_0 and Λ parameter maps. Moreover, synthetic image contrasts, such as images featuring a different flip angle than the measured one, can be derived. It also is possible to adjust the flip angle independently for each voxel to locally maximize the bSSFP signal, termed maxCISS, using [13]:

$$M_{max}|\Theta=\Theta_{opt} \approx \frac{1}{2} M_0 \Lambda^{-1/2} \text{ where } \Theta_{opt} \approx \cos^{-1} \left(\frac{\Lambda - 1}{\Lambda + 1} \right) \quad (6.4)$$

6.2.3 Simulations and Imaging

All numerical simulations, data analysis, and visualizations were performed using MatLab 8.5 (MathWorks, Natick MA). Measurements and calibrations were performed on a clinical 3T whole-body system (Magnetom Prisma, Siemens, Erlangen, Germany) with actively shielded magnetic field gradient coils using a commercially available 20-channel head coil. Prior to scanning, informed written consent was obtained from each volunteer taking part in this

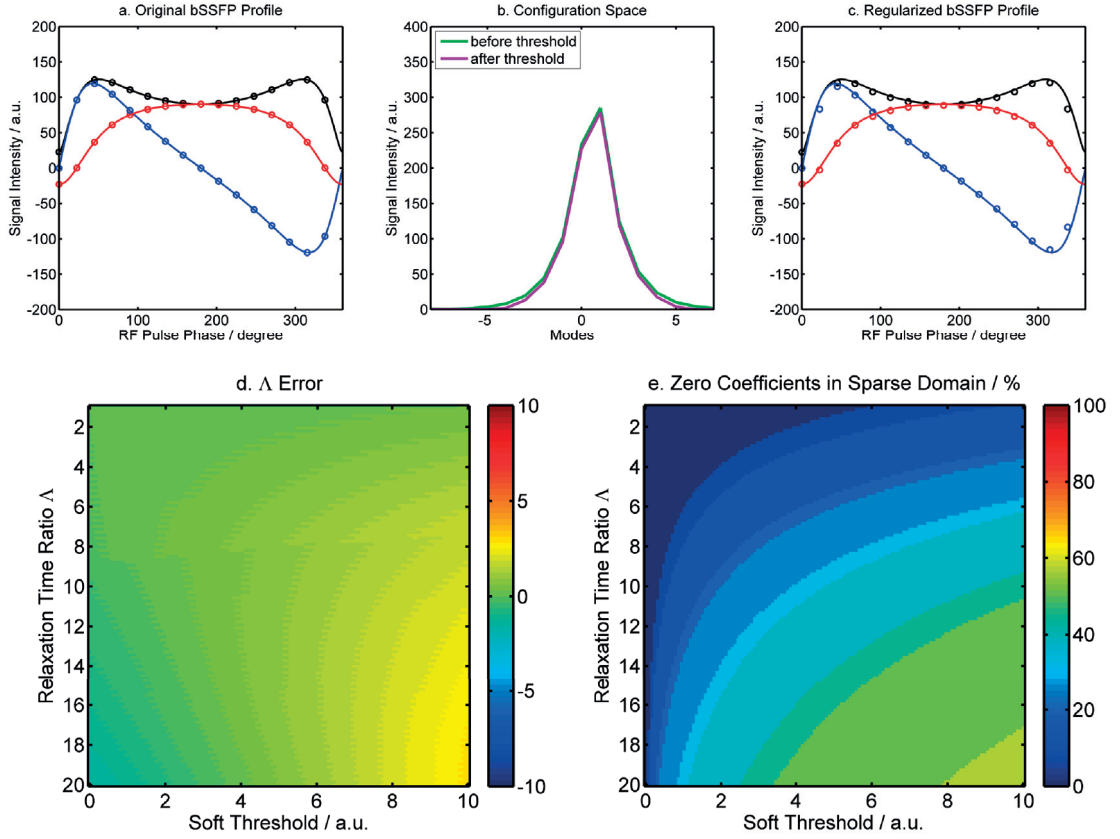


Figure 6.3: A simulated complex bSSFP profile with $\Lambda = 10.4$ (continuous line, top) with black indicating the magnitude, blue real- and red imaginary-values and circles the sampled phase-cycles. Its discretized signal was Fourier-transformed into configuration space (3b, green). The configuration space has six zero coefficients (37.5%) after applying a low soft-threshold of 6 (3b, purple). The inverse Fourier transform of the signal after applying the threshold diverges from the original (3c, circles) causing an overestimation in the dictionary fitting ($\Lambda^* = 11.6$). (c) Bias of Λ and (d) amount of zero coefficients for all combinations of Λ and soft-thresholds.

study.

Similar to every other compressed sensing regularization, the zeroing of coefficients in the sparse domain can introduce undesirable reconstruction artifacts that subsequently could bias the estimation of Λ . To study the impact of the regularization, a set of complex bSSFP profiles were simulated, with Λ ranging from 1 to 20; $\Phi = 180^\circ$ and $M_0 = 1$. To deliberately introduce regularization artifacts, all the profiles were Fourier-transformed into configuration space, and a range of soft thresholds (1–8) were applied to achieve zero coefficients, that is, sparsity. Subsequently, the signal was inverse Fourier-transformed back to a bSSFP profile and compared to the simulated ground truth. Subsequently, the previously described dictionary fitting was performed on the obtained profiles to evaluate the impact of the introduced regularization artifacts on the estimation of Λ .

Dictionary-based fitting algorithms became more popular in recent years and proved to be powerful tools, for example, in MR fingerprinting applications [23]. Applying it to a bSSFP sequence only requires a simple adaption of the method. However, the sequence design and signal properties are different and the dictionary fitting may behave in another manner, requiring a thorough analysis to avoid systematic biases and ensure accuracy. To that end, an additional experiment was performed, simulating bSSFP profiles with different relaxation time ratios Λ (1-30) for a fixed flip angle (15°) and fixed local phase offset ($\Phi = 180^\circ$) in the presence of white Gaussian noise at different SNR levels (5–100). The dictionary fitting was then used to estimate the relaxation time ratio, and its deviation from the known truth was calculated. This was repeated 128 times to calculate two fitting quality measures: the mean error and the standard deviation (SD) of the error. A similar experiment was then performed using a range of local phase offsets ($0 - 360^\circ$) and a fixed relaxation time ratio ($\Lambda = 10$).

Phantom imaging was performed on a manganese doped spherical phantom composed of 0.125 mM $MnCl_2$ dissolved in water (with T_1/T_2 ratio of 870 ms/70 ms ≈ 12 , similar to human tissues, measured by gold standard T_1 and T_2 relaxation methods) and about 14 cm in diameter. TrueCISS imaging was performed with 16 phase cycles using an eight fold undersampled k-space in combination with a TR/echo time (TE) of 4.48 ms/2.24 ms, a flip angle α of 15° , a resolution of $1 \times 1 \times 1 \text{ mm}^3$ ($192 \times 192 \times 192$ matrix size), a bandwidth of 501 Hz/px, and RF phase increments ϕ_j according to Equation 6.1, yielding an overall scan time of 5:56 minutes. During the acquisition, a linear frequency offset gradient was applied over the whole field of view to induce multiple banding artifacts within the image. A reference CISS image was acquired with the same resolution, bandwidth, and flip angle using an unmodified product sequence with a TR/TE of 7.13 ms/3.31 ms, yielding a comparable total acquisition time of 5:31 minutes.

One in vivo 3D human whole-brain trueCISS dataset was acquired using the same prototype sequence, with 16 phase cycles and eight fold undersampling in combination with a TR/TE of 6.36 ms/3.18 ms, $\alpha = 15^\circ$, $1 \times 1 \times 1 \text{ mm}^3$ resolution ($256 \times 256 \times 176$ matrix size), bandwidth 250 Hz/px, and RF phase increments ϕ_j following Equation 6.1, resulting in a total scan time of about 10:15 minutes. For comparison, a 3D CISS image dataset also was acquired with the same resolution but having a TR/TE of 7.87 ms/3.59 ms, $\alpha = 50^\circ$, and bandwidth 337 Hz/px, completed within 9:04 min. Contrary to the phantom experiment, different sequence parameters were used for the CISS acquisition because parameters as used for trueCISS would have led to significant banding residuals and would not be used in clinical routine.

6.3 Results

To demonstrate the effects of regularization artifacts, the 16 phase-cycling samples of an exemplary simulated complex bSSFP profile ($\Lambda = 10.4$) are shown in Figure 6.3a. Its shape in the configuration space is shown in Figure 6.3b (green). After a moderate soft threshold ($=6$) was applied (Figure 6.3b, purple), 37.5% of the coefficients in the configuration space are zero, indicating that the Fourier transform achieves a sufficient sparsity. The regularization artifacts

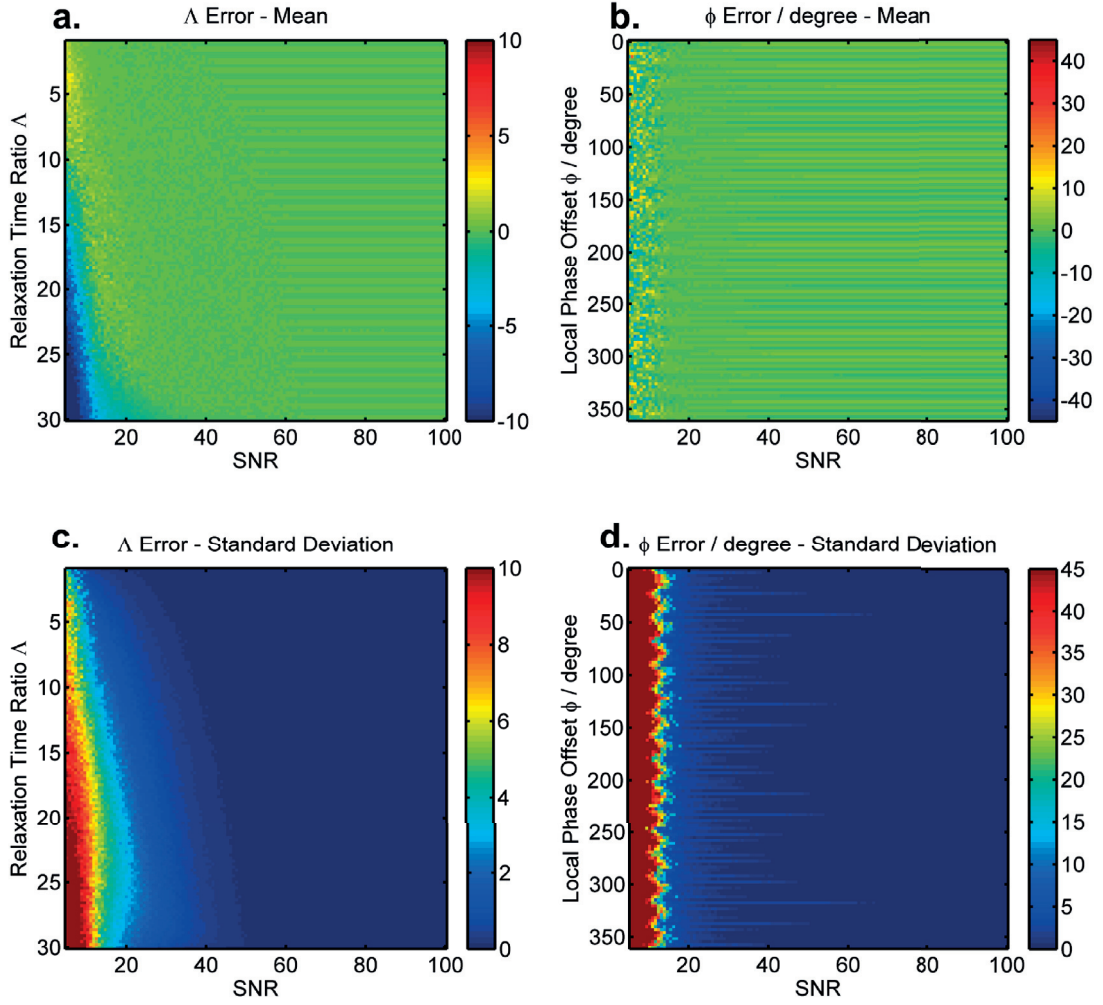


Figure 6.4: (a) Mean error of Λ depending on the SNR with $\Phi = 180^\circ$ and (c) the standard deviation of the Λ error. (b) Mean error of Φ depending on the SNR with $\Lambda = 10$ and (c) the standard deviation of the Φ error.

induced by the soft threshold only have a small impact on the shape of the bSSFP profile (Figure 6.3c, circles) and lead to a slight overestimation ($\Lambda^* = 11.6$). The obtained sparsity and introduced error in Λ for the simulated range of Λ and soft thresholds are shown in Figure 6.3d,e. To summarize these results, with higher Λ , more zero coefficients can be achieved after Fourier transformation and soft-thresholding due to its higher sparsity. However, the dictionary fitting overestimates Λ with stronger regularization artifacts, especially when Λ is high.

The mean and SD of the error in the dictionary fitting are shown in Figure 6.4. The simulations with a high SNR (>30) show a very low bias and a good accuracy of the parameter estimation. A small step-wise error is visible due to the restriction of the dictionary fitting to a discrete set of solutions. The estimation of lower Λ appears to be more accurate than for higher values,

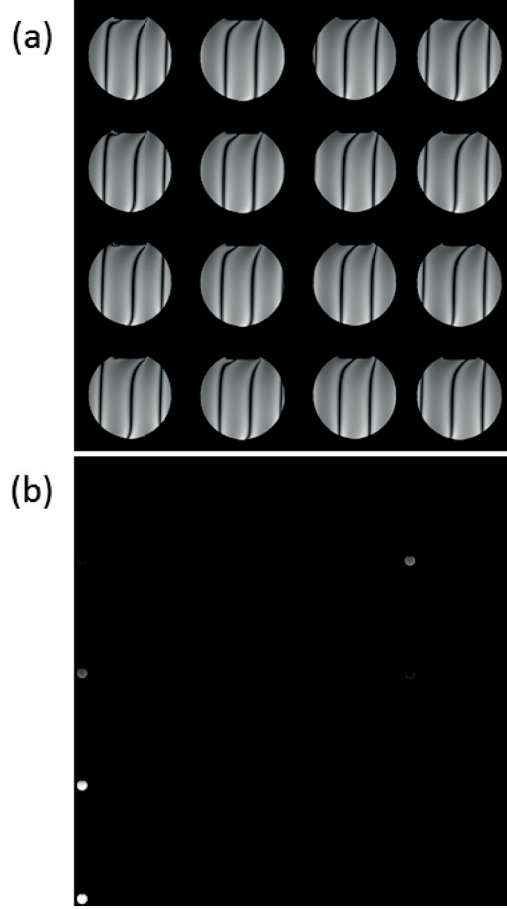


Figure 6.5: (a) Illustrative images from a set of $N = 16$ bSSFP scans with different RF phase increments, and (b) corresponding sparse representation by subsequently applying a Fourier transformation along the phase cycles and a spatial wavelet-transformation.

which could be due to the more distinctive shape of a low Λ at low flip angle (15°), allowing for good estimates even for a bad SNR (≈ 10). On the other hand, the accuracy of the Φ error is rather independent from the actual Φ value and remains high without bias until it drops drastically (e.g., at SNR=15 with $\Lambda = 10$).

Illustrative axial images from the 16 highly undersampled phase-cycled bSSFP manganese-doped spherical phantom datasets (with RF phase increments following 6:1) are shown in Figure 6.5a after the proposed compressed sensing reconstruction. Note that a linear frequency gradient was applied from left to right to artificially induce banding artifacts. The required sparsity after the proposed wavelet and Fourier transformation becomes evident by the low number of non-zeros coefficients present in the transformed image (Figure 6.5b).

Corresponding trueCISS parameter maps are given in Figure 6.6a–c in axial orientation. Generally, because transmit field inhomogeneities (B_1) are not accounted for, Λ maps reflect the expected B_1 -related smooth variation from the centre toward the rim of the phantom. Resid-

ual small-scale variations, however, which appear to be rather related to the superimposed B_0 field inhomogeneity, can be perceived on both Λ and M_0 parameter maps but become less intense in the final trueCISS image (Figure 6.6d) and have a magnitude smaller than truncation artifacts, as can be seen in the intensity profile. For reference, a 15° CISS image is shown in Figure 6.6e using an unmodified product sequence. Banding-related residual signal modulations become accentuated in the conventional CISS image due to the low flip angle scan.

Exemplary parameter maps estimated from the high resolution in vivo 3D whole-brain true-CISS acquisition are given in Figure 6.7 in sagittal orientation. As can be expected and as reflected by the field map (Figure 6.7c), severe field inhomogeneities toward the neck, cavities, and outer parts of the brain tissue emanate due to the rather long TR used for the bSSFP acquisition at 3T. Overall, the parametric maps of M_0 and Λ exhibit the expected contrast between white and grey matter resulting from differences in proton densities and relaxation times. As for the phantom, some residual B_1 bias can be perceived in Λ ; however, it appears less pronounced.

TrueCISS image reconstructions with flip angles of 15° (native) and 50° (synthetic), as well as a maxCISS image reconstruction (see also Equation 6.4), are shown in Figure 6.8. For comparison, a standard 50° flip angle CISS image also is shown (Figure 6.8d). Compared to the standard CISS sequence, all trueCISS images achieve a greater suppression of banding artifacts, most noticeable in regions suffering from strong field inhomogeneities, such as the region superior to the nasal cavity. The trueCISS image with a native flip angle of 15° (Figure 6.8a) provides a good contrast between white and grey matter, whereas the maxCISS with the optimal flip angle in each voxel (Figure 6.8b) provides the highest signal intensities throughout and a better contrast in deep grey matter structures. The synthetic trueCISS image derived for a flip angle of 50° (Figure 6.8c) provides a similar contrast as the conventional CISS sequence (Figure 6.8d) but suffers from slight blurring, as can be seen in the thalamus region. Furthermore, in comparison to the conventional CISS, small vessels are not visible.

6.4 Discussion

The results demonstrate that banding-free images can be reconstructed from a set of highly undersampled phase cycled bSSFP acquisitions using compressed sensing in combination with a dictionary-based estimation of the intrinsic bSSFP signal-dominating parameters. This combination allows for better image quality, with overall scan times comparable to conventional 3D CISS imaging.

TrueCISS imaging provides the true, that is, on-resonant, bSSFP signal amplitude, thus facilitating the use of quantitative imaging methods that rely on accurate bSSFP signal estimation. Moreover, high flip angle trueCISS images can be synthesized from low flip angle bSSFP data to enhance its prominent fluid–tissue contrast. Generally, low flip angle bSSFP imaging is advantageous because it not only mitigates MT effects [94] but also allows scanning with

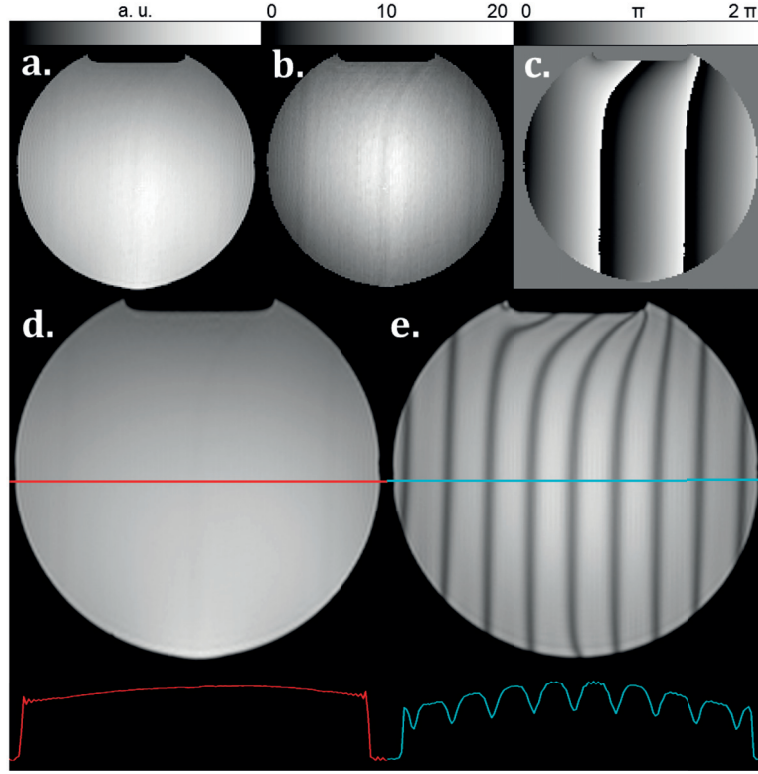


Figure 6.6: Parametric maps obtained from a dictionary based fitting of phase-cycled bSSFP datasets and correspond to the initial magnetization M_0 (a), the relaxation time ratio Λ (b) and the local phase offset $\Delta\Phi$ (c). Phantom images reconstructed based on the proposed TrueCISS method, with an intensity profile in red, (d) and from a conventional CISS acquisition, with an intensity profile in cyan (e). Both acquisitions were performed with a flip-angle of 15° and a linear frequency offset gradient (left to right) to generate banding artifacts.

low SAR. Consequently, synthetic trueCISS imaging may represent a valuable alternative if SAR-intensive sequences such as CISS and SPACE or conventional bSSFP protocols fail due to safety constraints. This is especially interesting at ultrahigh field strengths in which the application of SAR in-tense sequences is challenging.

The synthetic contrast, as provided by maxCISS, reflects the maximum bSSFP signal intensities in each voxel for the underlying tissue properties (i.e., T_1/T_2). This contrast not only is impossible to acquire in practice but also renders the maxCISS signal independent of the transmit field inhomogeneity (B_1^+). Thus, the proposed maxCISS image contrast might be of particular interest in clinical applications in which a strong B_1 variation is expected or the images contain many different types of tissues and the tuning for a reasonable flip angle is challenging (e.g., knee, abdomen).

The noise behaviour in the image should be considered when generating synthetic contrasts from the parameter maps that divert from the original sequence protocol (e.g., different flip angle). The synthesization may result in heterogeneous noise amplifications or reduc-

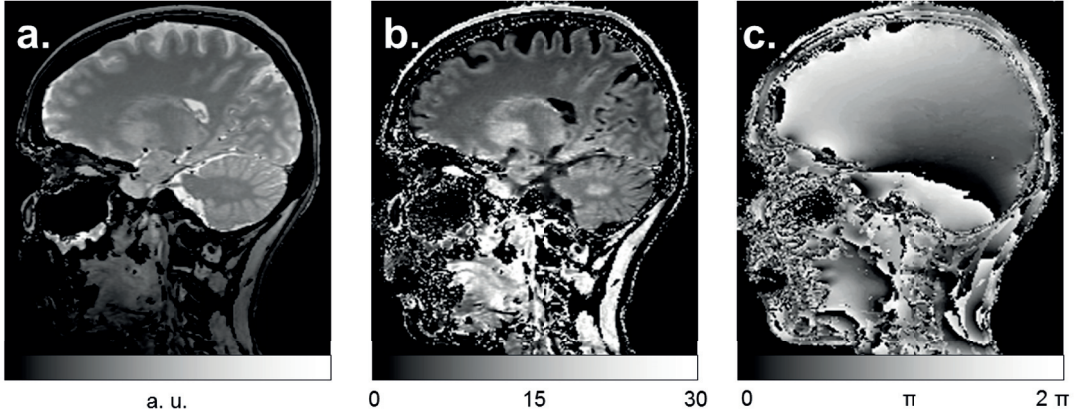


Figure 6.7: The parametric maps that were obtained by the dictionary based fitting and correspond to the initial magnetization M_0 (a), the relaxation time ratio Λ (b) and the local phase offset $\Delta\Phi$ (c).

tion because the signal intensity scales non-linearly, depending on the underlying contrast parameters (i.e., M_0 , T_1/T_2 , and flip angle).

The steady-state magnetization M_0 image should be proton density-weighted and therefore exhibit poor contrast between white and grey matter. However, we observe a greater contrast than expected, which may be due to an asymmetry of the bSSFP profile in some locations not accounted for in the signal model. These asymmetries were more closely studied in [95] and also may be the reason for the subtle B_0 effects in the phantom experiment. Other physical effects, which are neglected in the model, contribute to the estimate of M_0 as well. Therefore, we consider M_0 not a quantitative estimation of proton density; rather, it serves as a parameter used to accommodate multiple physical effects.

A limitation of the proposed method arises from the spatial regularization used in the compressed sensing reconstruction and the partial Fourier sampling of k-space that introduce blurring in the resulting images. Furthermore, simulations demonstrate that the sparsity that can be achieved with the Fourier transform across phase cycles greatly depends on T_1/T_2 and flip angle because lower T_1/T_2 and lower flip angles result in sharper transitions in the bSSFP profile. Additionally, the sparsity will depend on the amount of acquired phase cycles because data tend to become sparser as the dimensionality of the observation matrix increases. These limitations of the regularization should be taken into account when optimizing sequence protocols because they may prohibit high acceleration factors and cause regularization artifacts, resulting in an overestimation of Λ during the dictionary fitting. Generally, more advanced regularization techniques, such as joint total variation along the phase cycles [96], could be used to further mitigate residual blurring. Another possible method to reduce blurring is to acquire fewer phase cycles and use the gained time to sample more k-space samples for each phase cycle. However, this may lead to an ill-posed fitting of the tissue parameters after the compressed sensing reconstruction.

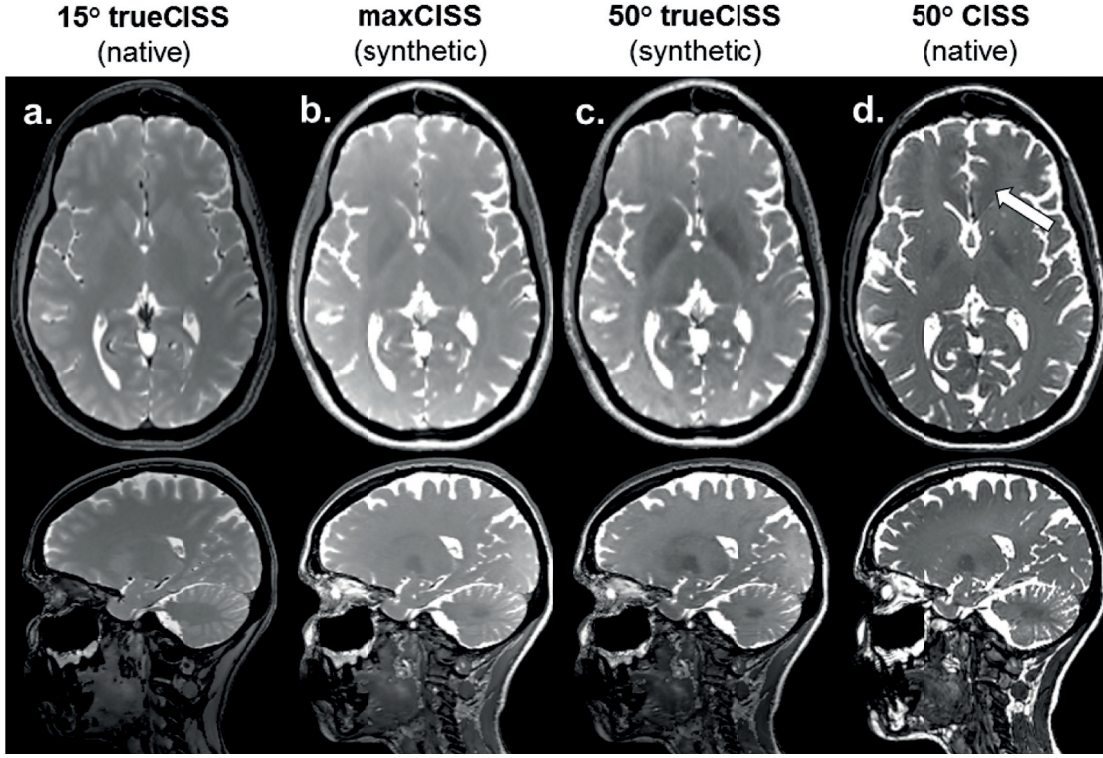


Figure 6.8: Axial and sagittal slices of trueCISS images with the native flip-angle of 15° (a), maxCISS with the optimal flip-angle (b) and a flip-angle of 50° (c) compared to the conventional CISS image (d). Note that the subject slightly moved between the trueCISS and CISS acquisition. The arrow points to residual banding artifacts that can be seen on the CISS image.

Another source of error in the reconstruction is the accuracy of the coil sensitivities used in the compressed sensing algorithm. The accuracy of the coil-sensitivity estimate can be flawed if the field of view of the acquisition is too small and folding artifacts appear. This is a common problem in compressed sensing reconstructions and thus affects the quality of the resulting trueCISS images.

Moreover, the model-fitting procedure might introduce errors in the obtained images. Its overall accuracy depends on the ability to correctly estimate the bSSFP signal parameters in each voxel. Any non-modelled difference due to hardware-related inconsistencies or physiological processes will result in biased estimates of M_0 , Λ , and Φ , which are visible as a sub-optimal banding artifact removal in the final images. For example, severe intra-voxel susceptibility gradients could lead to a local transition of balanced to unbalanced, or even to a completely dephased SSFP signal at the echo-time. A decrease of the voxel size might be considered to mitigate those problems. Another more general problem is that the fitting procedure might become more sensitive with lower SNR. A correct fitting is therefore only guaranteed with sufficient resolution and the use of multiple receiver coils.

The methods proposed in this work address two different aspects: First, lengthy acquisition

times are reduced by undersampling and a compressed sensing reconstruction using the Fourier transformed bSSFP profile as sparse domain. Second, banding artifacts that become even more severe with low flip angles are removed by using a dictionary-fitting algorithm and synthetic contrasts.

In conclusion, a compressed sensing reconstruction of a series of highly undersampled phase-cycled bSSFP images in combination with a dictionary-based fitting algorithm can be used to reconstruct banding artifact-free genuine bSSFP images, which we termed trueCISS. Moreover, synthetic bSSFP contrast images can be derived from the intrinsic parameter estimates, for example, the flip angle independent maxCISS signal, or enhanced tissue–fluid contrast images achieved at high flip angles, which are not possible to acquire directly due to either physical or safety constraints. From this, trueCISS might help to extend bSSFP imaging to a wider range of clinical applications.

7 Conclusion

7.1 Achieved Results

This work has contributed in multiple ways to the field of model-based MRI acquisitions and reconstructions, especially with regards to quantitative MRI. A part from scientific curiosity and the will to explore the presented ideas, the main goal was to aim for clinical applicability and relevance of the developed methods.

A fast quantitative mapping approach, GRAPPATINI, was developed, that combines the advantages of parallel imaging in k-space (GRAPPA) and a model-based reconstruction (MARTINI). With this new method, it is possible to acquire whole-brain T_2 maps in less than two minutes acquisition time. This is ten times faster than an acquisition without undersampling. Using a mono-exponential decay as signal model, the typical 20% overestimation of the T_2 values was observed. Nonetheless, T_2 values were reproducible between scan and rescan (< 0.4 ms SD) and across subjects (< 4 ms SD, notably including physiological differences), although stimulated echoes were not accounted for in the signal model. Furthermore, imaging protocols were developed and optimized for several bodyparts to enable a wide range of clinical or clinical research applications of this technique.

GRAPPATINI confirmed the validity of the concept to apply GRAPPA kernels prior to a model-based reconstruction. This led to the idea to combine model-based reconstructions with SMS, as SMS reconstructions also employ GRAPPA kernels to disentangle the signal from different slices. To that end, a conventional CPMG sequence was modified, yielding a new sequence design that used classical multiband pulses for excitation and PINS pulses for refocusing in order to acquire the undersampled k-space. Five simultaneously acquired slices in combination with five-fold undersampling yielded a much faster acquisition (2:06 min) in comparison to the conventional CPMG acquisition (52:30 min) while conserving the desired quantitative information. A major advantage of using PINS pulses is their low power deposition, enabling imaging protocols that are not possible with a conventional CPMG sequence, due to SAR limitations. A split-slice GRAPPA algorithm and a newly developed model-based reconstruction (SAFT) were used to reconstruct the data. Contrary to MARTINI, SAFT used numerical

simulations rather than an analytical model to recover missing k-space lines. This provided the advantage of being able to account for stimulated echoes by incorporating slice profiles while simultaneously estimating B1 maps. The new approach exhibited similar reproducibility as GRAPPATINI (< 0.45 ms scan-rescan SD, < 4.5 ms across subject SD), but with the addition that T_2 values were no longer overestimated and agreed with reference values in phantom experiments.

The difference in accuracy between models that account for stimulated echoes versus models that only assume a mono-exponential decay demonstrated the dependency of model-based reconstructions on the underlying signal model. This dependency also applies to a more recent and widely discussed model-based approach, magnetic resonance fingerprinting. In the studies described in this thesis, it was discovered that the estimation of T_1 and T_2 may be biased by magnetization transfer effect based on the observation from in-vivo experiments that this bias changes depending on the used pulse bandwidth. To this end, a simplified numerical model was proposed, which accounts for magnetization transfer; resulting maps showed more accurate T_1 and T_2 estimations and mitigated the undesired pulse bandwidth dependency.

In a last study, a model-based approach was used to remove banding artifacts in bSSFP acquisitions, which constitute a major limitation of this family of MRI sequences. To that end, an analytical signal model of a phase-cycled bSSFP profile was used to estimate two tissue properties, equilibrium magnetization and relaxation time ratio, together with the local phase offset caused by B_1 inhomogeneity. This facilitated the separation of tissue properties and effects from the experimental condition, allowed to generate synthetic contrasts (trueCISS contrast) without local phase-offset, and thus, without banding artifacts. Since the fitting required more phase cycles than a conventional CISS acquisition, the necessary additional scan time was counterbalanced by an incoherently undersampled acquisition and a compressed sensing reconstruction.

In summary, the main contribution of this work is to propose and study various signal models and to employ them in newly developed reconstruction techniques to accelerate image acquisition or improve imaging quality, especially in the field of quantitative MRI.

7.2 Clinical Impact of this Work

The fast quantitative T_2 imaging approach, GRAPPATINI, was implemented as an online reconstruction on a scanner platform (Siemens) and distributed as a prototype to various collaboration partners worldwide. Today, the prototype is installed on approximately 100 MRI scanners where it is used for research purposes on a daily basis.

In the following paragraphs, initial results from selected pilot studies performed by collaborating scientist using this prototype are briefly discussed.

The prototype was used by Gil et al. to study the impact of fiber orientation on T_2 values [97]. They showed that T_2 values vary depending on the relative orientation of fibres to the main magnetic field. The measured T_2 values were separated in isotropic and anisotropic components. This relaxation information is complementary to diffusion-weighted MR imaging and the authors speculate that this may help to better understand white matter pathology in the future.

The synthetic T_2 -weighted contrasts which can be calculated online in parallel with the GRAPPATINI reconstruction allowed the integration of this technique into clinical research. Since T_2 mapping is common in orthopaedics, especially in knee MRI, clinical collaborators tested the feasibility of this approach in this bodypart. Due to the wide spread of biological T_2 values in knee tissue (compared to brain tissue); multiple fast SE contrasts with different T_2 weighting are usually acquired. Roux et al. showed that these contrasts can be achieved faster acquiring quantitative maps and generating synthetic images with GRAPPATINI [98]. Further work is ongoing, trying to prove the clinical validity of the synthesized contrasts – which will help to integrate GRAPPATINI in other clinical protocols, with the advantage of measuring quantitative information while the classical radiological contrast can be generated “for free”.

Ongoing work by Raudner et al. explores T_2 values in the lumbar and cervical spine based on an optimized GRAPPATINI protocol [99]. The current study focuses on the correlation of T_2 values in the spinal discs with back pain. Future work will aim at using T_2 values to locate the origin of the pain, and may provide crucial information prior to surgery.

Furthermore, the prototype is used in yet unpublished studies, to detect and categorize cancerous tissue in the prostate, comparing results to image guided biopsies (University Hospital Jena, Germany), as well as to build databases for normative T_2 values in the pancreas with the aim to detect diffuse pancreatic lesions (University Hospital Lausanne, Switzerland). Another study is focusing on the brain maturation in neonates and its impact on T_2 values with the goal to early detect abnormal brain maturation (University Hospital Tours, France).

In the future, the prototype should be extended by the PINS-SMS method presented here. The additional acceleration and the possibility to acquire more slices may help to use it in other organs, e.g. in other abdominal regions, where only a short time during end-expiration or during a breath hold is available to acquire a T_2 map. With SMS, it would be possible to cover a bigger FOV in a shorter acquisition time that may be a step towards whole-body T_2 mapping. The low power deposition of the PINS pulses may also allow using the new method at higher field strength.

The proposed model of magnetization transfer in MRF may not have a direct impact in clinics today. However, it may help to raise awareness in the research community to integrate this potential source of error in the employed MRF signal models so that this method yields more accurate and robust mapping results for future integration in clinical protocols.

Finally, the trueCISS method may allow the future use of bSSFP acquisition at ultra-high field,

since it provides banding free images even when small flip angles are used. Doing so, high resolution 3D images are feasible without exceeding SAR limitations. Nguyen et al. already showed first in-vivo trueCISS images at 9.5T field strength without banding artifacts [100]. Furthermore, the method is of interest to mitigate artifacts in orthopaedics where implants can disturb the main magnetic field [101].

7.3 Outlook

A natural continuation of the present work is to further improve the accuracy and reproducibility of the proposed quantitative mapping techniques. Ideally, these efforts and the work of the entire qMRI community lead to consensus on ground truth quantitative reference values – initial efforts are already ongoing as the proposal of a standardized quantitative phantom shows [102]. Other standardized tests and open access data may be one way to move MRI to a fully quantitative imaging modality, where values are independent from the used sequence, imaging protocol, and hardware.

Future development should also focus on moving away from 2D, and towards 3D T_2 mapping, in order to enable acquisitions with higher SNR and isotropic resolutions. Various approaches are already established and could be further explored to achieve this goal, e.g. by using T_2 magnetization preparation and a 3D FLASH image acquisition. Numerical simulations, as proposed in this work, could be used for fitting to avoid biases due to T_1 relaxation and B_1 inhomogeneity. First initial results showed a good accuracy of T_2 values, but still suffer from long acquisition times [103]. 3D T_2 mapping approaches may benefit from model-based reconstruction as well. Alternatively, multiple 2D CPMG acquisitions could be combined in a super resolution reconstruction to achieve high resolution images similar to 3D imaging, with the advantage that already explored signal models could be employed [104].

The work of this thesis only focused on the development and optimization of acquisition and reconstruction techniques. With these techniques fast quantitative mapping is possible; however, the path to a routine use still requires more research and validation studies. For now, the quantitative maps are “just another contrast”, providing comparable information independent from hardware etc., but currently no additional clinical information for the radiologist. The comparability of MRI however enables establishing ranges of normal quantitative values for biological tissues. This has a great potential to help finding subtle pathological tissue alterations that cannot be observed with the naked eye. To that end, it is required to build a database of quantitative maps from healthy volunteers as well as develop statistical tools to compare a newly acquired quantitative map to the database to detect abnormal tissue. A large population-wide database for a wide variety of organs, and automated machine learning tools to detect abnormalities may support the future radiologist on the way towards precision medicine and personalized treatment.

Bibliography

- [1] F Bloch and I I Rabi. Atoms in Variable Magnetic Fields. *Rev. Mod. Phys.*, 17(2-3):237–244, apr 1945.
- [2] E M Purcell, H C Torrey, and R V Pound. Resonance Absorption by Nuclear Magnetic Moments in a Solid. *Phys. Rev.*, 69(1-2):37–38, jan 1946.
- [3] E.L. Hahn. Spin Echoes. *Physical Review*, 80(4):580–594, 1950.
- [4] N. Bloembergen, E. Purcell, and R. Pound. Relaxation Effects in Nuclear Magnetic Resonance Absorption. *Physical Review*, 73(7):679–712, 1948.
- [5] Raymond Damadian. Tumor Detection by Nuclear Magnetic Resonance. *Science*, 171(3976):1151–1153, 1971.
- [6] Raymond Damadian. Apparatus and method for detecting cancer in tissue, 1974.
- [7] M Goldsmith, R Damadian, M Stanford, and M Lipkowitz. NMR in cancer: XVIII. A superconductive NMR magnet for a human sample. *Physiological chemistry and physics*, 9(1):105–108, 1977.
- [8] P C Lauterbur, D M Kramer, W V House, and C N Chen. Zeugmatographic High-Resolution Nuclear Magnetic-Resonance Spectroscopy - Images of Chemical Inhomogeneity Within Macroscopic Objects. *Journal Of The American Chemical Society*, 97:6866–6868, 1975.
- [9] a N Garroway, P K Grannell, and P Mansfield. Image formation in NMR by a selective irradiative process. *Journal of Physics C: Solid State Physics*, 7(24):L457–L462, 1974.
- [10] A Kumar, D Welti, and R R Ernst. Imaging of macroscopic objects by NMR Fourier zeugmatography. *Naturwissenschaften*, 62(1):34, jan 1975.
- [11] Clifford R Jack, Matt A Bernstein, Nick C Fox, Paul Thompson, Gene Alexander, Danielle Harvey, Bret Borowski, Paula J Britson, Jennifer L Whitwell, Chadwick Ward, Anders M Dale, Joel P Felmlee, Jeffrey L Gunter, Derek L G Hill, Ron Killiany, Norbert Schuff, Sabrina Fox-Bosetti, Chen Lin, Colin Studholme, Charles S DeCarli, Gunnar Krueger, Heidi A Ward, Gregory J Metzger, Katherine T Scott, Richard Mallozzi, Daniel Blezek,

Bibliography

- Joshua Levy, Josef P Debbins, Adam S Fleisher, Marilyn Albert, Robert Green, George Bartzokis, Gary Glover, John Mugler, and Michael W Weiner. The Alzheimer's Disease Neuroimaging Initiative (ADNI): MRI methods. *Journal of magnetic resonance imaging: JMRI*, 27(4):685–91, apr 2008.
- [12] Janaka P. Wansapura, Scott K. Holland, R. Scott Dunn, and William S. Ball. NMR relaxation times in the human brain at 3.0 Tesla. *Journal of Magnetic Resonance Imaging*, 9(4):531–538, 1999.
- [13] E Mark Haacke, Robert W Brown, Michael R Thompson, and Ramesh Venkatesan. *Magnetic Resonance Imaging: Physical Principles and Sequence Design*, volume 1st. 1999.
- [14] Tilman J. Sumpf, Martin Uecker, Susann Boretius, and Jens Frahm. Model-based nonlinear inverse reconstruction for T2 mapping using highly undersampled spin-echo MRI. *Journal of Magnetic Resonance Imaging*, 34(2):420–428, 2011.
- [15] Daniel Neumann, Martin Blaimer, Peter M. Jakob, and Felix A. Breuer. Simple recipe for accurate T2 quantification with multi spin-echo acquisitions. *Magnetic Resonance Materials in Physics, Biology and Medicine*, 27(6):567–577, 2014.
- [16] N. N. Lukzen, M. V. Petrova, I. V. Koptug, A. A. Savelov, and R. Z. Sagdeev. The generating functions formalism for the analysis of spin response to the periodic trains of RF pulses. Echo sequences with arbitrary refocusing angles and resonance offsets. *Journal of Magnetic Resonance*, 196(2):164–169, 2009.
- [17] Tilman J. Sumpf, Andreas Petrovic, Martin Uecker, Florian Knoll, and Jens Frahm. Fast T2 mapping with improved accuracy using undersampled spin-echo MRI and model-based reconstructions with a generating function. *IEEE Transactions on Medical Imaging*, 33(12):2213–2222, 2014.
- [18] Noam Ben-Eliezer, Daniel K. Sodickson, and Kai Tobias Block. Rapid and accurate T2 mapping from multi-spin-echo data using bloch-simulation-based reconstruction. *Magnetic Resonance in Medicine*, 73(2):809–817, 2015.
- [19] Ruud B. Van Heeswijk, Davide Piccini, Hélène Feliciano, Roger Hullin, Juerg Schwitter, and Matthias Stuber. Self-navigated isotropic three-dimensional cardiac T2 mapping. *Magnetic Resonance in Medicine*, 73(4):1549–1554, 2015.
- [20] José P. Marques, Tobias Kober, Gunnar Krueger, Wietske van der Zwaag, Pierre François Van de Moortele, and Rolf Gruetter. MP2RAGE, a self bias-field corrected sequence for improved segmentation and T1-mapping at high field. *NeuroImage*, 49(2):1271–1281, 2010.
- [21] Rahel Heule, Carl Ganter, and Oliver Bieri. Triple echo steady-state (TESS) relaxometry. *Magnetic Resonance in Medicine*, 71(1):230–237, 2014.

-
- [22] Sean C L Deoni, Terry M. Peters, and Brian K. Rutt. Determination of Optimal Angles for Variable Nutation Proton Magnetic Spin-Lattice, T1, and Spin-Spin, T2, Relaxation Times Measurement. *Magnetic Resonance in Medicine*, 51(1):194–199, 2004.
- [23] Dan Ma, Vikas Gulani, Nicole Seiberlich, Kecheng Liu, Jeffrey L Sunshine, Jeffrey L Duerk, and Mark A Griswold. Magnetic resonance fingerprinting. (1). *Nature*, 495(7440):187–192, 2013.
- [24] J. Hennig, A. Nauerth, and H. Friedburg. RARE imaging: A fast imaging method for clinical MR. *Magnetic Resonance in Medicine*, 3(6):823–833, 1986.
- [25] K Oshio and D a Feinberg. GRASE (Gradient- and spin-echo) imaging: a novel fast MRI technique. *Magnetic resonance in medicine : official journal of the Society of Magnetic Resonance in Medicine / Society of Magnetic Resonance in Medicine*, 20:344–349, 1991.
- [26] Mark A. Griswold, Peter M. Jakob, Robin M. Heidemann, Mathias Nittka, Vladimir Jellus, Jianmin Wang, Berthold Kiefer, and Axel Haase. Generalized Autocalibrating Partially Parallel Acquisitions (GRAPPA). *Magnetic Resonance in Medicine*, 47(6):1202–1210, 2002.
- [27] Klaas P. Pruessmann, Markus Weiger, Markus B. Scheidegger, and Peter Boesiger. SENSE: Sensitivity encoding for fast MRI. *Magnetic Resonance in Medicine*, 42(5):952–962, 1999.
- [28] William W. Hager and Hongchao Zhang. A New Conjugate Gradient Method with Guaranteed Descent and an Efficient Line Search. *SIAM J. Opt.*, 16(1):170–192, 2005.
- [29] D L Donoho. Compressed sensing. *IEEE Transactions on Information Theory*, 52(4):1289–1306, 2006.
- [30] Michael Lustig, David Donoho, and John M. Pauly. Sparse MRI: The application of compressed sensing for rapid MR imaging. *Magnetic Resonance in Medicine*, 58(6):1182–1195, 2007.
- [31] Julia V. Velikina, Andrew L. Alexander, and Alexey Samsonov. Accelerating MR parameter mapping using sparsity-promoting regularization in parametric dimension. *Magnetic Resonance in Medicine*, 70(5):1263–1273, 2013.
- [32] Mariya Doneva, Peter Börnert, Holger Eggers, Christian Stehning, Julien S  n  gas, and Alfred Mertins. Compressed sensing reconstruction for magnetic resonance parameter mapping. *Magnetic Resonance in Medicine*, 64(4):1114–1120, 2010.
- [33] Kai Tobias Block, Martin Uecker, and Jens Frahm. Model-based iterative reconstruction for radial fast spin-echo MRI. *IEEE Transactions on Medical Imaging*, 28(11):1759–1769, 2009.
- [34] Xiaoqing Wang, Volkert Roeloffs, Jakob Klosowski, Zhengguo Tan, Dirk Voit, Martin Uecker, and Jens Frahm. Model-based T1 mapping with sparsity constraints using single-shot inversion-recovery radial FLASH, 2017.

Bibliography

- [35] Johannes Tran-Gia, Tobias Wech, Thorsten Bley, and Herbert Köstler. Model-based acceleration of Look-Locker T1 mapping. *PLoS ONE*, 10(4), 2015.
- [36] David J. Larkman, Joseph V. Hajnal, Amy H. Herlihy, Glyn A. Coutts, Ian R. Young, and Gsta Ehnholm. Use of multicoil arrays for separation of signal from multiple slices simultaneously excited. *Journal of Magnetic Resonance Imaging*, 13(2):313–317, 2001.
- [37] David G. Norris, Peter J. Koopmans, Rasim Boyacioglu, and Markus Barth. Power independent of number of slices (PINS) radiofrequency pulses for low-power simultaneous multislice excitation. *Magnetic Resonance in Medicine*, 66(5):1234–1240, 2011.
- [38] Stephen F. Cauley, Jonathan R. Polimeni, Himanshu Bhat, Lawrence L. Wald, and Kawin Setsompop. Interslice leakage artifact reduction technique for simultaneous multislice acquisitions. *Magnetic Resonance in Medicine*, 72(1):93–102, 2014.
- [39] Felix A. Breuer, Martin Blaimer, Robin M. Heidemann, Matthias F. Mueller, Mark A. Griswold, and Peter M. Jakob. Controlled aliasing in parallel imaging results in higher acceleration (CAIPIRINHA) for multi-slice imaging. *Magnetic Resonance in Medicine*, 53(3):684–691, 2005.
- [40] Kawin Setsompop, Borjan A. Gagoski, Jonathan R. Polimeni, Thomas Witzel, Van J. Wedeen, and Lawrence L. Wald. Blipped-controlled aliasing in parallel imaging for simultaneous multislice echo planar imaging with reduced g-factor penalty. *Magnetic Resonance in Medicine*, 67(5):1210–1224, 2012.
- [41] Sean C L Deoni. Quantitative relaxometry of the brain. *Topics in magnetic resonance imaging : TMRI*, 21(2):101–113, 2010.
- [42] Hai Ling Margaret Cheng, Nikola Stikov, Nilesh R. Ghugre, and Graham A. Wright. Practical medical applications of quantitative MR relaxometry, 2012.
- [43] H. Y. Carr and E. M. Purcell. Effects of diffusion on free precession in nuclear magnetic resonance experiments. *Physical Review*, 94(3):630–638, 1954.
- [44] Martin Uecker, Thorsten Hohage, Kai Tobias Block, and Jens Frahm. Image reconstruction by regularized nonlinear inversion - Joint estimation of coil sensitivities and image content. *Magnetic Resonance in Medicine*, 60(3):674–682, 2008.
- [45] Martin Uecker, Peng Lai, Mark J. Murphy, Patrick Virtue, Michael Elad, John M. Pauly, Shreyas S. Vasanawala, and Michael Lustig. ESPIRiT - An eigenvalue approach to autocalibrating parallel MRI: Where SENSE meets GRAPPA. *Magnetic Resonance in Medicine*, 71(3):990–1001, 2014.
- [46] Felix A. Breuer, Stephan A R Kannengiesser, Martin Blaimer, Nicole Seiberlich, Peter M. Jakob, and Mark A. Griswold. General formulation for quantitative G-factor calculation in GRAPPA reconstructions. *Magnetic Resonance in Medicine*, 62(3):739–746, 2009.

-
- [47] Martijn A Cloos, Florian Knoll, Tiejun Zhao, K Block, Mary Bruno, CG Wiggins, and DK Sodickson. Multiparametric imaging with heterogeneous radiofrequency fields. *Nature Communication*, in press:1–10, 2016.
- [48] Feng Huang, Yunmei Chen, Wotao Yin, Wei Lin, Xiaojing Ye, Weihong Guo, and Arne Reykowski. A rapid and robust numerical algorithm for sensitivity encoding with sparsity constraints: Self-feeding sparse SENSE. *Magnetic Resonance in Medicine*, 64(4):1078–1088, 2010.
- [49] Juergen Hennig, Matthias Weigel, and Klaus Scheffler. Calculation of Flip Angles for Echo Trains with Predefined Amplitudes with the Extended Phase Graph (EPG)-Algorithm: Principles and Applications to Hyperecho and TRAPS Sequences. *Magnetic Resonance in Medicine*, 51(1):68–80, 2004.
- [50] Matthias Weigel. Extended phase graphs: Dephasing, RF pulses, and echoes - Pure and simple, 2015.
- [51] Cornelius Eichner, Lawrence L. Wald, and Kawin Setsompop. A low power radiofrequency pulse for simultaneous multislice excitation and refocusing. *Magnetic Resonance in Medicine*, 72(4):949–958, 2014.
- [52] Borjan A. Gagoski, Berkin Bilgic, Cornelius Eichner, Himanshu Bhat, P. Ellen Grant, Lawrence L. Wald, and Kawin Setsompop. RARE/Turbo Spin Echo imaging with Simultaneous MultiSlice Wave-CAIPI. *Magnetic Resonance in Medicine*, 73(3):929–938, 2015.
- [53] D. C. Look and D. R. Locker. Time saving in measurement of NMR and EPR relaxation times. *Review of Scientific Instruments*, 41(2):250–251, 1970.
- [54] I L Pykett, B R Rosen, F S Buonanno, and T J Brady. Measurement of spin-lattice relaxation times in nuclear magnetic resonance imaging. *Physics in medicine and biology*, 28:723–729, 1983.
- [55] S. Meiboom and D. Gill. Modified spin-echo method for measuring nuclear relaxation times. *Review of Scientific Instruments*, 29(8):688–691, 1958.
- [56] Tao Zhang, John M. Pauly, and Ives R. Levesque. Accelerating parameter mapping with a locally low rank constraint. *Magnetic Resonance in Medicine*, 73(2):655–661, 2015.
- [57] Kyunghyun Sung, Bruce L. Daniel, and Brian A. Hargreaves. Transmit B₁ + field inhomogeneity and T₁ estimation errors in breast DCE-MRI at 3 tesla. *Journal of Magnetic Resonance Imaging*, 38(2):454–459, 2013.
- [58] Samuel A Hurley, Vasily L Yarnykh, Kevin M Johnson, Aaron S Field, Andrew L Alexander, and Alexey A Samsonov. Simultaneous variable flip angle-actual flip angle imaging method for improved accuracy and precision of three-dimensional T₁ and B₁ measurements. *MAGNETIC RESONANCE IN MEDICINE*, 68(1):54–64, 2012.

Bibliography

- [59] Jing Zhang, Shannon H. Kolind, Cornelia Laule, and Alex L. MacKay. How does magnetization transfer influence mcDESPOT results? *Magnetic Resonance in Medicine*, 74(5):1327–1335, 2015.
- [60] Klaus Schmierer, Francesco Scaravilli, Daniel R. Altmann, Gareth J. Barker, and David H. Miller. Magnetization transfer ratio and myelin in postmortem multiple sclerosis brain. *Annals of Neurology*, 56(3):407–415, 2004.
- [61] Irene M. Vavasour, Kenneth P. Whittall, Alex L. MacKay, David K B Li, Galina Vorobeychik, and Donald W. Paty. A comparison between magnetization transfer ratios and myelin water percentages in normals and multiple sclerosis patients. *Magnetic Resonance in Medicine*, 40(5):763–768, 1998.
- [62] Debra et al. McGivney. A Bayesian Approach to the Partial Volume Problem in Magnetic Resonance Fingerprinting. In *Proc. Intl. Soc. Mag. Reson. Med. Vol. 23., Toronto, Canada*, 2015.
- [63] Sunli et al. Tang. Multi-Compartment MR Fingerprinting Via Reweighted-L1-Norm Regularization. In *Proc. Intl. Soc. Mag. Reson. Med. Vol. 25., Honolulu, USA*, 2017.
- [64] R. M. Henkelman, G. J. Stanisz, and S. J. Graham. Magnetization transfer in MRI: A review, 2001.
- [65] C Morrison, G Stanisz, and R M Henkelman. Modeling Magnetization Transfer for biological-like systems using a semi-solid pool with a super-lorentzian lineshape and dipolar reservoir. *J. Magn. Reson., Series B*, 108(2):103–113, 1995.
- [66] Greg J. Stanisz, A. Kecojevic, M. J. Bronskill, and R. M. Henkelman. Characterizing white matter with magnetization transfer and T2. *Magnetic Resonance in Medicine*, 42(6):1128–1136, 1999.
- [67] M Gloor, Klaus Scheffler, and Oliver Bieri. Quantitative magnetization transfer imaging using balanced SSFP. *Magnetic Resonance in Medicine*, 60(3):691–700, 2008.
- [68] Hunter R. Underhill, Chun Yuan, and Vasily L. Yarnykh. Direct quantitative comparison between cross-relaxation imaging and diffusion tensor imaging of the human brain at 3.0 T. *NeuroImage*, 47(4):1568–1578, 2009.
- [69] Jorge Zavala Bojorquez, Stéphanie Bricq, Clement Acquitter, François Brunotte, Paul M. Walker, and Alain Lalande. What are normal relaxation times of tissues at 3 T?, 2017.
- [70] Giles E. Santyr. Magnetization transfer effects in multislice MR imaging. *Magnetic Resonance Imaging*, 11(4):521–532, 1993.
- [71] H Carr. Steady-State Free Precession in Nuclear Magnetic Resonance. *Physical Review*, 112(5):1693–1701, 1958.

-
- [72] Klaus Scheffler and Stefan Lehnhardt. Principles and applications of balanced SSFP techniques. *European Radiology*, 13(11):2409–2418, 2003.
- [73] J. W. Casselman, R. Kuhweide, M. Deimling, W. Ampe, I. Dehaene, and L. Meeus. Constructive interference in steady state-3DFT MR imaging of the inner ear and cerebello-pontine angle. *American Journal of Neuroradiology*, 14(1):47–57, 1993.
- [74] Shreyas S. Vasanawala, John M. Pauly, and Dwight G. Nishimura. Linear combination steady-state free precession MRI. *Magnetic Resonance in Medicine*, 43(1):82–90, 2000.
- [75] Neal K. Bangerter, Brian A. Hargreaves, Shreyas S. Vasanawala, John M. Pauly, Garry E. Gold, and Dwight G. Nishimura. Analysis of Multiple-Acquisition SSFP. *Magnetic Resonance in Medicine*, 51(5):1038–1047, 2004.
- [76] Tolga Çukur, Neal K. Bangerter, and Dwight G. Nishimura. Enhanced spectral shaping in steady-state free precession imaging. *Magnetic Resonance in Medicine*, 58(6):1216–1223, 2007.
- [77] Ray Freeman and H. D W Hill. Phase and intensity anomalies in fourier transform NMR. *Journal of Magnetic Resonance (1969)*, 4(3):366–383, 1971.
- [78] Tobias Knopp, Holger Eggers, Hannes Dahnke, Jürgen Prestin, and Julien Senegas. Iterative off-resonance and signal decay estimation and correction for multi-echo MRI. *IEEE Transactions on Medical Imaging*, 28(3):394–404, 2009.
- [79] Marcus Björk, R. Reeve Ingle, Erik Gudmundson, Petre Stoica, Dwight G. Nishimura, and Joëlle K. Barral. Parameter estimation approach to banding artifact reduction in balanced steady-state free precession. *Magnetic resonance in medicine*, 72(3):880–892, 2014.
- [80] Qing San Xiang and Michael N. Hoff. Banding artifact removal for bSSFP imaging with an elliptical signal model. *Magnetic Resonance in Medicine*, 71(3):927–933, 2014.
- [81] Michael N. Hoff, Jalal B. Andre, and Qing San Xiang. Combined geometric and algebraic solutions for removal of bSSFP banding artifacts with performance comparisons. *Magnetic Resonance in Medicine*, 77(2):644–654, 2017.
- [82] M Lustig, J M Santos, D Donoho, and J M Pauly. k-t SPARSE: high frame rate dynamic MRI exploiting spatio-temporal sparsity. *Proceedings of ISMRM, Seattle*, 50(5):2420, 2006.
- [83] Tolga Cukur. Accelerated phase-cycled SSFP imaging with compressed sensing. *IEEE Transactions on Medical Imaging*, 34(1):107–115, 2015.
- [84] Efe Ilicak, Lutfi Kerem Senel, Erdem Biyik, and Tolga Çukur. Profile-encoding reconstruction for multiple-acquisition balanced steady-state free precession imaging, 2016.

Bibliography

- [85] Robert Bridson. Fast Poisson Disk Sampling in Arbitrary Dimensions. *Engineering*, pages 1–1, 2006.
- [86] Herman Tulleken. Poisson disk sampling. *Dev. Mag*, 21:21–25, 2008.
- [87] S. S. Vasanawala, M. J. Murphy, M. T. Alley, P. Lai, K. Keutzer, J. M. Pauly, and M. Lustig. Practical parallel imaging compressed sensing MRI: Summary of two years of experience in accelerating body MRI of pediatric patients. In *Proceedings - International Symposium on Biomedical Imaging*, pages 1039–1043, 2011.
- [88] Daniel Brenner, Rüdiger Stirnberg, Eberhard D. Pracht, and Tony Stöcker. Two-dimensional accelerated MP-RAGE imaging with flexible linear reordering. *Magnetic Resonance Materials in Physics, Biology and Medicine*, 27(5):455–462, 2014.
- [89] Oliver Bieri. An analytical description of balanced steady-state free precession with finite radio-frequency excitation. *Magnetic Resonance in Medicine*, 65(2):422–431, 2011.
- [90] M. Guerquin-Kern, M. Haberlin, K. P. Pruessmann, and M. Unser. A fast wavelet-based reconstruction method for magnetic resonance imaging. *IEEE Transactions on Medical Imaging*, 30(9):1649–1660, 2011.
- [91] Y. Zur, M. L. Wood, and L. J. Neuringer. Motion insensitive, steady state free precession imaging. *Magnetic Resonance in Medicine*, 16(3):444–459, 1990.
- [92] Ir Marinus T Vlaardingerbroek and Ir Jacques A den Boer. Partitioning of the Magnetization into Configurations. In *Magnetic Resonance Imaging*, pages 423–472. Springer, 2003.
- [93] Damien Nguyen and Oliver Bieri. Motion-insensitive rapid configuration relaxometry, 2016.
- [94] Oliver Bieri and K. Scheffler. On the origin of apparent low tissue signals in balanced SSFP. *Magnetic Resonance in Medicine*, 56(5):1067–1074, 2006.
- [95] Karla L. Miller, Stephen M. Smith, and Peter Jezzard. Asymmetries of the balanced SSFP profile. Part II: White matter. *Magnetic Resonance in Medicine*, 63(2):396–406, 2010.
- [96] Itthi Chatnuntaweche, Berkin Bilgic, Adrian Martin, Kawin Setsompop, and Elfar Adalsteinsson. Fast reconstruction for accelerated multi-slice multi-contrast MRI. In *Proceedings - International Symposium on Biomedical Imaging*, volume 2015-July, pages 335–338, 2015.
- [97] Rita Gil, Diana Khabipova, Marcel Zwiers, Tom Hilbert, Tobias Kober, and Jose P Marques. An in vivo study of the orientation-dependent and independent components of transverse relaxation rates in white matter. *NMR in biomedicine*, 29(12):1780–1790, dec 2016.

-
- [98] M Roux, T Hilbert, J-B Ledoux, T Kober, and P Omoumi. Buy one, get two for free: simultaneous knee T2 mapping and morphological analysis on synthetic images using grappatini. *Osteoarthritis and Cartilage*, 24:S301—S302, 2016.
 - [99] R Raudner, T Hilbert, T Kober, V Juras, C Kronnerwetter, D Stelzeneder, and S Trattnig. GRAPPATINI put to use: How MSK applications profit from highly undersampled T2 mapping and synthetic contrasts. In *Proc. Intl. Soc. Mag. Reson. Med.*, 2017.
 - [100] Damien Nguyen, Tom Hilbert, Philipp Ehse, Klaus Scheffler, Jean-Philippe Thiran, Oliver Bieri, and Tobias Kober. On-resonant balanced Steady-State Free Precession imaging at 9.4T. In *Proc. Intl. Soc. Mag. Reson. Med. 24, Singapore*, 2016.
 - [101] Damien Nguyen, Tom Hilbert, Thiran Jean-Philippe, Tobias Kober, and Oliver Bieri. Metal implant imaging using highly undersampled phase-cycled 3D bSSFP. In *Proc. Intl. Soc. Mag. Reson. Med. 24, Singapore*, 2016.
 - [102] S E Russek, M Boss, E F Jackson, D L Jennings, J L Evelhoch, J L Gunter, and A G Sorensen. Characterization of NIST/ISMRM MRI system phantom. In *Proc. Intl. Soc. Mag. Reson. Med*, page 2456, 2012.
 - [103] Emilie Priscille Claire Mussard, Tom Hilbert, Christoph Forman, Reto Meuli, Jean-Philippe Thiran, and Tobias Kober. High-resolution 3D T2 mapping of the Brain Using T2-prepared Cartesian Spiral Phyllotaxis FLASH and Compressed Sensing. In *Intl. Soc. Mag. Reson. Med. 25*, 2017.
 - [104] Tom Hilbert, Jose P Marques, Jean-Philippe Thiran, Reto Meuli, Gunnar Krueger, and Tobias Kober. Model-Based Super-Resolution Reconstruction of T2 Maps. In *Proc. Intl. Soc. Mag. Reson. Med.*, 2017.

Publications

PEER-REVIEWED JOURNAL AND PROCEEDINGS PAPERS

Hilbert T.*, Nguyen D.*, Thiran J. P., Krueger G., Kober T., Bieri O.

True constructive interference in the steady state (trueCISS).

Magnetic Resonance in Medicine. 2017:10.1002/mrm.26836

*equal contributions

Hilbert T., Sumpf T., Weiland E., Frahm J., Thiran J.P., Meuli R., Kober T., Krueger G.

Accelerated T2 Mapping Combining Parallel MRI and Model-Based Reconstruction – GRAPPATINI

Planned submission to Journal of Magnetic Resonance Imaging (JMIR), September 2017

Hilbert T., Kober T., Zhao T., Block K.T., Knoll F., Thiran J.P., Krueger G., Sodickson D.K., Cloos M.

Mitigating the Effect of Magnetization Transfer in Magnetic Resonance Fingerprinting

Submitted to Neuroimage July 2017, Major Revision September 2017

Hilbert T., Schulz J., Bains L.J., Marques J.P., Meuli R., Thiran J.P., Krueger G., Norris D.G., Kober T.

Fast Model-based T2 Mapping using SAR-Reduced Simultaneous-Multi-Slice Excitation

Drafted for submission to Magnetic Resonance in Medicine, September 2017

Waszak M., Falkovskiy P., **Hilbert T.**, Bonnier G., Maréchal B., Meuli R., Gruetter R., Kober T., Krueger G.

Prospective head motion correction using FID-guided on-demand image navigators.

Magnetic Resonance in Medicine. 2017:10.1002/mrm.26364

Gil R., Khabipova D., Zwiers M., **Hilbert T.**, Kober T., Marques JP.

An in vivo study of the orientation-dependent and independent components of transverse relaxation rates in white matter.

NMR Biomed., 29: 1780–1790. doi: 10.1002/nbm.3616

PATENT APPLICATIONS

Hilbert T., Krüger G., Kober T.

Verfahren zur Aufnahme einer Parameterkarte mit einer Magnetresonanzeinrichtung und Magnetresonanzeinrichtung.

DE102014206395.7, Date of filing: April 3, 2014

Hilbert T., Krüger G.

Phase-encode ghosting detection and mitigation in MRI.

EP14194280.5, Date of filing: November 21, 2014

Hilbert T., Kober T., Bieri O., Nguyen D., Krüger G.

Apparatus and method for improving bSSFP in Magnetic Resonance Imaging.

EP15167175.7, Date of filing: May 11, 2015

Hilbert T., Kober T.

Iterative Rekonstruktion von quantitativen MR-Bildern

Date of filing: March 22, 2017

WORK-IN-PROGRESS PACKAGES

Hilbert T., Kober T.

GRAPPATINI – Model-based Accelerated T2 Mapping

Version 1, VB17A/VD13A – Siemens WIP No. 832 – March 2014

Version 2, VD13A/VD13C/VD13D - Siemens WIP No. 899 – September 2014

Version 3, VD13A/VD13D/VE11A - Siemens WIP No. 899B – April 2015

Version 3, VD13D/VE11A/VE11C - Siemens WIP No. 899C – July 2016

ABSTRACTS ACCEPTED FOR INTERNATIONAL CONFERENCES

ISMRM 2012 – Melbourne, Australia

Annual Meeting of the International Society for Magnetic Resonance in Medicine 20

Maréchal B., Kober T., **Hilbert T.**, Ribes D., Chevrey N., Roche A., Thiran J.P., Meuli R., Krueger G.

Automated quality control in MR-based brain morphometry

ISMRM 2014 – Milan, Italy

Annual Meeting of the International Society for Magnetic Resonance in Medicine 22

Hilbert T., Kober T., Sumpf T.J., Tan Z., Frahm J., Falkovskiy P., Meyer H., Bendl R., Thiran J.P., Meuli R., Krueger G.

MARTINI and GRAPPA - When Speed is Taste

ISMRM 2015 – Toronto, Canada

Annual Meeting of the International Society for Magnetic Resonance in Medicine 23

Hilbert T., Nguyen D., Kober T., Thiran J.P., Krueger G., Bieri O.

Oral: TrueCISS: Genuine bSSFP Signal Reconstruction from Undersampled Multiple-Acquisition SSFP Using Model-Based Iterative Non-Linear Inversion

Babayeva M., Falkovskiy P., Kober T., **Hilbert T.**, Bonnier G., Maréchal B., Tisdall D., Kouwe A., Meuli R., Gruetter R., Krueger G.

Oral: Prospective motion correction with FID-triggered image navigators

ISMRM 2016 – Singapore

Annual Meeting of the International Society for Magnetic Resonance in Medicine 24

Hilbert T., Schulz J., Bains L.J., Marques J.P., Meuli R., Thiran J.P., Krueger G., Norris D.G., Kober T.

Oral: Fast Quantitative T2 Mapping using Simultaneous-Multi-Slice and Model-Based Reconstruction

Hilbert T., Thiran J.P., Meuli R., Krueger G., Kober T.

SAFT: Split-Algorithm for Fast T2 Mapping

Hilbert T., Kober T., Thiran J.P., Meuli R., Krueger G.

Phase-Encode Ghosting Detection using Multi-Channel Coil Arrays

Hilbert T., Nguyen D., Thiran J.P., Krueger G., Bieri O., Kober T.

Fast 3D Acquisition for Quantitative Mapping and Synthetic Contrasts Using MIRACLE and trueCISS

Hilbert T., Nguyen D., Thiran J.P., Krueger G., Kober T., Bieri O.

trueFLASH: Model-Based Iterative T1 Mapping using Variable-Flip-Angle Fast Low-Angle Shot

Nguyen D., **Hilbert T.**, Kober T., Bieri O.

Oral: Metal implant imaging using highly undersampled phase-cycled 3D bSSFP

108 Nguyen D., **Hilbert T.**, Ehses P., Scheffler K., Bieri O., Kober T.

On-resonant balanced Steady-State Free Precession imaging at 9.4 T

Mussard E., **Hilbert T.**, Meuli R., Thiran JP, Kober T.
Accelerated MP2RAGE Imaging Using Sparse Iterative Reconstruction

Omoumi P., **Hilbert T.**, Roux M., Ledoux JB, van Heeswijk RB., Meuli R., Kober T.
Buy one, get three for free: Simultaneous Knee T2 Mapping and Morphological Analysis On Synthetic Contrasts Using GRAPPATINI

Gil R., Khabipova D., Zwiers M., **Hilbert T.**, Kober T., Marques JP
Assessing the (ani)sotropic component of R2 as a mean of studying White Matter properties

SMRA 2016 – Chicago, USA
Society for Magnetic Resonance Angiography 28

Lugand E., Yerly J., **Hilbert T.**, Colotti R., Kober T., Stuber M., Heeswijk R.B.
Do signal averaging and undersampling with compressed sensing cancel each other, or is there something to be gained by combining them? A fluorine-19 MRI study

ISMRM 2017 – Honolulu, USA
Annual Meeting of the International Society for Magnetic Resonance in Medicine 25

Hilbert T., Kober T., Zhao T., Block K.T., Yu Z., Thiran J.P., Krueger G., Sodickson D.K., Cloos M.
Oral: Mitigating the Effect of Magnetization Transfer in Magnetic Resonance Fingerprinting

Hilbert T., Marques J.P., Thiran J.P., Meuli R., Krueger G., Kober T.
Model-Based Super-Resolution Reconstruction of T2 Maps

Hilbert T., Roche R., Granziera C., Bonnier G., O'Brien K., Meuli R., Stöcker T., Falkovskiy P., Thiran JP., Krueger G., Kober T.
A T2 Template Map from a Healthy Cohort to Identify Localized Anomalies in Single Subjects

Bonnier G., **Hilbert T.**, Albrecht D, Loggia M., Granziera C.
The MRI signature of glia activation: a PET-MRI study using PBR28 radioligand and MR relaxometry

Mussard E., **Hilbert T.**, Forman C., Meuli R, Thiran J.P., Kober T.
High-resolution 3D T2 mapping of the Brain Using T2-prepared Cartesian Spiral Phyllotaxis FLASH and Compressed Sensing

Raudner R., **Hilbert T.**, Kober T., Juras V., Kronnerwetter C., Stelzeneder D., Trattnig S.
GRAPPATINI put to use: How MSK applications profit from highly undersampled T2 mapping and synthetic contrasts

Darçot E., Yerly J., **Hilbert T.**, Colotti R., Pellegrin M, Najdenovska E., Kober T., Stuber M., Heeswijk R.B.
Compressed Sensing with Undersampling and Signal Averaging Reduces Motion Artifacts in Fluorine-19 MRI

Bonnier G., Roche A., Kober T., **Hilbert T.**, Krueger G., Granziera C.
Personalized deviation map to assess diffuse and focal brain damage

Curriculum Vitae

PERSONAL INFORMATION

<i>Name</i>	Tom Hilbert
<i>Date of birth</i>	January 27, 1989
<i>Place of birth</i>	Gera, Germany
<i>Nationality</i>	German
<i>E-mail address</i>	tom.hilbert@epfl.ch

EDUCATION

<i>Ph.D. Studies</i> 2013 – today	École Polytechnique Fédéral de Lausanne Doctoral Program of Electrical Engineering under the supervision of Prof. Jean-Philippe Thiran and Dr. Gunnar Krueger
<i>Master Studies</i> 2011–2013	Ruprecht-Karls University Heidelberg/ Hochschule Heilbronn Medical Computer Science Thesis: Accelerated Quantitative Mapping of Relaxation Times in MRI
<i>Bachelor Studies</i> 2007-2011	University of Applied Science Stralsund Medical Computer Science and Biomedical Engineering Thesis: Performance Optimization of a Tissue Classification Algorithm
<i>Secondary School</i> 2005-2007	SBBS Technik Gera Major: Electrical Engineering

WORK EXPERIENCE

<i>Siemens</i> 8/2009-3/2013	Advanced Clinical Imaging Technology, Lausanne Development and performance optimization for MRI related algorithms
<i>HANSE-Klinikum</i> 7/2008-7/2009	Interdisciplinary Sleeping Laboratory, Stralsund Technical assistant and patient care
<i>Rhön-Klinikum</i> 4/2008-5/2008	Medical and Cardiac Technology Department, Bad Berka Medical equipment maintenance and assisting on working with a heart-lung machine
<i>Klinikum Jena</i> 8/2007-8/2007	Klinikum der Schiller Universität, Jena Electronical patient record implementation and automatization
<i>ADG</i> 7/2007-7/2007	Apotheken Dienstleistungsgesellschaft mbH Pharmacy Software Gera Technical customer service for pharmacy warehouse software
<i>Silbitz Guss</i> 9/2005-7/2006	Steel Mill Maintenance Department, Silbitz Install and maintain industrial equipment